Search for the Higgs Boson in $H \rightarrow WW$ Decays at the DØ Experiment and Precise Muon Tracking

Dissertation der Fakultät für Physik
der
Ludwig-Maximilians-Universität München

vorgelegt von
Johannes Elmsheuser
geboren in Gießen

München, den 7. Mai 2004

Search for the Higgs Boson in
H → WW Decays at the DØ Experiment
and
Precise Muon Tracking

Dissertation der Fakultät für Physik
der
Ludwig-Maximilians-Universität München

vorgelegt von
Johannes Elmsheuser
geboren in Gießen

München, den 7. Mai 2004

1. Gutachterin: Prof. Dr. Dorothee Schaile
2. Gutachter: Prof. Dr. Martin Faessler
Tag der mündlichen Prüfung: 27. Juli 2004

Zusammenfassung

Die vorliegende Arbeit beschreibt die Suche nach dem Higgs Boson in $H \rightarrow WW^{(*)}$ Zerfällen in Proton-Antiproton-Kollisionen mit Daten des DØ Experiments am Tevatron Beschleuniger. Diese Daten wurden zwischen April 2002 und September 2003 aufgezeichnet und haben eine integrierte Luminosität von etwa $147\,\mathrm{pb}^{-1}$. Es wurde eine Analyse im Zwei-Myonen Zerfallskanal der W-Paare entwickelt, die auf höhere integrierte Luminositäten und auf den bis zum Jahr 2009 aufzuzeichnenden vollen Datensatz skaliert werden kann. Die Anzahl der beobachteten Ereignisse in den vorliegenden Daten ist konsistent mit den Erwartungen des Standardmodells. Da kein Überschuss gesehen wurde, sind Grenzen auf den Wirkungsquerschnitt der $H \rightarrow WW^{(*)}$ Produktion auch in der Kombination mit anderen Leptonzerfallskanälen im 95% Vertrauensintervall berechnet worden. Einen Hauptuntergrund zur $H \rightarrow WW^{(*)}$ Suche stellt die direkte Produktion von W-Paaren dar. Eine erste Messung des Wirkungsquerschnitts von W-Paar-Produktion beim DØ Experiment wird im Anschluß vorgestellt. Die Messung von Spuren mit hoher Genauigkeit ist ein wesentlicher Bestandteil beider Messungen. Die Arbeit schließt mit einem Beitrag zur genauen Spurmessung beim ATLAS Experiment am zukünftigen Large Hadron Collider (LHC). Hierzu wird ein Positionsüberwachungssystem für ATLAS Myondriftkammern am Höhenstrahlungsmeßstand der LMU München vorgestellt.

Abstract

This thesis describes the search for the Higgs boson in $H \rightarrow WW^{(*)}$ decays in proton antiproton collisions with data taken at the DØ experiment at the Tevatron collider. The data set was taken between April 2002 and September 2003 and has an integrated luminosity of approximately $147\,\mathrm{pb}^{-1}$. An analysis of the di-muon decay channel of the W pairs was developed which can be scaled to higher luminosities up to the full data set to be taken until 2009 at the Tevatron collider. The number of events observed in the current data set is consistent with expectations from standard model backgrounds. Since no excess is observed, cross-section limits at 95% confidence level for $H \rightarrow WW^{(*)}$ production have been calculated both standalone and also in combination with other lepton decay channels. The production of W pairs is one major background in the search of $H \rightarrow WW^{(*)}$ decays. Hence a first measurement of the WW production cross-section with the DØ experiment is presented. Experience gained during this analysis has shown the precise track reconstruction is an essential tool for both measurements. This thesis closes with a contribution to precise tracking in the ATLAS experiment at the future Large Hadron Collider (LHC). An alignment system for ATLAS muon drift chambers at the cosmic ray measurement facility at LMU Munich is presented.

Für meine Familie

Da steh ich nun, ich armer Tor!
Und bin so klug als wie zuvor;

Faust
Johann Wolfgang von Goethe

Contents

1 Introduction

Despite the great success of the Standard Model of elementary particles for the electroweak and strong interaction, the mechanism of mass generation of the weak gauge bosons and the fermions is still experimentally unsolved. In the Standard Model, the Higgs boson is a key point of the theory. The experimental discovery of the Higgs boson or something similar is a crucial test of the electroweak theory. Theoretical considerations place an upper limit on a Standard Model Higgs mass around 1 TeV [1]. Experimental limits from direct searches and theoretical calculations using loop corrections place a lower limit at 114.4 GeV [1] and an upper limit at approximately 211 GeV [2] respectively.

The direct search for the Standard Model Higgs boson is one of the main topics at the present and future hadron colliders. This document describes the search for the Higgs boson in $H \to WW^{(*)}$ decays with the DØ experiment at the Tevatron collider at Fermilab near Chicago, USA. Here protons and anti-protons collide at a centre of mass energy of $\sqrt{s} = 1.96\,\mathrm{TeV}$. With the full dataset of $4 - 8\mathrm{fb}^{-1}$ an exclusion or discovery of a Standard Model Higgs boson is possible in the above mentioned mass range. In this thesis the Higgs boson decays will be discussed in detail in the $H \to WW^{(*)} \to \mu^+\nu_\mu\mu^-\bar{\nu}_\mu$ decay channel. Backgrounds and experimental limitations will be examined and a combination with the di-electron and electron-muon decay channel will be presented afterwards. One of the main remaining backgrounds of $H \to WW^{(*)}$ decays is the Standard Model WW production. A detailed understanding of this background is a key point to understanding $H \to WW^{(*)}$ decays. Until now only few W-pairs have been observed in p$\bar{\text{p}}$-collisions leading to unreliable cross-section measurements. A first attempt of a cross-section measurement with the DØ experiment is presented.

In the first chapters it will be demonstrated that a good track finding with high precision and efficiency is essential for the discovery of the Higgs boson and many other important measurements. This fact will also be a key part of the physics programme at the next generation collider. At CERN in Geneva, the Large Hadron Collider, LHC, will collide protons at a centre of mass energy of $\sqrt{s} = 14\,\mathrm{TeV}$ from 2007 onwards. The ATLAS

---

[1] Throughout this document, units are chosen in the rationalised Heavyside-Lorentz system, ie. $\hbar = c = 1$. Masses, momenta and energies all have the units of energies.

experiment is one of two general purpose experiments which will contribute to the understanding of many aspects of the Standard Model. The sophisticated muon system of the ATLAS experiment will help to discover or exclude a Standard Model Higgs boson over a wide mass range in certain decay channels. Parts of this system are tested at the Cosmic Ray Measurement Facility at the Ludwig-Maximilians-Universität München. A muon chamber alignment system for this measurement facility was developed and allows a precise control of the chamber positions.

In the following document Chapter 2 presents an introduction to the basic principles of the Standard Model and Higgs boson physics, whereas Chapter 3 gives an overview of the Tevatron collider and the DØ experiment. Chapter 4 describes details of the event reconstruction with the DØ experiment. In Chapter 5 limits on the $H \to WW^{(*)}$ production in the di-muon channel and a combination with other channels are presented. Chapter 6 describes a first attempt of a WW production cross-section measurement. In Chapter 7 the alignment system of the cosmic ray measurement facility is described in detail. Chapter 8 provides a summary of all results presented in the different Chapters.

2 The Higgs Boson in the Standard Model and its Extensions

This Chapter provides a very brief introduction to the theory and concepts which are used in this thesis.

2.1 The Standard Model

Particle physics studies the fundamental constituents of matter and their interactions. What is called fundamental evolves with the improved understanding of nature. The modern theory, the so called *Standard Model*, explains all phenomena of particle physics in terms of properties and interactions of a small number of particles of three distinct types [3, 4]. The first two are spin-1/2 fermions and called leptons and quarks (Table 2.1), the third are spin-1 bosons and are called gauge bosons which are the 'force carriers' in the theory (Table 2.2). All these particles are assumed to be elementary. There are three generations of lepton and quark families ordered by increasing mass. The lepton families consist of electrons, muons and taus and their corresponding neutrinos. The former particles have an electric charge of one unit whereas the neutrinos do not carry an electric charge and are assumed to be massless. Recent measurements have proven that neutrinos have masses [5] which can be accounted for in the Standard Model. As for leptons, quarks are also ordered into three families. Besides the electric charge of $2/3$ or $-1/3$,

	I	II	III	Charge
Leptons	e	μ	τ	-1
	ν_e	ν_μ	ν_τ	0
Quarks	up	charm	top	$+2/3$
	down	strange	bottom	$-1/3$

Table 2.1: *The three generations of elementary particles with spin* $S = 1/2$.

respectively, they carry an additional charge called “colour” which can be red, green or blue. Unlike leptons quarks are not observable as free particles in nature. They are confined to “colourless” objects which are “baryons” or “mesons”. Baryons consist of three quarks with different colours which sum up to a colourless object. Mesons consist of two quarks with colour and its anti-colour. All particles have a corresponding antiparticle with opposite electric charge but same mass.

In the Standard Model quarks and leptons are postulated as the elementary constituents of matter. The recently discovered dark matter [6] suggests that there must be something else. A description of the interaction between the constituents of matter is needed to complete the picture of the elementary particles. The Standard Model is a quantum field theory where all particles are described as fields. The interactions between fermions are explained by exchanges of mediating particles, equivalently called “gauge bosons”, corresponding to their interaction fields. There are four different types of interactions, also called forces, in nature. The “electromagnetic” force is mediated by massless photons coupling to all charged particles. It has infinite range and the strength is determined by the fine structure constant, $\alpha \approx 10^{-2}$. The “weak” force is mediated by massive weak gauge bosons $W^{\pm}$ and Z^0 and is responsible for e.g. the nuclear β decay. The interaction range of $\hbar/M_{\mathrm{W}}c \approx 10^{-17}\,\mathrm{m}$ and the strength, given by the Fermi constant $G_{\mathrm{F}} \approx 10^{-5}\,\mathrm{GeV}^{-2}$, are very small. The “strong” force is mediated by eight massless gluons with colour and is responsible for the quark interactions. The range is given by the size of a nucleus of $\approx 10^{-15}\,\mathrm{m}$ and the strength depends on the momentum transfer between the quarks and is ≈ 0.1 at a momentum transfer scale corresponding to the mass of the electroweak gauge bosons. The “gravitational” force is much weaker compared to the first three ($\approx 10^{-38}$) and is too weak to be observable in particle physics laboratory experiments. It is not included in the Standard Model.

Force	Gauge Bosons	Mass
electromagnetic	γ	0
strong	$g_1 \dots g_8$	0
weak	$W^{\pm}, Z^0$	$\approx 80, 91\,\mathrm{GeV}$

Table 2.2: *The gauge bosons with spin $S = 1$.*

From Noether’s Theorem follows: invariance of a physical law under a global symmetry transformation results in a conserved quantity. The invariance with respect to translations in time and space and rotation in space provides the conservation of energy, momentum and angular momentum. Together with these quantities the electromagnetic, weak and strong interactions also conserve other quantities related to internal degrees of freedom like the electric charge or colour.

The Standard Model is a quantum field theory which unifies the electromagnetic, weak and strong interactions. Similar to Maxwell's unification of electricity and magnetism the Standard Model combines the electromagnetic and the weak force to an electroweak interaction. The special feature of the Standard Model is that the Lagrangian of the theory in also invariant under local symmetry transformations, called gauge transformations. The $SU(3)$ symmetry of Quantum Chromodynamics (QCD) is related to rotations in colour space. The Electroweak Theory, a unification of the weak interaction and Quantum Electrodynamics (QED), has a $SU(2) \times U(1)$ symmetry related to rotations in weak iso-spin and in hypercharge space. All left-handed fermions carry weak iso-spin $I = 1/2$. The hyper-change Y is defined by $I_3 = Q - Y/2$ where Q is the electric charge and $I_3 = \pm 1/2$ is the third component of the weak iso-spin.

To have predictive power a quantum field theory has to be "renormalisable". The quantitative features of the interactions can be calculated to arbitrary accuracy as perturbative expansion of the coupling constant given a few parameters by a limited set of measurements. If all divergencies caused by higher order corrections can be absorbed into physical measurable quantities the theory is "renormalisable". All above mentioned quantum field theories are renormalisable.

The principle of local gauge invariance is applicable to the strong and electromagnetic interactions. The application is not directly possible for the weak interaction due to its massive gauge fields. The introduction of the spontaneous symmetry breaking and the so called "Higgs-mechanism" [7] helps to overcome this problem. The renormalisability remains intact if gauge symmetry is spontaneously broken, that means if the Lagrangian is gauge invariant but the vacuum state and the spectrum of particles are not. A set of elementary scalars fields ϕ is introduced with a potential energy $V(\phi)$ that is minimised at a value of $< \phi > \neq 0$ and the vacuum energy state is degenerate. The $U(1)$ gauge invariant potential, for example, of an electrically charged scalar field $\phi = |\phi| e^{i\theta}$,

$$V(|\phi|^2) = -\mu^2 |\phi|^2 + \lambda |\phi|^4, \tag{2.1}$$

has its minimum at $< |\phi| > = \mu/\sqrt{2\lambda} = v/\sqrt{2}$, but is independent of the phase θ. The choice of a value for θ spontaneously breaks the gauge symmetry. The massive Higgs scalar particles of mass $m_{\mathrm{H}} = \sqrt{2}\mu = \sqrt{2\lambda} v$ are excitations of ϕ around its vacuum value. Excitations around the vacuum value of θ require no energy and correspond to massless and spinless Goldstone bosons. In the physical spectrum they appear as the longitudinal polarisation third degree of freedom of the gauge bosons. The gauge bosons acquire masses through their couplings to the Higgs field. Their masses m are given by $m = gv/2$ where g are their couplings to the Higgs field and v is the the vacuum value of the Higgs field. In this model the Fermi constant G is given by $G = \sqrt{2} g^2 / 8m^2 = 1/(v^2 \sqrt{2})$.

The theory of the electroweak interaction predicts four gauge bosons. The local invariance under $SU(2)$ transformations requires three gauge fields: $W^{\pm}$ and W^0 with coupling $g = e \sin\theta_W$, where e is the electric charge and θ_W is the Weinberg angle. The local invariance under $U(1)$ transformations yields the B^0 with coupling $g' = e\cos\theta_W$. The symmetry breaking is introduced by a complex iso-doublet scalar field with $\phi = \phi_1 + i\phi_2$ and $\phi^*\phi = \phi_1^2 + \phi_2^2$ and a potential following Eq. 2.1. Minimisation of the vacuum energy gives $v = 246\,\mathrm{GeV}$ and leaves three Goldstone bosons that are absorbed by three massive vector bosons: $W^\pm$ and $Z^0 = -\sin\theta_\mathrm{W} B^0 + \cos\theta_\mathrm{W} W^0$ and one massless photon $\gamma = \cos\theta_\mathrm{W} B^0 + \sin\theta_\mathrm{W} W^0$. The Weinberg angle θ_W can be determined experimentally through $\nu - e$ scattering, by electroweak interference in e^+-e^- scattering, by Z^0 line-shape measurements or by the mass ratio of the $W^\pm$ and Z^0 bosons. The ratio $\rho = m_W^2/m_Z^2\cos^2\theta_\mathrm{W}$ is predicted to be 1 at Born level and probes the multiplet structure of the Higgs boson. Deviations from 1 due to higher order corrections are sensitive to the mass of the Higgs boson.

In the Standard Model quarks and leptons also acquire their masses through the Higgs particle. They are given by the product of the Yukawa coupling $\tilde{g}_\mathrm{fermion}$ and the vacuum expectation value $v/\sqrt{2}$ of the Higgs field. These masses are non calculable parameters of Standard Model since their Yukawa couplings to the Higgs boson are arbitrary. The validation of the Standard Model explanation for elementary particle masses requires the discovery of the Higgs boson.

2.2 Higgs Production

The Higgs mechanism presented in the previous Section is only one model of electroweak symmetry breaking. Present experimental data are not sufficient to identify with certainty the nature of dynamics behind the mechanism. The search for the origin of weak gauge boson and fermion masses requires continuous experimentation at present and future colliders [8].

The mass of the Standard Model Higgs bosons is given by $m_\mathrm{H} = \sqrt{2}\mu = \sqrt{2\lambda}v$, with the Higgs self-coupling parameter λ. Since λ is unknown, the mass value of the Higgs particle is unpredicted. However, the couplings of the Higgs boson to fermions and gauge bosons are proportional to the corresponding particle masses as predicted by theory (cf. Figure 2.1).

In Higgs production and decay processes at colliders the dominant interactions involve couplings to $W^\pm$ and Z^0 bosons and the third generation of quarks and leptons. Figure 2.2 shows the leading order diagrams of these processes in the production of a Higgs boson. Except for very heavy Higgs bosons, the dominant production mechanism is $gg \to H$, via an intermediate top quark loop (cf. Figure 2.2(a)). The cross-section for Higgs production associated with W or Z bosons are smaller, but are useful for detecting a light Higgs boson which decays into $b\bar{b}$ or $\gamma\gamma$ pairs. The weak boson decay can be used to discriminate the Higgs boson signal against other background sources. The weak boson fusion and

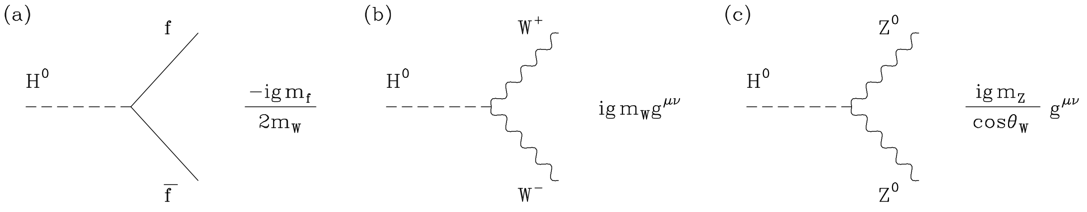

Figure 2.1: *Interactions of the Standard Model Higgs boson at tree level [9].*

associated production with $t\bar{t}$ is less important at the Tevatron collider (cf. Section 3.1), but are also important production modes at the LHC collider (cf. Section 7.1).

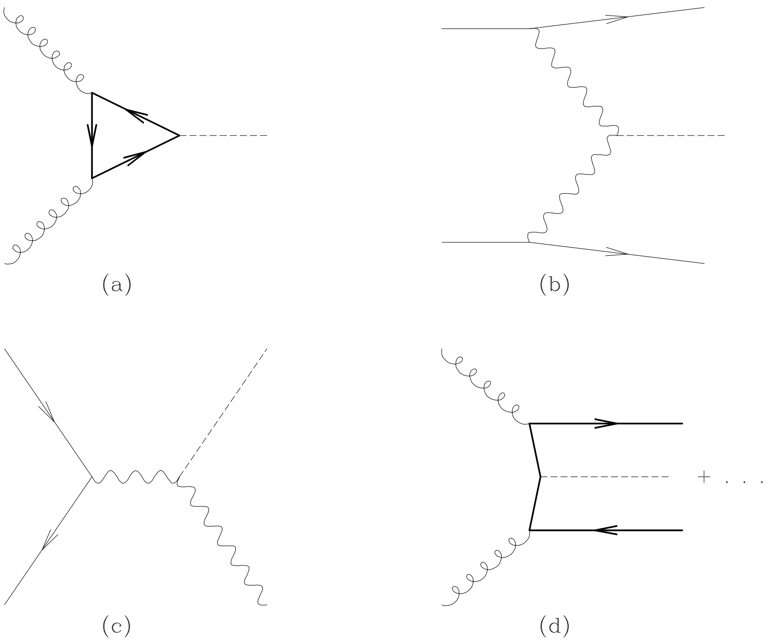

Figure 2.2: *The dominant Higgs production mechanisms at hadron colliders: (a) gluon-gluon fusion, (b) vector boson fusion, and associated production with (c) W, Z bosons and (d) $t\bar{t}$ [10].*

Figure 2.3 shows the production cross-sections of a Higgs particle as a function of its mass at a centre of mass energy of $\sqrt{s} = 2\,\text{TeV}$ approximately corresponding to the Tevatron collider energy. The gluon fusion process is the dominant production mode at the Tevatron with a cross-section in the range of 1.0 – 0.1 pb for a Higgs mass between 100 and 200 GeV. The decay mode $gg \to H \to b\bar{b}$ is not very promising due to the overwhelming

QCD background. For a higher mass Higgs particle the $H \rightarrow WW^{(*)}$ decay mode provides a promising discovery mode.

In the mass region below 130 GeV a promising mode is the $q\bar{q}$ annihilation into a virtual W^* or Z^* with subsequent radiation of $W^*/Z^* \rightarrow W/ZH$ and following $H \rightarrow b\bar{b}$ and the W or Z decaying leptonically. The final state leptons can be used for event trigger purposes. The production cross-section span a range of $0.25 - 0.002$ pb for $m_{\mathrm{H}} = 100 - 300$ GeV and are larger for the $\mathrm{p\bar{p}}$ collider than for pp collider where the gluon-gluon fusion dominates.

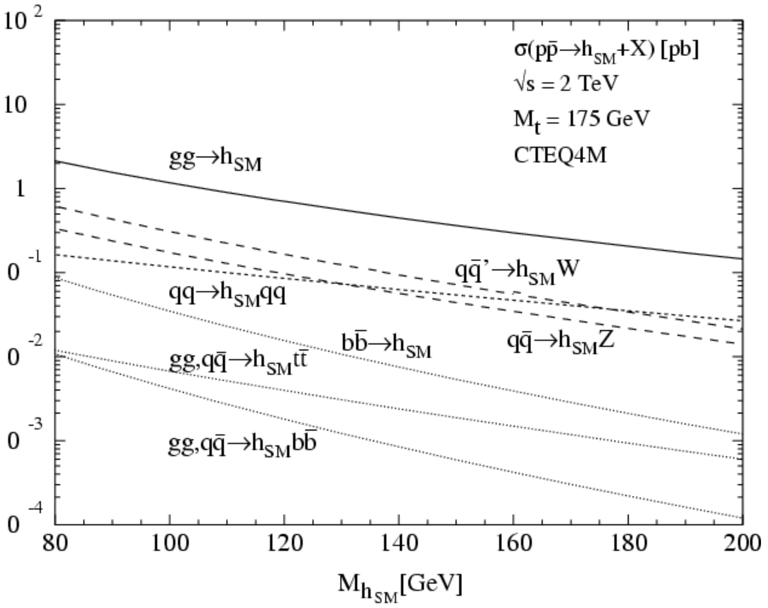

Figure 2.3: *Higgs production cross-section (in units of pb) at the Tevatron as a function of its mass [11].*

Figure 2.4 shows the branching ratios for the dominant decay modes of a Standard Model Higgs boson as a function of its mass [12]. For masses below about 130 GeV, the decay into $b\bar{b}$ pairs dominates, whereas for higher masses the decay mode $H \rightarrow WW^{(*)}$, where at least one of the two W bosons is off-shell becomes important. The corresponding decay into $ZZ^{(*)}$ is one of the gold-plated modes for Higgs searches at the future Large Hadron collider LHC with both Z decaying into electrons or muons, but it is less useful at the Tevatron.

Theory places an upper limit on the Higgs mass of around 1 TeV from unitary requirements of the process $f^+f^- \rightarrow W^-W^+$ (where f denotes a fermion) at high energies. Divergences can only be compensated if corrections including a Higgs coupling proportional the electron mass is added.

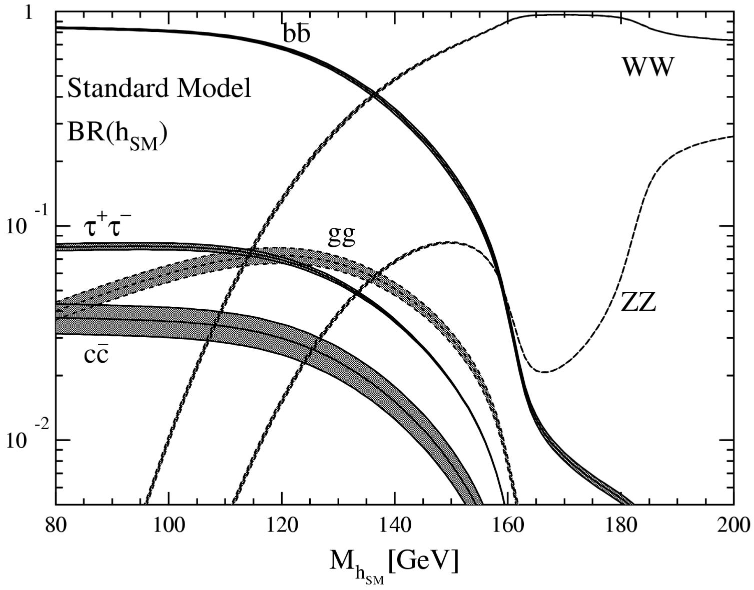

Figure 2.4: *Branching ratios of the dominant decay modes of the Standard Model Higgs boson as a function of the its mass.*

The existence of the Higgs particle in the Standard Model has an impact on the values of most electroweak parameters via higher order corrections. The theory is only renormalisable as mentioned in the previous Section if a Higgs particle exists. Limits can be placed on the Higgs mass by precise measurements of the W boson and top quark mass due to their dependence on its mass in loop corrections. The left plot in Figure 2.5 shows the predictions of the W boson and top quark mass from electroweak radiative corrections using SLD and LEP-1 (solid contour) together with direct measurements from LEP-2 and Tevatron data (dashed contour). The yellow band shows the Standard Model constraints between the two masses depended on Higgs particle mass. Both indirect and direct measurements prefer a low value for the Higgs particle mass. The arrow labelled $\Delta\alpha$ shows the variation of the relation between m_{W} and m_{t} if $\alpha(m_{\mathrm{Z}}^2)$ is changed by one standard deviation. Furthermore, a joint fit of all data using 20 different electroweak parameters gives the best constraint to the Higgs particle mass m_{H}. The right plot in Figure 2.5 shows the $\Delta\chi^2$ curve as a function of m_{H} with a minimum of $m_{\mathrm{H}} = 91^{+58}_{-37}\,\mathrm{GeV}$ which corresponds to a one-sided upper limit of 211 GeV at 95% CL. The fitted mass has strong correlation with the top quark mass. The fits are shown with and without the result of the NuTeV collaboration on neutrino-nucleon neutral to charged cross-section ratios. The NuTeV results in terms of the on-shell electroweak mixing angle is 2.9 standard deviations higher than the expectations.

Apart from indirect constraints also direct searches for the Standard Model Higgs boson have been performed. The yellow shaded band in the right plot of Figure 2.5 is the excluded region of the current best lower limit of $m_{\mathrm{H}} > 114.4\,\mathrm{GeV}$ at 95% CL set by the combination of all four LEP experiments [1].

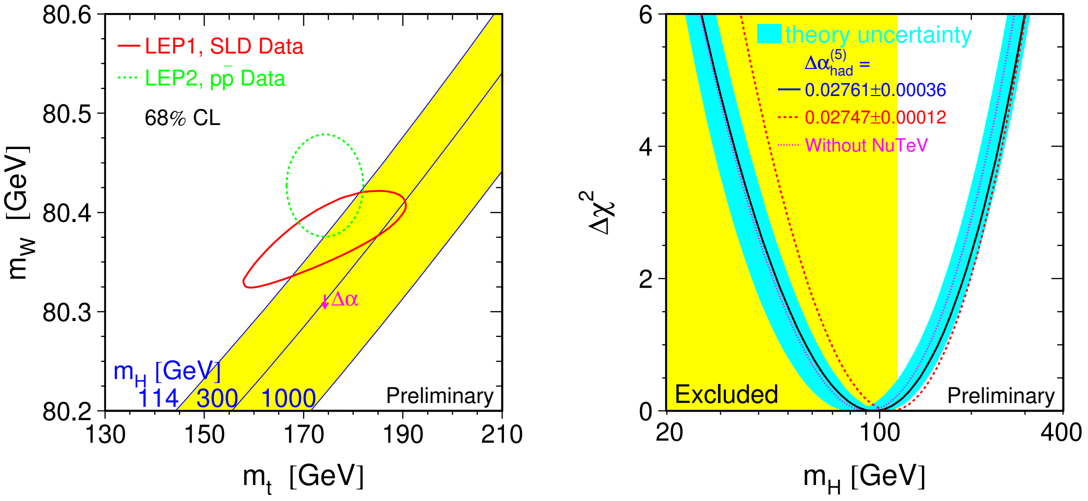

Figure 2.5: *Left: Contour curves of* 68% *CL in the plane of the top quark and W boson mass. These values give constraints on the mass of the Standard Model Higgs boson. Right:* $\Delta\chi^2$ *curve of a joint fit from different electroweak precision measurement results as a function of the Higgs mass. The yellow band denotes the excluded mass region from direct Higgs searches at LEP [2].*

2.3 Background Processes

As described in the previous sections the Higgs particle will be searched in the process $\mathrm{p\bar{p}} \to H \to WW^{(*)}$. The leptonic decay channels of the $W \to l\nu$ bosons give a clear signal of a lepton with high transverse momentum and some significant missing transverse energy coming from the undetected neutrino. The branching ratio for each leptonic decay mode is only around 10% per W boson, nevertheless the hadronic decay modes are swamped by background from QCD jet production with much higher cross-sections and similar event topology.

Background processes that have a similar event topology like the process $H \to WW^{(*)} \to l^+\nu l^-\bar{\nu}$ are the Drell-Yan process $q\bar{q} \to Z/\gamma^* \to l^+l^-$, the vector boson production mode $\mathrm{p\bar{p}} \to WW \to l^+\nu l^-\bar{\nu}$ and top quark pair production $\mathrm{p\bar{p}} \to t\bar{t} \to l^+\nu l^-\bar{\nu}b\bar{b}$. Figure 2.6

shows an illustration of the Drell-Yan process. The leading order (LO) cross-section for producing a lepton pair is obtained by weighting the cross-section $q\bar{q} \to l^+l^-$ with the parton distribution functions $f_q(x,Q^2)$ and $f_{\bar{q}}(x,Q^2)$ extracted from deep inelastic scattering and summing over all quark-antiquark combinations [10]. The cross-section $q\bar{q} \to l^+l^-$ is given by:

$$\sigma(q(x,Q^2)\bar{q}(x,Q^2) \to l^+l^-) = \frac{4\pi\alpha^2}{3\hat{s}}\frac{Q_q^2}{N} \tag{2.2}$$

where $\hat{s} = (p_1 + p_2)^2$ the sum of the incoming particle four momenta, α the electromagnetic coupling constant, Q_q the quark charge and N the colour factor. The incoming quark and anti-quark centre of mass energy is a fraction of the collision energy $\sqrt{\hat{s}}$. The next-to-next-to-leading order corrections for the process are well calculable and are in the range of a factor 1.4 [13] for masses around $M \sim M_Z$. At invariant dilepton masses $M \sim M_Z$ the Z boson resonance is clearly visible. The s-channel Z boson exchange has to be added to the $q\bar{q} \to \gamma^* \to l^+l^-$ process. The cross-section has the same structure as Equation 2.2 but a different colour-averaging factor. This process will be used in the following sections thoroughly to study different detector and algorithm efficiencies.

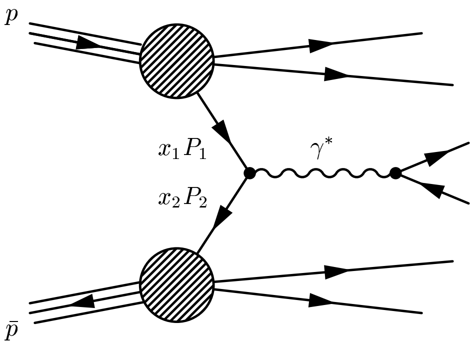

Figure 2.6: *Lepton pair production in the Drell-Yan model.*

The process $p\bar{p} \to WW \to l^+\nu l^-\bar{\nu}$ is the second remaining background. The measurement of the production cross-section will be one part of the following analysis. The Standard Model makes specific predictions of the gauge boson self-interactions as mentioned in the previous sections. Anomalous couplings [14] or decays of new particles from physics beyond the Standard Model result in enhanced W^-W^+ production. Furthermore trilinear vector boson couplings WWZ and $WW\gamma$ can be tested as predicted by the $SU(2) \times U(1)$ symmetry of the electroweak interaction. Using the CTEQ5 [21] parton density function the total cross-section for W^-W^+ production at the Tevatron with a centre of mass energy $\sqrt{s} = 2\,\text{TeV}$ is predicted to be approximately 13.5 pb [16].

2.4 Extensions of the Standard Model

The rate of events coming from $H \to WW^{(*)}$ decays may be larger in alternative theoretical models. As mentioned in earlier sections the electroweak breaking mechanism might be realised in a different way or the Standard Model is based on a more fundamental theory which is valid in a larger energy range.

A larger production cross-section is given in a so called fourth-generation model, where the Higgs production cross-section is approximately 8.5 times larger in a mass range of $100\,\mathrm{GeV} < m_\mathrm{H} < 200\,\mathrm{GeV}$ [17]. In the standard model the main contribution of the Higgs boson comes from the triangular diagram with a top quark loop (cf. Section 2.2) in the gluon-gluon fusion process. With an additional generation there are two additional diagrams with replaced top quarks. The production enhancement will be visible in all decay channels of the Higgs boson. The current limit on a fourth generation quark is $m_4 > 199\,\mathrm{GeV}$ [18].

In Fermiphobic Higgs models the coupling of fermions to the Higgs particle is suppressed [19]. This leads to a larger decay branching ratio into W or γ pairs. This is especially important for the mass region below $m_\mathrm{H} < 140\,\mathrm{GeV}$, where a Standard Model Higgs particle decays mainly into $b\bar{b}$ pairs.

2.5 Event Simulation

In particle physics Monte Carlo simulations are a commonly used technique to analyse the reactions described in the previous sections. The theoretical predictions are brought into a common data format and can be compared to measured data. First, the reactions of the interacting particles and their daughter particles are produced with pseudo random generators on a four vector basis obeying the underlying theory. Starting with the particle density functions of the incoming protons and anti-protons the different matrix elements are calculated for a given reaction. PYTHIA [20] is a commonly used leading order Monte Carlo simulation programme. This programme can simulate a large set of Standard Model processes and physics beyond the Standard Model. Most of the so called "$2 \to 2$" or "$2 \to 1$" processes can be fully simulated, ie. reactions where two primary particles produce one or two secondary particles. This includes also initial and final state radiation. The parton distribution functions $f_\mathrm{i}^\mathrm{q}(x,Q^2)$ or $f_\mathrm{i}^{\bar{\mathrm{q}}}(x,Q^2)$ are included into these calculations. The functions parameterise the probability to find a parton i with a fraction x of the beam energy if a proton or anti-proton is probed at virtuality Q^2. There are many such parameterisations. Here, the leading order parton distributions CTEQ4L [15] and CTEQ5L [21] are used.

In parallel the so called “underlying event” is simulated. This is the remainder of the primary interactions since not all partons of the initial protons and anti-protons are involved in the primary hard interaction. The “underlying event” is added to the primary interaction for the following steps of the simulation.

After the primary particle reaction, initial- and final-state radiation is simulated. In a good approximation the parton shower model simulates higher order corrections of gluon and/or photon radiation caused by coloured and/or charged objects in the event [20]. The branching of one parton or more yield a good description of multi-jet events. In the next step the partons are fed through a simulation of the hadronisation and a detector simulation.

Since the primary quarks or gluons cannot be seen in a real detector a hadronisation of these particles to mesons and baryons is simulated. The hadronisation describes the transition of the primary produced particles to observable hadrons. This process cannot be calculated with perturbative methods in QCD since the scale of momentum transfer is small and so the the strong coupling constant α_S has large values. Phenomenological methods are used instead for the transition of the primary particles to multi particle end states. A commonly used model is the Lund string fragmentation model [22]. In this model the force between two primary quarks is described similar to a string. Iteratively a meson $q_0\bar{q}_1$, e.g., is build from a primary quark q_0 and a newly build quark pair $q_1\bar{q}_1$. The remaining quark q_1 can build a stable state together with a new quark q_2 and so on. The different probabilities for a new quark pair and stable mesons are given as input parameters. The probability of the energy and momentum transfer between the new quark pairs and remaining quarks is parameterised by a fragmentation function for each quark flavour separately.

The commonly used detector simulation programme GEANT [23] simulates the reaction of the particles and partons in their passage through matter. All hits and drift spectra the particles would cause in a real detector are simulated in a digitisation afterwards. After that a set of minimum bias events is overlaid to the primary reaction. Since the interaction rate of proton and anti-proton collisions is very high and protons and anti-protons are bunched in the accelerator, there might be some remainders of the soft interaction in the detector from proton and anti-proton interactions in the same bunch crossing. These events are simulated by minimum bias events.

After all these steps the theoretical predictions have the same data format as the actual measured data and can be analysed with the same reconstruction software and same methods.

3 The Tevatron Accelerator and DØ Experiment

The DØ experiment is one of two detectors located at the Tevatron collider at the Fermi National Accelerator Laboratory (Fermilab) near Chicago, USA. Besides other important measurements the top quark was discovered during the so called "Run I" period of data taking between 1991 and 1996. An integrated luminosity of approximately $100\,\mathrm{pb}^{-1}$ was recorded by each experiment. In the year 2001 after major upgrades to the accelerator complex and the two experiments a new period of data taking has begun. In this so called Run II it is planned to accumulate an integrated luminosity of $4-8\,\mathrm{fb}^{-1}$ per experiment until 2009 depending on the accelerator performance.

3.1 The Tevatron Accelerator

The Tevatron is until the start of the Large Hadron Collider (LHC) in 2007 at CERN in Geneva, Switzerland (cf. Section 7.1) the worlds most energetic collider. Protons and anti-protons collide at a centre of mass energy of $\sqrt{s} = 1.96\,\mathrm{TeV}$. It was one of the first superconducting synchrotron when it was build in 1983. The collider is located in a ring tunnel of 1 km radius. The magnetic field of 4.2 T is produced by superconducting dipole and quadrupole magnets. The ultimate goal for Run II is to reach an instantaneous luminosity of $2 \cdot 10^{32}\,\mathrm{cm}^{-2}\mathrm{s}^{-1}$ though presently the maximum achieved is about a factor of four smaller. The reason for this is caused by a sum of small effects in the accelerator chain, but one larger effect is due to the low efficiency in the number of anti-protons that are finally transfered to the Tevatron. Protons and anti-protons circulate in 36 bunches each, separated by 396 ns in the Tevatron during operations. In the second phase as of Run II is was foreseen to lower the bunch crossing time to 132 ns after several upgrades to the accelerator complex and the detectors. This lowers the number of interactions per crossing at a given instantaneous luminosity. Recently all upgrade plans have been changed substantially and only minor upgrades are planned now to assure a long term reliable operation.

Figure 3.1 shows an aerial view of the Fermilab accelerator complex. The Tevatron is only the last part in a long chain of accelerators. First negatively charged hydrogen ions (H^-) are accelerated with a 750 keV Cockcroft-Walton accelerator, where it is bunched and subsequently fed into a 400 MeV linear accelerator (Linac). After that a thin graphite foil strips off both electrons of the hydrogen ions and leaves protons that are injected to the Booster. This is a 475 m long synchrotron ring which accelerates protons to 8 GeV for the Main Injector. The Main Injector itself is a 3 km synchrotron that accelerates protons and anti-protons to 150 GeV before they are injected into the Tevatron. Anti-protons are produced by 120 GeV protons from the Main Injector which hit a nickel target. A lithium lens focuses anti-protons with an energy of about 8 GeV from the target particle showers. After that anti-protons are de-bunched, stochastically cooled and stored in the accumulator before being inserted into the Main Injector. The Tevatron ring accelerates both protons and anti-protons from 150 TeV to 980 GeV. The beams will be brought to collisions at two interaction points at the DØ and CDF detectors.

Figure 3.1: *Aerial view of the Tevatron accelerator complex.*

3.2 The DØ Detector

The DØ detector is a multi purpose detector with a similar layout as other modern large scale collider physics detectors. A side view is shown in Figure 3.2. As $p\bar{p}$ collisions happen in the centre of the detector an almost complete 4π solid angle coverage allows a measurement of all reaction products and their properties. Several sub-detectors for different particle identifications are in concentric order around the nominal interaction point. A detailed description of all detector components is given in [24].

The DØ coordinate system is defined with its centre in the nominal interaction point and the z-axis pointing into the proton beam direction. The x-axis is pointing towards the centre of the Tevatron ring and the y-axis is pointing upwards. The spheric coordinates are given by the radius R, polar angle θ and azimuthal angle ϕ. The pseudo-rapidity η given by

$$\eta = -\ln\left(\tan\frac{\theta}{2}\right) \tag{3.1}$$

is often used instead of the polar angle θ.

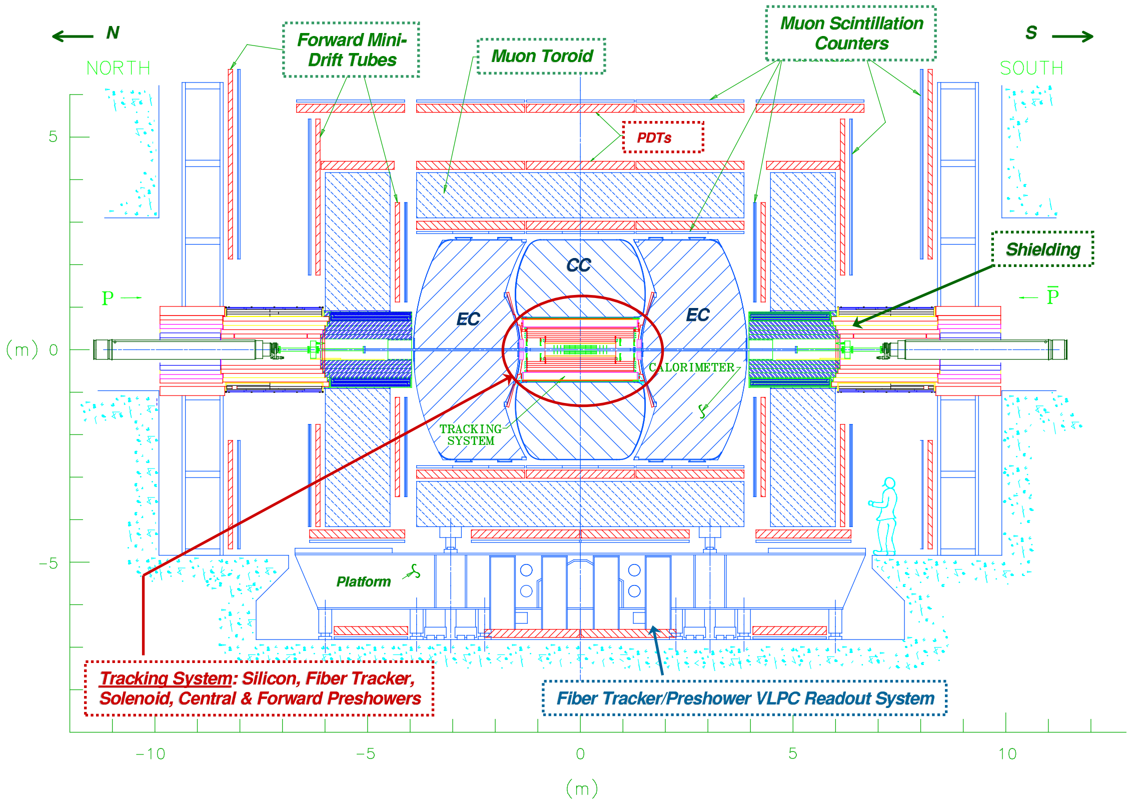

Figure 3.2: *2D outline of the DØ detector.*

3.2.1 The Tracking System

The tracking system consists of an inner silicon detector and an outer scintillating fibre tracker which are placed within a 2 Tesla superconducting solenoid of 2.8 m length and 60 cm radius. Figure 3.3 shows a side view of the DØ tracking system which is designed to detect tracks in an pseudo-rapidity range of $-3 < \eta < 3$. It provides charged particle momentum measurement, e/π separation, electron identification and detection of secondary vertices for b quark identification. The expected momentum resolution of the whole tracking system can be parametrised by $\Delta p_T/p_T = 0.02 + 0.002 p_T$ at $|\eta| = 0$. [24].

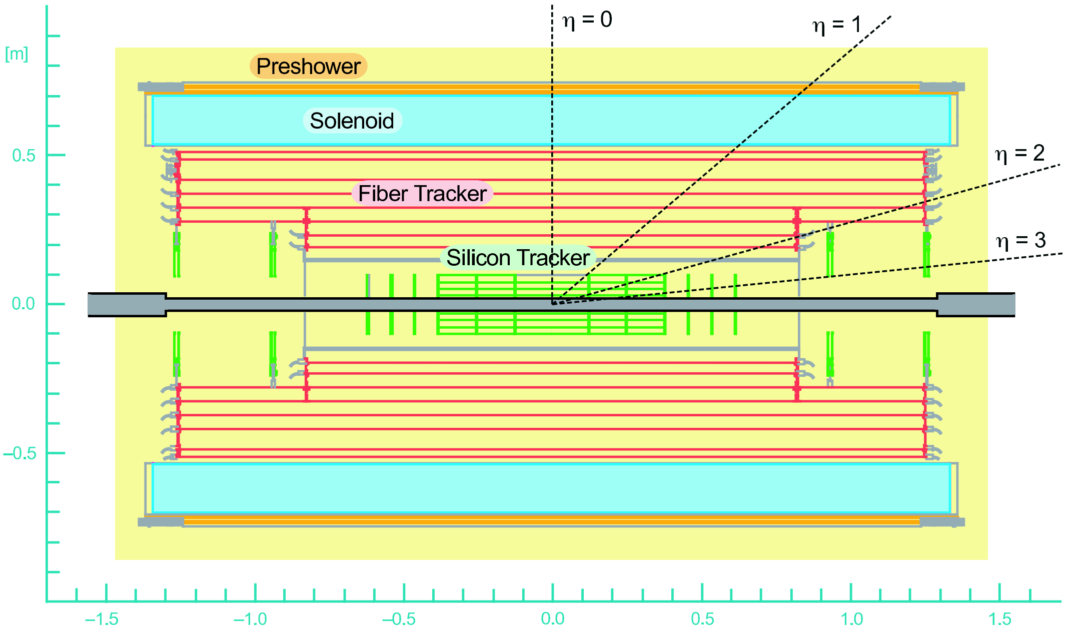

Figure 3.3: *2D outline of the DØ tracking system.*

The Silicon Micro-strip Tracker (SMT)

The Silicon Micro-strip Tracker (SMT) is composed of three sub-detectors: the central barrels, the F-Disks and the H-Disks. The central barrels are made of six cylindrical barrels with three on either side of the interaction point. They are 12.4 cm long and have a maximum radius of $r \approx 10$ cm. The barrels are built of four double layers of silicon detectors in rectangular shape (ladders) which are mounted on a beryllium support structure. The twelve F-Disks are made of twelve double-sided detectors in wedge-shape. Six disks are located in between the barrels with one attached to each end of the barrel detector. Two triplets of the remaining six disks are located in a small distance from either end of the barrel detector. About one metre from the interaction point are the H-Disks which span the detection region of $9.6\,\mathrm{cm} < r < 23.6\,\mathrm{cm}$. The SMT allows tracking in a pseudo-rapidity range of $|\eta| < 3$ and has about 800000 readout channels. The micro-strip detectors provide a hit resolution of approximately 10μm.

The Central Fibre Tracker (CFT)

The scintillating fibre tracker surrounds the silicon detector and covers the pseudo-rapidity range within $|\eta| < 1.62$. It consists of 8 cylindrical layers of two fibre doublets with a radius in the range of $19.5\,\mathrm{cm} < r < 51.4\,\mathrm{cm}$. Each doublet is made of two layers of 835μm diameter scintillating fibres separated by 870μm. Both layers have an offset of half a fibre width to each other to fill all gaps. On each of the eight layers there is an axial doublet for r and ϕ measurement and a stereo doublet rotated by $\pm 3^{\circ}$ to provide stereo information. The axial layers are also used for for triggering (c.f. Section 3.2.5). The scintillating fibres are mounted on carbon fibre support structures and are up to 2.5 m long. They are connected to visible light photon counters (VLPCs) via $7-11$ m long optical waveguides. The VLPCs are located below the whole DØ detector in a cryostat at an operation temperature of ≈ 9 K. They are small silicon devices highly doped with As with excellent quantum efficiency and high gain and basically work as solid state photomultiplier tubes. The CFT detector has in total approximately 77000 readout channels. The hit resolution is about 100μm.

The Pre-shower Detectors (CPS and FPS)

Two additional tracking detectors are located outside the solenoid magnet: the central and forward pre-shower detectors (CPS and FPS). The CPS is mounted on the solenoid at a radius $r = 72\,\mathrm{cm}$ and covers a pseudo-rapidity range of $|\eta| < 1.2$. The FPS sits on the inner surface of the end calorimeter cryostat (c.f. Section 3.2.2) and covers a pseudo-rapidity range of $1.4 < \eta < 2.5$. Both detectors consist of lead absorbers followed by several layers of triangular shaped axial and stereo scintillator strips. Similar to the CFT these are connected through waveguides to VLPCs. CPS and FPS are used as tracking devices for a precise position measurement and as calorimeter for early energy sampling. They provide an improved electron identification, triggering and a determination of the energy loss in the solenoid.

3.2.2 The Calorimeter

The outline of the calorimeter is basically unchanged compared to Run I. Only the readout electronics was upgraded to cope with the higher rates and shorter bunch crossing intervals. Figure 3.4 shows a three dimensional view with its central and two end cap calorimeters located in separate cryostats covering a pseudo-rapidity range of $|\eta| < 4$. The calorimeter measures the energy of electrons, photons and jets and is used for the calculation of the missing transverse energy. It is a hermetic liquid argon sampling calorimeter. The absorber material in the electromagnetic and inner hadronic section is made from depleted uranium due to its high density and compensating e/π response. The outer layers consist of stainless steel and copper. The central calorimeter consists of three concentric

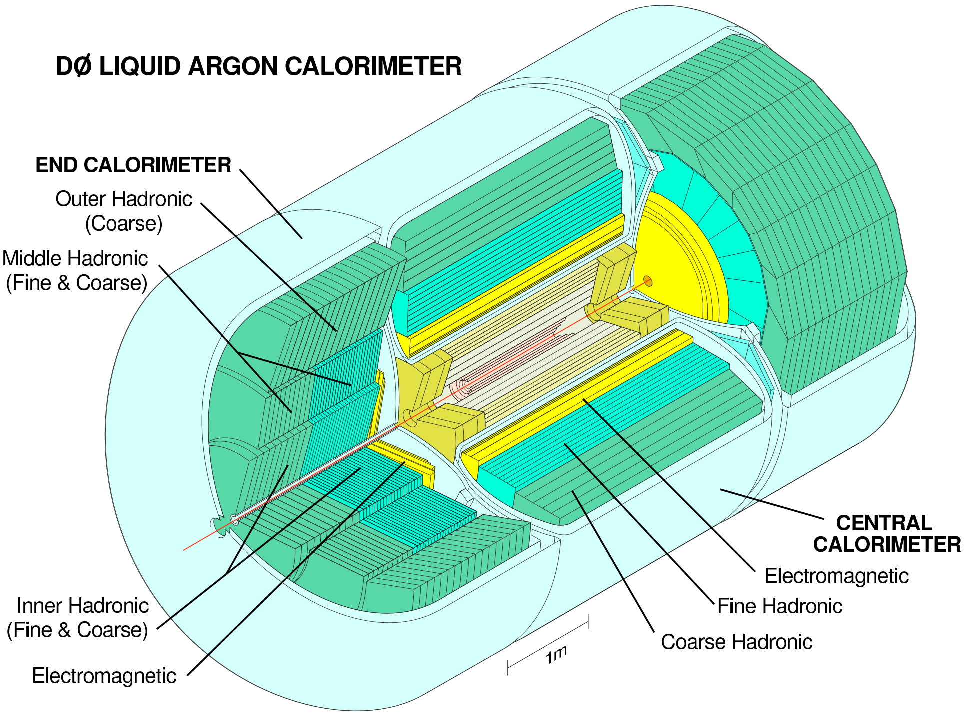

Figure 3.4: *Outline of the DØ calorimeter system.*

regions and covers a pseudo-rapidity range $|\eta| < 1.2$: the four electromagnetic layers, followed by three fine hadronic and one coarse hadronic layer. The end cap calorimeters are covering a range of $1.4 < |\eta| < 4$ and are made of four electromagnetic layers and three concentric cylinders for hadronic showers, called inner, middle and outer modules. Each layer is segmented into cells of 0.1×0.1 in $\eta \times \phi$ units apart from the far forward region ($|\eta| > 3.2$) with a cell size of 0.2×0.2. The third electromagnetic layer is segmented into 0.05×0.05 cells since electrons are expected to reach their shower maximum in this region. All modules are grouped to semi projective towers but their boundaries are not aligned to avoid continuous inter-modules cracks. For trigger information cells are formed to towers of 0.2×0.2 size and read out by separate electronics. The calorimeter response for electrons and charged pions has been measured from test beam data to be:

$$\begin{aligned} \text{electrons}: \ \sigma_{\mathrm{E}}/E &= 15\%/\sqrt{E} + 0.3\% \\ \text{pions}: \ \sigma_{\mathrm{E}}/E &= 45\%/\sqrt{E} + 4\% \end{aligned} \tag{3.2}$$

The inter-cryostat detector (ICD) is located in the overlap region between the central and end cap calorimeter in a pseudo-rapidity range of $0.7 < |\eta| < 1.4$. It compensates the dead region between the cryostats. It provides a correction for the energy loss in the this region and improves the jet energy and missing transverse $\not{E}_{\mathrm{T}}$ measurement. The ICD consists of one single layer of 384 scintillating tiles each mounted on both end cryostats. The detector signals are read out by photo-tubes which are connected by wavelength-shifting fibres.

3.2.3 The Muon System

The muon system consists of two separate systems covering the central pseudo-rapidity region $|\eta| < 1$ and the forward region with $1 < |\eta| < 2$. The central muon detector is split into 3 layers (A, B and C) of proportional drift tubes (PDTs) that provide muon identification and a momentum measurement independent of the central tracking system. The inner A layer and outer B and C layers are separated by a solid iron magnet which produces a 1.8 T toroid field. The PDTs are made from extruded aluminium of rectangular shape with a size of $5.7\,\mathrm{cm} \cdot 10\,\mathrm{cm}$. The anode wires are made of gold-plated tungsten. The A-layer is between the calorimeter cryostat and the muon toroid magnet, whereas the B and C-layers are outside the magnet with a distance of 1 m to each other. Since the PDT's drift time of 750 ns is longer than the brunch crossing time of the Tevatron accelerator there are extra layers of scintillation counters for trigger output. There are two different types: the $A - \phi$-counters, a layer of scintillators between the calorimeter and the A-layer PDTs which in addition reject out-of-time cosmic rays and scattered particles from the calorimeter. The second type are the cosmic caps that are mounted outside the C-layer of the PDTs. Due to the support structure of the DØ detector the bottom part of the detector is only partly covered with these scintillator counters. This leaves a hole in the azimuthal angle range $4.25 < \phi < 5.15$ in the trigger acceptance region of the di-muon trigger (c.f. Section 3.2.5).

The forward muon system consists of three layers of mini drift tubes (MDTs) and three layers of scintillation counters. The MDTs have been newly build for Run II and are more radiation hard than the PDTs. They are composed of eight cells of extruded aluminium combs with a cross-section size of $10 \times 10\,\mathrm{mm}^2$ and all have a anode wire of radius 50μm. Though the drift time of the MDTs is approximately 60 ns scintillation counters are used for triggering and for rejection of cosmic rays and other sources of background. Time resolutions of around 2.5 ns are expected for the scintillation counters depending on their size. The forward muon system has additional shielding around the beam pipe to reduce trigger rates and the aging of the detectors by beam halo. Figure 3.5 shows the outline of the DØ muon system.

The design momentum resolution of the muon system can be parameterised approximately by: $\Delta p/p = 0.18 + 0.003p/\mathrm{GeV}$. The resolution is limited by multiple scattering at low momentum. At high momentum it is limited by the individual hit resolution and is presently significantly worse measured with real data.

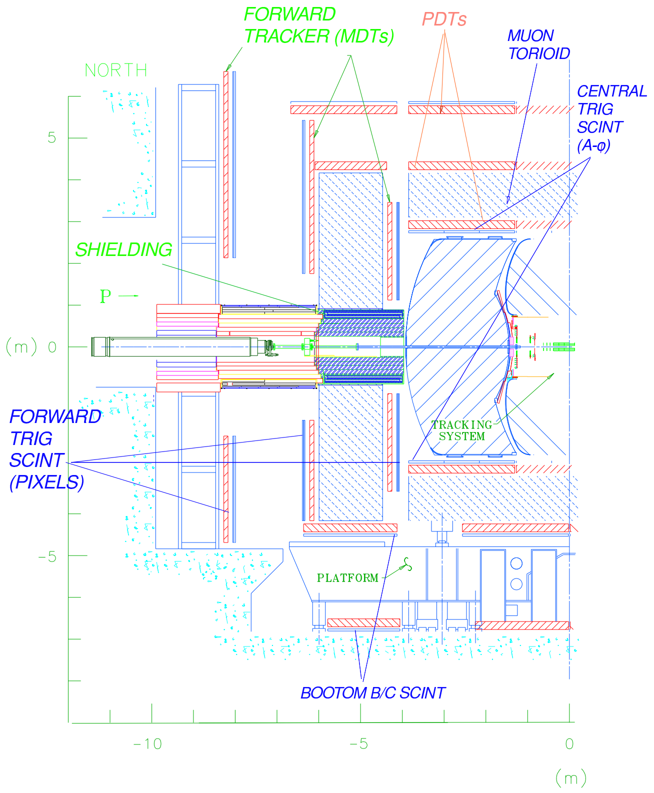

Figure 3.5: *Outline of the DØ muon system.*

3.2.4 The Luminosity Monitors

The amount of luminosity delivered by the Tevatron accelerator is measured by the luminosity monitors. Two hodoscopes built from plastic scintillators and read out by photomultiplier tubes are mounted on the end cap calorimeter cryostats (North and South). They cover a pseudo-rapidity range of $2.7 < |\eta| < 4.4$.

The luminosity is determined by triggering on beam crossings with non-diffractive inelastic $p\bar{p}$ interactions. The measurement of the time difference between signals from the north and south luminosity detector discriminates between a proton-antiproton interaction and beam halo. A beam proton will be measured in the south detector 9 ns after it was verified in the north detector and vice versa for anti-protons. Particles produced at the nominal interaction point inside the DØ detector will hit both luminosity detectors approximately at the same time. The time difference of both hits allows a fast measurement of the 0-vertex position.

The instantaneous luminosity is measured by the rate of inelastic collisions:

$$\mathcal{L} = \frac{1}{\sigma_{p\bar{p},\mathrm{eff}}} \frac{dN}{dt}(p\bar{p}) \tag{3.3}$$

with $\sigma_{p\bar{p},\mathrm{eff}} = \varepsilon_{\mathrm{LM}} \cdot A \cdot \sigma_{p\bar{p}}$. The luminosity detector efficiency $\varepsilon_{\mathrm{LM}}$ is extracted from data by studying the calorimeter energy in the cells directly behind the luminosity detectors, A corresponds to the luminosity detector acceptance determined using Monte Carlo and $\sigma_{p\bar{p}}$ is the inelastic $p\bar{p}$ cross-section measured by other experiments to be 60.7 ± 2.4 mb [25]. The overall estimated error on all these numbers, ie. the estimated error on the DØ luminosity, is 6.5% [26].

3.2.5 The Trigger and DAQ-System

The trigger and data acquisition system of the DØ detector is split into three levels. The input rate of 2.5 MHz given by the bunch crossing time of 396 ns is reduced by three consecutive trigger levels to an event rate of about 50 Hz which is written to tape. This rate reduction is necessary since not all events are interesting from the physics point of view and is also a financial and technical compromise since every event has a raw data size of about 250 kB which cannot be dealt with unfiltered. Figure 3.6 shows an outline of the Level 1 and Level 2 trigger system.

Instead of filtering and triggering on interesting physic objects like e.g. muons, electrons or jets, one can artificially reduce the bandwidth by randomly triggering on events. This method is called “pre-scaling” and is used e.g. in the commissioning phase of a newly integrated trigger or in certain jet cross-section measurements if the input rate is to high for the DAQ system. The difficulty is to choose a real random process for “pre-scaling” to be independent from any biases this might cause.

Level 1 trigger

The Level 1 trigger (L1) is a hardware and firmware system designed to reduce the input rate from 2.5 MHz to about 10 kHz. It consists of a L1 trigger framework and several subsystems which are closely connected to single sub-detectors. There are the L1 Muon system, the L1 Calorimeter trigger for electron, photon and jets, and L1 track trigger.

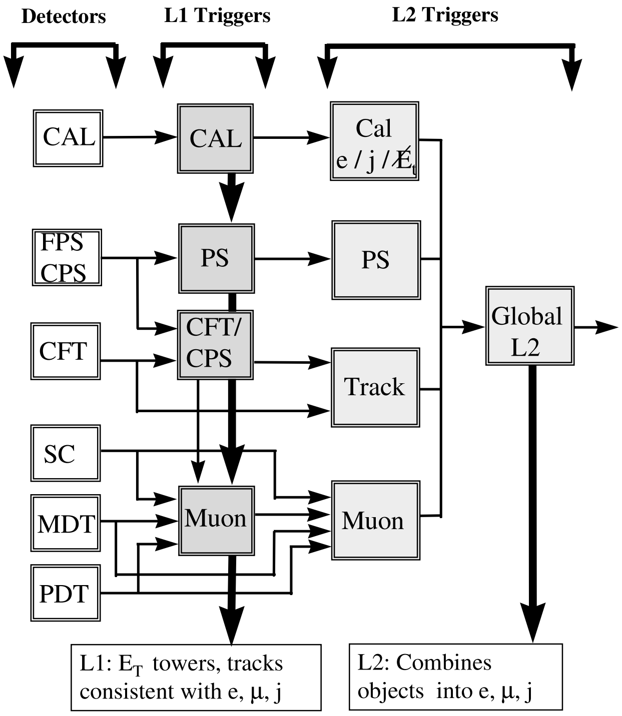

Figure 3.6: *Outline of the DØ trigger system.*

Level 2 trigger

The Level 2 trigger (L2) is the first trigger level for event-wide trigger decisions. There are similar to L1 sub-detector specific triggers which make their decision on a mixture of firmware and software information. There are systems for muons, electrons, jets and tracks. But the final trigger decision is made a central system which can combine all L2 information for a trigger decision. The Level 2 system reduces within 100μs the input rate in a pipe lined event queue by a factor of 10 to about 0.5 – 1 kHz.

Level 3 trigger

The Level 3 system is a software only system which reduces the event rate to about 50 Hz to tape. It performs event filtering with an optimised and simplified software which is similar to the reconstruction software used later for full event reconstruction. The software is run in parallel on 48 dual processor Linux farm nodes and has a processing time of about 100 ms per event. With this long time at hand various algorithms are used for all detected particles.

3.2.6 Muon Trigger

Events analysed in the subsequent sections are triggered and written to tape for offline analysis by finding muons hits in trigger level 1 or 2. For a small fraction of events a track with high transverse momentum is required in addition on trigger level 3.

Level 1 Muon

The Level 1 muon trigger at the stage used for the following analysis uses scintillator hits in the muon detectors to pass an event to the next trigger level. A co-incidence of two layers in the same region (central or forward muon system) and the same octant fulfil this trigger requirement. The scintillator times are calibrated such that a muon from a $p\bar{p}$ collision would reach them at a time $t = 0$. The trigger gate is defined by allowing only hits within $|t| < 20\,\mathrm{ns}$. Two of such muons are required to pass these quality criteria.

In addition the level 1 muon trigger can also use tracks that are found by the level 1 central fibre tracker trigger (L1CTT). This trigger uses predefined roads of the axial information of the CFT detectors to find tracks fast and efficiently. This information is passed on to the level 1 muon trigger to build co-incidences with hits found in the scintillator or wire chambers of the muon system.

For most of the time range of the analysed data sample an additional “fast-z” trigger is also required. To reject cosmic muons and random hits in the muon chambers a co-incidence of hits in the luminosity monitors, with no other sub-detector trigger requirements is used.

Level 2 Muon

For further bandwidth reduction of the very loose trigger requirement at trigger level 1, events are filtered for muons at trigger level 2. At this level complete timing information, including calibration constants for the wire proportional chambers and scintillator detectors are available. The information is fed on two separate paths into the level 2 muon system. On one path the information is read out directly from the different muon detector front ends [27]. The second path uses the level 1 muon trigger information which has additional information available from L1CTT. The hardware of the level 2 muon system consists of several signal reshaper and multiplexer on the detector front end readout side. All signals are fed into so called SLIC boards (Second Level Input Computer) which each host five 160 MHz Texas Instruments DSPs. There are eleven boards for the central muon system and five boards for the forward system. The Level 1 muon trigger inputs are unpacked and translated for the forward and central muon system on two of these SLIC boards. On the remaining SLIC boards different algorithms perform a muon track finding with the additional available information and larger time budget of approximately 30μs. Muon tracks are found by look up tables combining hits from the scintillator and wire chambers within the A layer or combined BC layer of the muon system. After that the information from the level 1 muon DSPs, A layer DSPs and BC layer DSPs, is gathered by two processor boards, the so called alpha boards, which are running 500 MHz DEC alpha processors. There is one board for the forward and one for the central muon system. Meanwhile these boards have been replaced by the so called beta boards, running faster Intel Pentium processors. All other sub-detectors, e.g. calorimeter or tracking, have corresponding alpha/beta boards with various trigger algorithms. The central trigger decision for level 2 is done by a separate alpha/beta boards running a global level 2 algorithm.

Events for the subsequent analysis are passed to trigger level 3, if one muon of medium quality is found at level 2. A 'medium' muon at level 2 has to meet the following quality requirements (at least "quality > 1") in the A layer and BC layer each: in the forward muon detector A layer a muon has to have at least 2 MDT chamber hits and at least 1 associated hit in the scintillator and in the BC layer a muon has to have at least 2 hits in the B or C layer where the muon has only hits in one of the two layers. In the central muon system a muon track has to have at least 3 PDT chamber hits with valid hit-pattern in the look-up table for the A- and BC-layer.

Level 3 Tracking

With the increasing instantaneous luminosity and better performance of the Tevatron accelerator a small fraction of events need to have an additional tracking requirement at trigger level 3. The triggers with muon requirements at trigger level 1 and 2 only, have been pre-scaled at periods with high ($\approx 40-50\cdot 10^{30}\mathrm{cm}^{-2}\mathrm{s}^{-1}$) instantaneous luminosities. To avoid conflicts with the pre-scaling system or to loose too many events, a track with high transverse momentum eventually coming from one of the already triggered muons is required to be in the event. With a time budget of approximately 100 ms at level 3, a reduced offline reconstruction software with all sub-detector information and calibration available is run on Linux computers. The tracking algorithm [28] first searches for CFT axial tracks and extrapolates them to CFT and SMT stereo clusters. Events are selected for the subsequent analysis if at least one global track with a transverse momentum of 5 GeV or 10 GeV depending on the run period is found.

4 Event selection

This Chapter gives an overview about the main ingredients of the two analyses on the search of the Higgs boson in Chapter 5 and the measurement of the WW cross-section in Chapter 6. The reconstruction of muons, jets and missing transverse energy $\not\!\!E_{\mathrm{T}}$ with the DØ detector are discussed together with efficiencies in data and Monte Carlo and issues of data and reconstruction quality.

4.1 Reconstruction

4.1.1 Muons

Muon tracks are reconstructed at a first stage from the hits in the muon detector scintillation counters and drift chambers. The quality criteria of the muon track are divided into three categories with increasing quality: loose, medium, and tight. A muon is called "tight" if it has at least two hits in the wire chambers in the A layer, at least one hit in the A layer scintillators, at least three hits in BC layer wire chambers, at least one BC layer scintillator hit, and a converged fit through the A and BC layer muon detector hits. A muon is called "medium" if it has at least two hits in the A layer wire chambers, at least one hit in the A layer scintillators, at least two hits in the BC layer wire chambers and at least one hit in the BC scintillator (except for central muons with less than four BC wire hits). A "loose" muon is defined as a medium muon but allowing one of the above tests to fail, with the A layer wire chamber and scintillator requirement treated as one test and requiring always at least one scintillator hit. All these criteria have hit requirements in the A and BC layers of the muon detectors. In addition a BC segment with match to a central track is called "loose" if has at least one BC layer scintillator hit and has at least two hits in the BC layer wire chambers. Similarly an A layer segment matched to a central track is called "loose" if it has an A scintillator hit and at least two hits in the A layer wire chambers.

After the reconstruction of the muon tracks in the muon detector only these tracks are matched to tracks from the central tracking system consisting of the Central Fibre Tracker

(CFT) and Silicon Micro-strip Tracker (SMT). A simultaneous “global” fit through all hits in three detector components provides the muon track information which is used in the following analysis. Since the intrinsic resolution of the central tracking system is much better than from the standalone muon system (see Section 3.2.1 and 3.2.3), only muons with a matching central track are retained. Events are required to have two loose muons which are matched to a central track.

The entire muon information is obtained from the software package `muo_evt` version `p14-br-05`, `muonid` version `p14-br-14` provided by the muon-ID group [29] and post processed by `d0correct` version `v00-00-06` provided by the common samples group [30].

There is a non negligible rate of muons from cosmic rays present in a fraction of events (the rate is estimated in Section 7.2). Muons from cosmic rays are rejected by a cut on the scintillator counter times in the A and BC layer. Both times should be in the range of $-10\,\text{ns} < t_0 < 10\,\text{ns}$. The scintillator times are calibrated such that a muon from a $p\bar{p}$ collision would reach them at a time $t = 0$.

To ensure the quality of the tracks, a cut on the minimum number of hits in the tracking system is required: all muon tracks must have at at least three hits in the silicon tracker (SMT). Figure 4.1 shows the number of hits in the silicon tracker (left) and central fibre tracker (CFT). It can be seen that in both distributions the Monte Carlo has a higher mean for the number of hits in both silicon and central fibre tracker. Most of the tracks with no hits in the silicon tracker do not originate from the nominal $p\bar{p}$-interaction region. It was studied if constraining tracks without silicon tracker hits to the nominal vertex position improves the statistics of selected muon events. The bad momentum resolution of these tracks distorted the correction of the missing transverse energy $\not{E}_T$ (see Section 4.4.7) and these tracks were rejected.

For further rejection of muons from cosmic rays and to ensure that the muon tracks are coming from the hard interaction at the nominal $p\bar{p}$ interaction point a cut on the distance of closest approach x_{DCA} of the track with respect to the reconstructed vertex is applied. The distance of closest approach should be smaller than $x_{\text{DCA}} < 0.15\,\text{cm}$.

The analysis in the subsequent chapters uses events with high transverse momentum muons. The transverse momentum p_T should be $p_T^{\mu 1} > 20\,\text{GeV}$ for the first muon and and $p_T^{\mu 2} > 10\,\text{GeV}$ for the second muon. These muons should also be isolated from jet activity. Two isolation criteria can be used to discriminate between isolated and non-isolated muons. Muons must fulfil the tracking isolation criteria, i.e. $\sum_{\text{tracks}}^{R<0.5} p_T < 4.0\,\text{GeV}$ (sum of the p_T of tracks in a cone $\Delta R < 0.5$ around the muon not including the muon track, where $R = \sqrt{\Delta\phi^2 + \Delta\eta^2}$). The calorimeter isolation $\sum_{\text{cells}}^{0.1<R<0.4} E_T < 2.5\,\text{GeV}$ (sum of the calorimeter cell transverse energies in a hollow cone with $0.1 < \Delta R < 0.4$ around the muon) is not used throughout the analysis. Since both muons are required to have a relatively large transverse momentum it was found that with the high tracking efficiency a tracking-only isolation is sufficient to reduce QCD and multi jet background. Figure 4.2

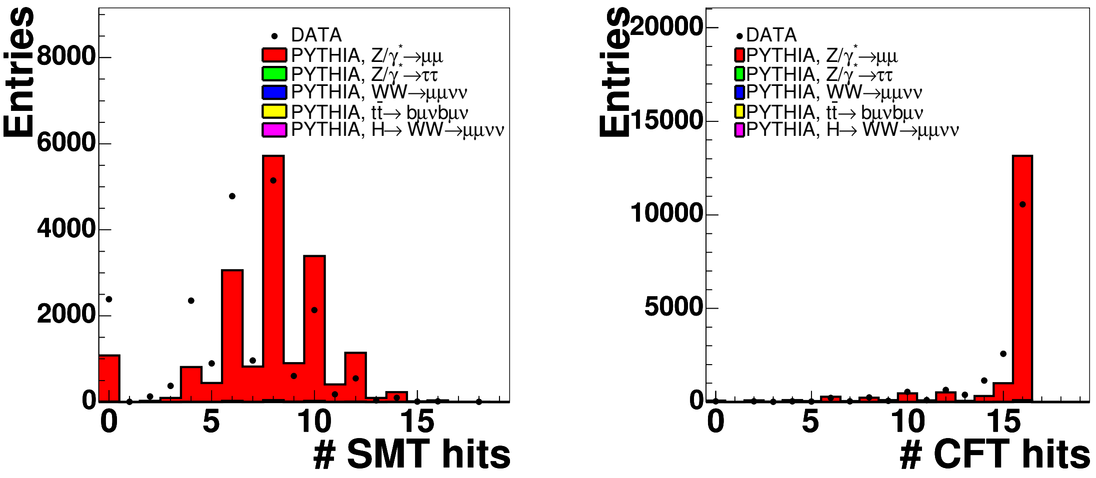

Figure 4.1: *Distribution of number of hits in the silicon tracker (left) and the number of hits in the central fibre tracker (right). The normalisation of the MC was obtained as described in Section 4.4.6.*

shows the distributions of both isolation definitions. The discrepancy between data and Monte Carlo at high values of the isolation variables is due to the missing Monte Carlo for QCD and multi-jet events.

4.1.2 Jets and Missing Transverse Energy $\not{E}_T$

Jets

Particle jets are reconstructed with the DØ calorimeter from the energy depositions in the calorimeter cells using a cone algorithm [31] with cone size $R = \sqrt{\Delta\phi^2 + \Delta\eta^2} = 0.5$ or 0.7. Jets are required to pass the following quality criterion:

- $0.5 < EM\ fraction < 0.95$, where $EMfraction$ is the fraction of the jet energy deposited in the electro-magnetic part of the calorimeter.
- $Coarse\ hadronic\ fraction(CHF) < 0.4$, where the coarse hadronic fraction is the fraction of energy deposited in the coarse hadronic layer of the calorimeter.
- $Hot\ fraction < 10.0$, where the Hot fraction is the ratio of energy of the highest to next-to-highest energy calorimeter tower.

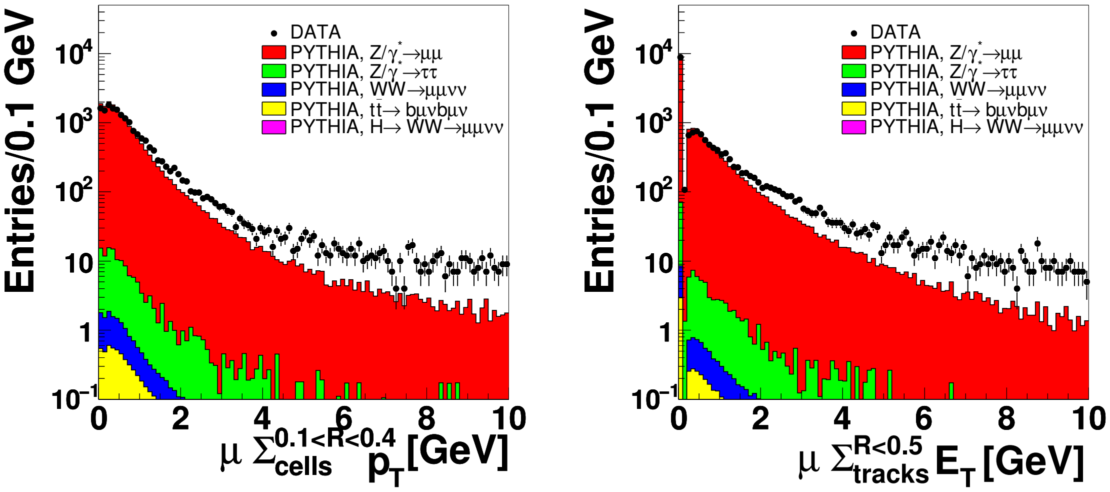

Figure 4.2: *Distribution of the calorimeter isolation (left) and the tracking isolation (right) of the muon track. The normalisation of the MC was obtained as described in Section 4.4.6.*

- $N_{90} > 1$, where N_{90} is the number of calorimeter towers containing 90% of the energy of a jet.

- $L1energy/(jetpt \cdot (1-CHF)) > 0.4$ for jets within $|\eta| < 0.8$ (CC region) or $|\eta| > 1.5$ (EC region) or > 0.2 within the ICD region of $0.8 < |\eta| < 1.5$. $L1energy$ is the energy measured by the Level 1 calorimeter trigger, which uses a different readout and calorimeter segmentation as the precision calorimeter measurement. $Jetpt$ is the transverse energy of the measured jet. This last quality criterion is applied to data events only, since the Level 1 response is not simulated.

- Jets should be within the validity region of the Jet energy scale correction: $|\eta| < 2.5$

Jet Energy Scale Correction

The discrepancy between the measured jet energy and the particle level jet energy is due to migrations into and out of the jet cone, collider effects and imperfections of the calorimeter measurement which cannot detect all energy deposits [32]. The collider environment can add additional energy in the calorimeter. This effect is often called "pile-up". The limited jet cone size can result into energy flows outside the jet boundary because of showering in the calorimeter. The particle jet energy $E_{\mathrm{Jet}}^{\mathrm{Particle}}$ is given in terms of the measured jet energy $E_{\text{Jet}}^{\text{Cal}}$ by:

$$E_{\text{Jet}}^{\text{Particle}} = \frac{E_{\text{Jet}}^{\text{Cal}} - E_{\text{offset}}}{R_{\text{Jet}} \cdot F_{\text{S}}}, \tag{4.1}$$

where E_{offset} is the energy offset correction which depends on the cone size R, the pseudo-rapidity η and the instantaneous luminosity. This term arises from the underlying event, pile-up in the calorimeter from previous bunch-crossings, additional minimum bias interactions per crossing and noise from the calorimeter uranium absorber. R_{Jet} is the jet response and the largest contribution to the correction of the jet energy. The jet response is mainly less that one due to dead calorimeter material, not instrumented regions, module differences. F_{S} is the showering correction that compensates for the energy flow out of the cone due to particle interaction with the calorimeter. This interaction subsequently forms showers of other particles depositing energy outside the original cone boundary.

Figure 4.3 shows the overall correction in data as function of the jet energy $E_{\text{Jet}}^{\text{Cal}}$ and the pseudo-rapidity η (left column) together with their corresponding errors (right column).

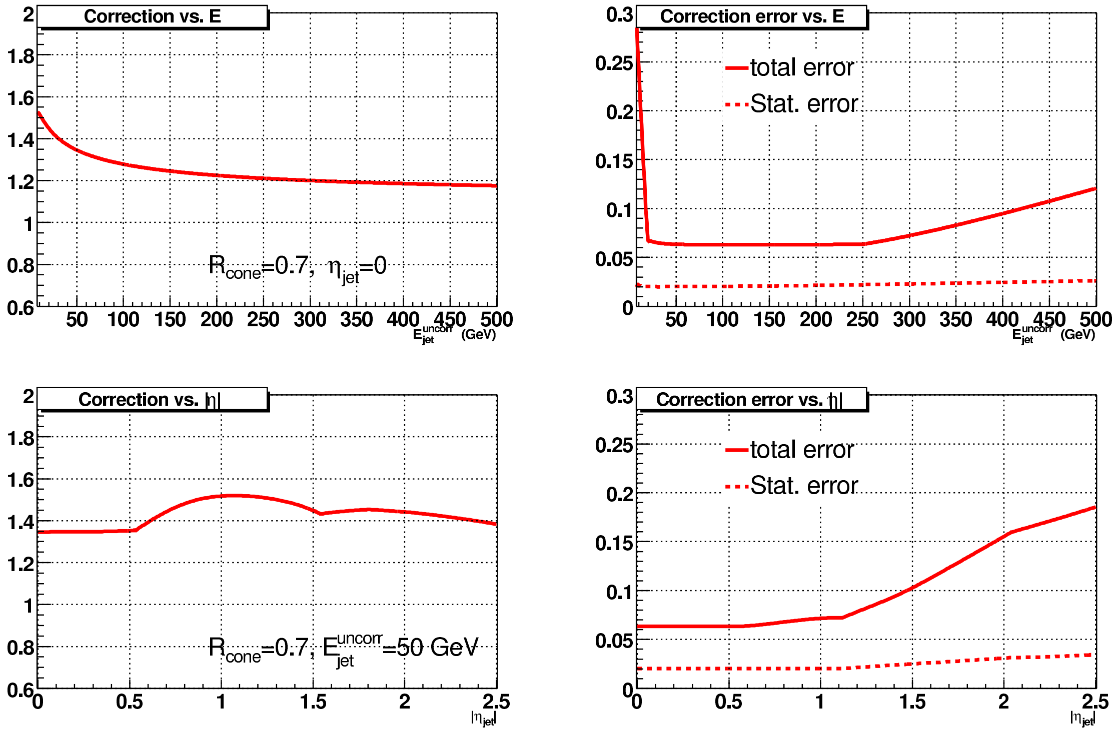

Figure 4.3: *Correction factors (left column) of the Jet Energy Scale versus E (top) and η (bottom) and their corresponding errors (right column). These correction apply for jets with $R = 0.7$. Similar factors apply for $R = 0.5$ cone jets [32].*

Missing transverse energy $\not\!\!E_T$

Following the latest recommendations of the DØ Jet/Missing Energy-ID group the missing energy is recalculated using all calorimeter cells with an energy above 0 MeV where the unclustered energy in the coarse hadronic layers (outer calorimeter layer 15-18) is excluded except for coarse hadronic cells which belong to a jet [33]. The calculation of $\not\!\!E_T$ includes all corrections for the coarse hadronic layer, electrons from jet removal, jet energy scale correction and muon corrections. The coarse hadronic layer has been partially removed from the $\not\!\!E_T$ calculation since it showed unstable behaviour due to noise that distorted the $\not\!\!E_T$ resolution or led to a wrong measurement of $\not\!\!E_T$. The jet energy scale correction is performed with the software package `jetcorr` version `v05-00-00`. The missing transverse energy $\not\!\!E_T$ is calculated using the software package `missingET` version `v00-06-10` and post processed by `d0correct` version `v00-00-06`. Every good jet as defined in previous Section with a cone radius of $R = 0.7$ is energy scale corrected. With this procedure a correction for the missing transverse energy in each event is obtained. In Run I the missing transverse energy correction based on $R = 0.7$ jets was preferred over correction through $R = 0.5$ jets, since the 0.7 cone jets gather significantly more energy than 0.5 cone jets, and therefore a substantially improved $\not\!\!E_T$ correction was available from them. Electrons can lead to a mis-measurement of jets and are therefore removed from jets before they are corrected for their jet energy scale.

The muon corrections include the following: the energy loss of muons in the calorimeter through ionisation is about 2 GeV, roughly independent of the muon momentum. Thus the calorimeter-only missing transverse energy must be corrected using the value of the momentum measured by the tracking system. The muon transverse momentum given by the tracking system is subtracted from the missing transverse energy. The value of the muon energy loss is obtained from an empirical function which parameterises the muon energy loss measured in test beam data. This value is added to the missing transverse energy taking into account the angular dependence. Only muons of the quality criteria discussed in Section 4.1.1 are used for this correction. They must have loose quality with track match and at least three hits in the silicon tracker with a distance of closest approach with respect to the vertex smaller than $0.15\,\mathrm{cm}$. For MC in addition to the above muon corrections the transverse momentum of the muon is smeared with the same function as described in Section 4.4.1.

4.2 Data Sample

The data used in the present analysis was collected by the DØ experiment between August 2002 and September 2003. Most of the available data are centrally reconstructed by the common reconstruction software “DØReco” on a Fermilab Computing Linux cluster.

The software versions p14.03.00/01/02, p14.05.00, p14.05.02 and p14.06.00 have been used. Some parts of the data have also been re-reconstructed from an older software version p13.06.00 at several remote sites throughout the world. Small improvements in reconstruction efficiency and speed have been made between these p14 versions. To have a common basis all available data from the first software version have been post-processed to fix some minor known issues that have been fixed with the latest software version. All event information is stored into a so called "TMB" (Thumbnail). This has the size of about 25 KB (Kilobyte) per event and stores the compressed information of physics objects, like kinematics, track quality, calorimeter cells and common event information like trigger status and detector status.

All data ($\approx$ 500 million events for this period) are skimmed to smaller subsamples based on physics objects like electrons, muons and jets with certain kinematic conditions. The "2MU" skim of the DØ common sample group provides a preselection for this analysis [30]. Events passing the preselection cuts have two "loose" muons without any requirement on the muon transverse momentum. The different muon quality criteria have been discussed in Section 4.1.1. These are approximately 25.9 million events.

4.2.1 Trigger Efficiency

The triggers used in this analysis are a logical OR of the four di-muon triggers which have been described in detail in Section 3.2.6. These triggers are the "unprescaled" triggers `2MU_A_L2M0`, `2MU_A_L2ETAPHI`, `2MU_A_L2M0_TRK10`, and `2MU_A_L2M0_TRK5`. They are a combination of a muon scintillator trigger at Level 1 (L1) and a medium muon trigger at Level 2 (L2). For the first two triggers there are no requirements for this trigger at Level 3. The last two triggers require a track with transverse momentum of $p_T > 5$ or $> 10\,\text{GeV}$, respectively. The latter two triggers were added since the first two triggers are prescaled in runs during July 2003 until September 2003 at high instantaneous accelerator luminosities.

The efficiencies at the different trigger levels are studied in the data in an unbiased sample of various calorimeter triggers. This set contains events that are triggered and recorded by high rate electromagnetic or jet triggers. Eventually muons are also found in these events. With these muons the trigger efficiency at the different trigger levels can be determined.

The efficiency at Level 1 is determined for reconstructed loose isolated offline muons having a track match (see Section 4.1.1) and with fired calorimeter triggers by dividing the number of events with a fired trigger `mu1ptxatxx` by the number of all calorimeter triggered events. The trigger term `mu1ptxatxx` refers to single muon trigger at level 1 with scintillator co-incidence over the full muon detector coverage. The top row in Figure 4.4 shows the Level 1 trigger efficiency versus the muon transverse momentum p_T, ϕ and η. The drop of the efficiency in the region $4.25 < \phi < 5.25$ is due to the missing scintillator detector coverage at the bottom of the DØ detector. An efficiency of $\varepsilon_a = 0.845 \pm 0.009$ is obtained for offline muons with $p_T > 10\,\mathrm{GeV}$.

The L2 medium muon trigger efficiency is determined by dividing the number of events with at least one medium muon at L2Global by the number of all calorimeter triggered events and a fired L1 trigger. The lower row in Figure 4.4 shows the Level 2 medium muon trigger efficiency versus versus the muon transverse momentum p_T, ϕ and η. Here the drop of efficiency in the region $4.25 < \phi < 5.25$ is due to missing events triggered by the Level 1 muon trigger. The efficiency sums up to $\varepsilon_b = 0.901 \pm 0.005$ for offline muons with $p_T > 10\,\mathrm{GeV}$.

Combining the two efficiencies the total efficiency for the di-muon trigger `2MU_A_L2M0` becomes $\varepsilon_{2MU\_A\_L2M0} = 0.76 \pm 0.02$. The additional trigger `2MU_A_L2ETAPHI` is required for a short data taking period of time where the trigger `2MU_A_L2M0` is prescaled (see Section 4.2.2). This trigger requires in addition to the requirements of the first trigger two muons at L2 with a separation in $\Delta\phi \approx 13.5^o$ and $\Delta\eta \approx 0.15$. The overall trigger efficiency is assumed to be similar within the error compared to efficiency of `2MU_A_L2M0` alone since the sample of events triggered by `2MU_A_L2ETAPHI` contribute to only about 5% of the whole data sample. The same assumption is made for the two additional triggers `2MU_A_L2M0_TRK10` and `2MU_A_L2M0_TRK5` which require an additional track with $p_T > 5\,\mathrm{GeV}$ or $p_T > 10\,\mathrm{GeV}$, since the trigger efficiency is measured with respect to a reconstructed offline muon with track match.

4.2.2 Luminosity

The integrated luminosity of the data set is determined using the `lm_access_pkg` software package provided by the luminosity ID group [34]. The recorded luminosity in good luminosity blocks for all four triggers is obtained for the whole data sample. Good luminosity blocks are measured in a time interval of about 1 min and indicate that no detector component was in a bad status from the electronics and readout point of view. Nevertheless, bad detector status due to noise or failed detector components are also discovered after data recording. To assure the data quality and to account for detector or reconstruction failures, runs which are classified *bad* for the muon system, tracking system (CFT and SMT), calorimeter (CAL) or $\not{E}_T$ reconstruction in the run quality database are rejected [35]. In addition the run ranges 174207 to 174217 and 172359 to 173101 are excluded because of problems with forward and central di-muon trigger system.

Table 4.1 shows the integrated luminosities for the four different triggers and the combined overall luminosity of all. A sum of all triggers is made since the trigger `2MU_A_L2M0` is prescaled at high instantaneous luminosities whereas the other three triggers stay unprescaled. Only events with one of these triggers and no prescale are retained. The last three triggers have a smaller integrated luminosity because they were introduced later into the trigger list.

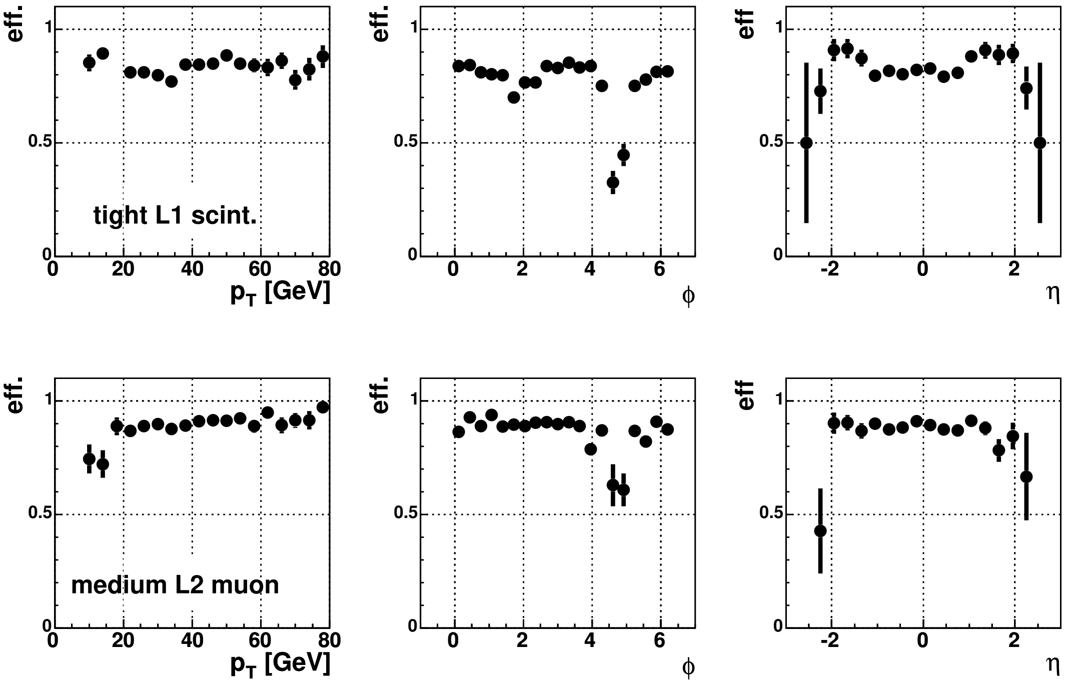

Figure 4.4: *The trigger efficiency for the Level 1 muon scintillator trigger (top row) versus the muon transverse momentum* p_{T}*,* ϕ *and* η*. The corresponding trigger efficiency for the Level 2 medium muon trigger is shown versus* p_{T}*,* ϕ *and* η *(bottom row).*

4.3 Monte Carlo Samples

Different Monte Carlo (MC) samples listed in Table 4.2 are used to study the signal and background distributions. All simulated events are generated using PYTHIA 6.202 [20] using the CTEQ4L parton distribution function [15]. They are processed through a full detector simulation using plate calorimeter geometry in version `p14.02.00`, `p14.03.02`, and `p14.05.02`. A Poisson-distributed average of 0.8 minimum bias events is overlaid. The cross-sections listed in Table 4.2 are taken from various sources: the NLO cross-sections for processes 1-6 are calculated using HDECAY [12] and HIGLU [11] with CTEQ5M parton distribution function and a top quark mass of $m_{\mathrm{t}} = 175\,\mathrm{GeV}$. The NLO cross-sections for processes 7 and 8 are taken from [13] and the cross-section for process 9 is taken from [16], and and process 10 are obtained from [36].

Further contributions from $b\bar{b}$-QCD background and W+jets production are studied in data and MC (see Section 5.2). The contribution of additional channels from $\Upsilon(1S)$, $\Upsilon(2S)$ and WZ production has been tested with large samples generated with PYTHIA

Trigger	$\mathcal{L}\,[\mathrm{pb}^{-1}]$
`2MU_A_L2M0`	131.4
`2MU_A_L2ETAPHI`	121.6
`2MU_A_L2M0_TRK10`	61.6
`2MU_A_L2M0_TRK5`	35.2
OR of all triggers	146.9

Table 4.1: *Integrated luminosity $\mathcal{L}$ for the trigger* `2MU_A_L2M0`, `2MU_A_L2ETAPHI`, `2MU_A_L2M0_TRK10` *and* `2MU_A_L2M0_TRK5`.

	Process	$\sigma \times BR$ [pb]	Generated Events
1	$H \to WW^{(*)} \to \mu^+\nu_\mu\mu^-\bar{\nu}_\mu$ ($m_\mathrm{H} = 100\,\mathrm{GeV}$)	0.00012	10000
2	$H \to WW^{(*)} \to \mu^+\nu_\mu\mu^-\bar{\nu}_\mu$ ($m_\mathrm{H} = 120\,\mathrm{GeV}$)	0.00095	10000
3	$H \to WW^{(*)} \to \mu^+\nu_\mu\mu^-\bar{\nu}_\mu$ ($m_\mathrm{H} = 140\,\mathrm{GeV}$)	0.00219	10000
4	$H \to WW^{(*)} \to \mu^+\nu_\mu\mu^-\bar{\nu}_\mu$ ($m_\mathrm{H} = 160\,\mathrm{GeV}$)	0.00269	10000
5	$H \to WW^{(*)} \to \mu^+\nu_\mu\mu^-\bar{\nu}_\mu$ ($m_\mathrm{H} = 180\,\mathrm{GeV}$)	0.00189	10000
6	$H \to WW^{(*)} \to \mu^+\nu_\mu\mu^-\bar{\nu}_\mu$ ($m_\mathrm{H} = 200\,\mathrm{GeV}$)	0.00104	10000
7	$Z/\gamma^* \to \mu^+\mu^-$	254	660715
8	$Z/\gamma^* \to \tau^+\tau^-$	254	305000
9	$WW \to \mu^+\nu_\mu\mu^-\bar{\nu}_\mu$	0.0145	20750
10	$t\bar{t} \to b\mu\nu b\mu\nu$	0.065	39000

Table 4.2: *Monte Carlo samples used in comparisons with data (see Section 5 and Section 6).*

as above. These samples showed negligible or no contribution already after the muon preselection described in Section 4.1.1.

4.4 Reconstruction Efficiencies

4.4.1 Muon Identification and Muon Momentum Smearing

Although there was a significant reconstruction quality improvement between the different reconstruction versions p13 and p14 by tracker realignment and improved tracking algorithms the muon momentum resolution, data and MC still differ. The resolution in MC is overestimated since not all dead material is properly simulated and a perfect alignment and ideal geometry of the tracking detectors are assumed in the simulation. Also the effect of temporarily dead readout channels cannot be properly handled. Figure 4.5

shows the distribution of the unsmeared invariant di-muon mass $m_{\mu\mu}$ (left) and the muon transverse momentum p_{T} of the first and second muon. The width of the Z resonance expected by Monte Carlo is ~ 6 GeV. Therefore, the Monte Carlo is tuned to describe the data by smearing the muon transverse momentum p_{T} with a smearing method following: $\frac{1}{p_{\mathrm{T}}} \rightarrow \frac{1}{p_{\mathrm{T}}}(1+fG)$, where $f = 0.00205$ is the smearing factor and G is a random variable with standard Gaussian distribution. In Figure 4.6 the result of this smearing is shown together with an additional tuning of the Monte Carlo normalisation. The latter will be discussed in Section 4.4.6.

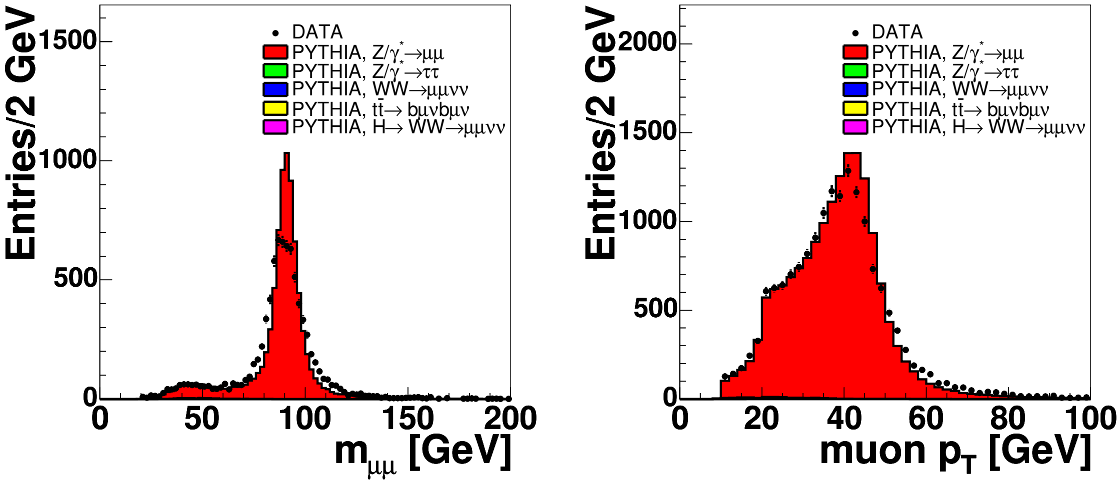

Figure 4.5: *Distribution of invariant di-muon mass (left) and the transverse muon momentum (right)* BEFORE *MC momentum smearing. The normalisation of the MC was obtained as described in Section 4.4.6.*

4.4.2 Tracking Efficiency

The efficiencies determined in the following sections are based on methods described in [37]. All efficiencies are determined using the previously described dataset and a $Z \rightarrow \mu^+\mu^-$ MC. To measure the tracking efficiency two loose muons are required to have a local muon transverse momentum $p_{\mathrm{T}} > 15\,\mathrm{GeV}$ determined standalone by the muon system. Both muons should be separated by $\Delta\phi > 2.5$ and isolated with calorimeter isolation $\sum_{\mathrm{cells}}^{0.1<\mathrm{R}<0.4} E_{\mathrm{T}} < 2.5\,\mathrm{GeV}$. The tracking times matching efficiency can be expressed as:

$$\varepsilon_{\mathrm{track\cdot match}} = \frac{N_1 + 2 \cdot N_2}{2(N_0 + N_1 + N_2)} \tag{4.2}$$

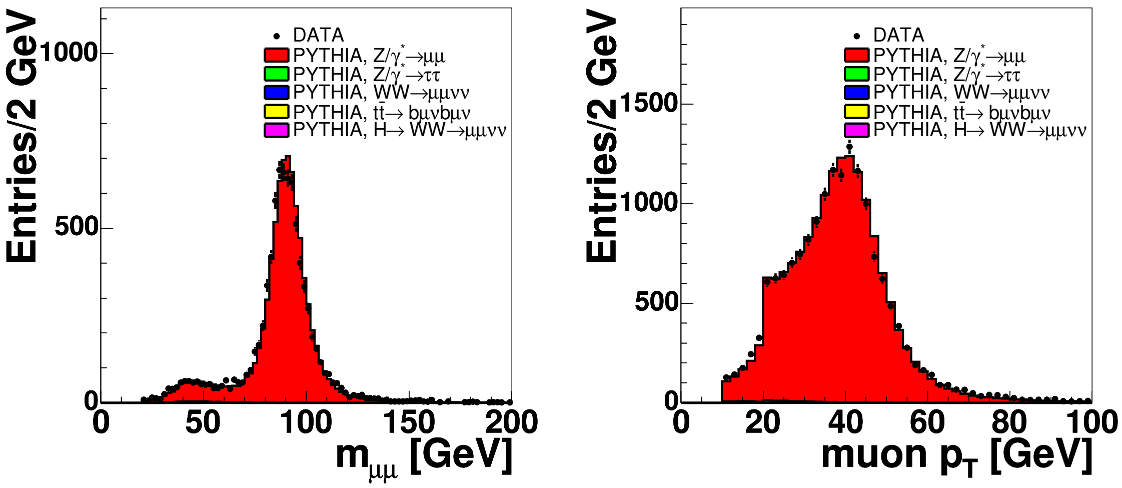

Figure 4.6: *Distribution of invariant di-muon mass (left) and the transverse muon momentum (right)* AFTER *MC momentum smearing. The normalisation of the MC was obtained as described in Section 4.4.6.*

where N_i is the number of events with $i = 0,1,\mathrm{or}\,2$ muons matched to a central track. Figure 4.7 shows the efficiency with respect to the muon transverse momentum p_T, η and ϕ. Averaging over all muons with $p_\mathrm{T} > 15\,\mathrm{GeV}$ the tracking efficiency is found to be $\varepsilon_{\mathrm{track,DATA}} = 0.928 \pm 0.008(stat.)$ for data and $\varepsilon_{\mathrm{track,MC}} = 0.961 \pm 0.005(stat.)$ for MC. The drop of the efficiency for values $|\eta| > 1.62$ is due to the missing central fibre tracker coverage in this region. Here tracks are reconstructed with the silicon tracker and only parts of the CFT. In the full CFT coverage range of $|\eta| < 1.62$ the tracking efficiency for data reaches a value of $\varepsilon_{\mathrm{track,DATA}} = 0.95 \pm 0.01(stat.)$. The drop of the efficiency in ϕ around 4.5 is due to the missing events that are not triggered by the Level 1 muon trigger in bottom hole of the muon detector.

4.4.3 Muon Reconstruction Efficiency

The efficiency to reconstruct a loose muon is determined with the help of muons identified with the calorimeter. Muons traverse the calorimeter in a straight line with a constant energy loss of approximately $2\,\mathrm{GeV}$. The reconstruction and identification efficiency especially in a jet environment is not efficient enough to include these calorimeter muons to the following analyses. One muon is required to be loose and matched to a central track with a transverse momentum $p_\mathrm{T} > 20\,\mathrm{GeV}$ whereas the second muon with a transverse momentum $p_\mathrm{T} > 10\,\mathrm{GeV}$ is tested whether it is loose or not. Both muons should be separated by $\Delta\phi > 2.5$. The events have to be triggered by the muon trigger described in Section 4.2.1.

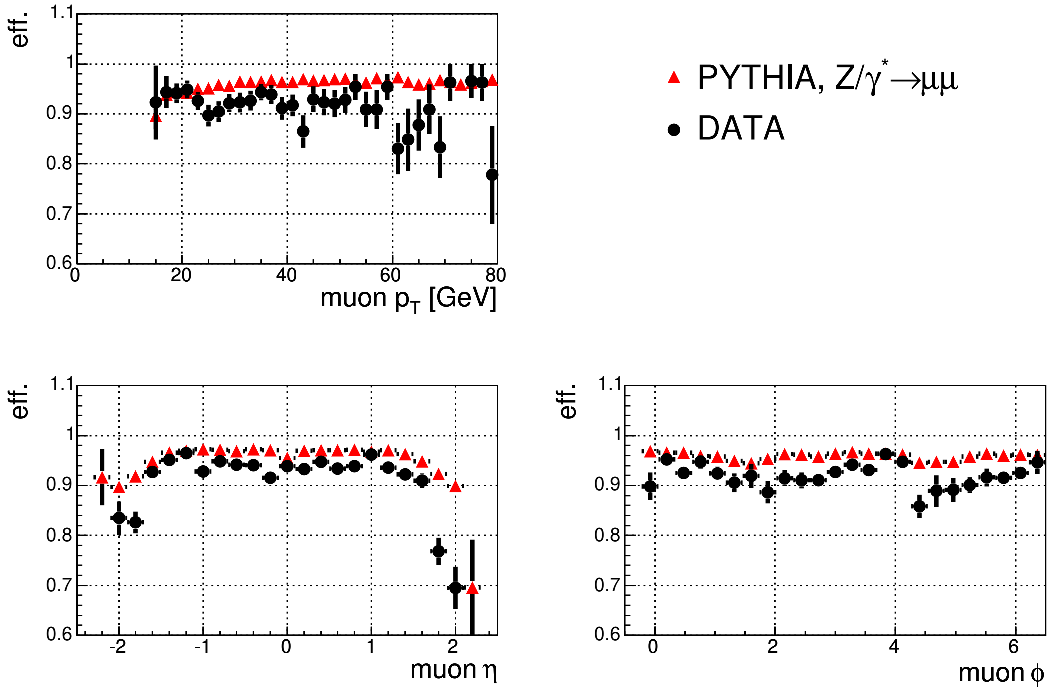

Figure 4.7: *The muon tracking efficiency determined in data (black dots) and Monte Carlo (red triangles)*

Averaging over ϕ of the muon and excluding the bottom acceptance gap $4.25 < \phi < 5.15$, the loose muon reconstruction efficiency is found to be $\varepsilon_{\mathrm{loose,DATA}} = 0.91 \pm 0.01(stat.)$ in data and $\varepsilon_{\mathrm{loose,MC}} = 0.90 \pm 0.01(stat.)$ for MC. Exchanging the cut on the muon transverse momenta yields the same efficiencies. Figure 4.8 shows the efficiency with respect to the muon transverse momentum p_{T}, η and ϕ. The drop of the efficiency in ϕ between $4 < \phi < 5.5$ is due to missing muon detector coverage in the bottom part which has been excluded from the quoted efficiencies as described above.

4.4.4 Muon Isolation Efficiency

The muon isolation efficiency is determined in data and MC with events coming from Z decays. Two loose muons matched to a central track are required to have a transverse momentum $p_{\mathrm{T}} > 15\,\mathrm{GeV}$ and need to be separated by $\Delta\phi > 2.5$. In the mass window $70\,\mathrm{GeV} < m_{\mu\mu} < 110\,\mathrm{GeV}$, one muon is required to be isolated according to $\sum_{tracks}^{R<0.5} p_{\mathrm{T}} < 4.0\,\mathrm{GeV}$. The second muon is tested whether it fulfils the isolation criterion. Figure 4.9 shows the efficiency with respect to the muon transverse momentum p_{T}, η and ϕ. The

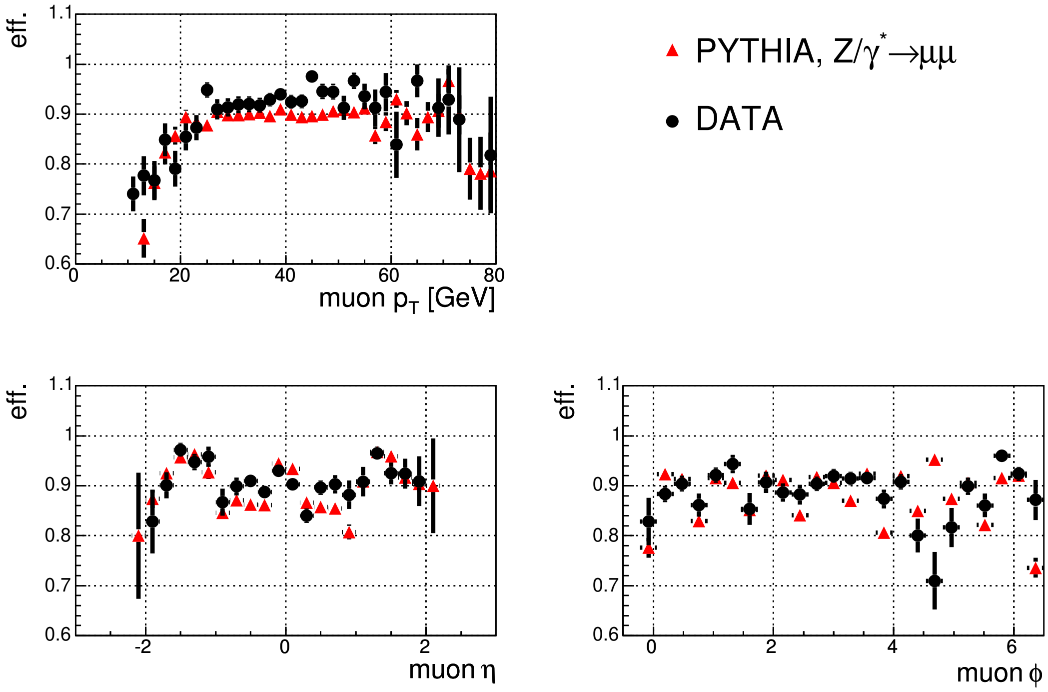

Figure 4.8: *The muon reconstruction efficiency determined in data (black dots) and Monte Carlo (red triangles)*

efficiency obtained is higher when the tested muon has a larger transverse momentum than the reference muon and vice versa. Averaging over all muons with $p_T > 15\,\mathrm{GeV}$ the muon isolation efficiency becomes $\varepsilon_{\mathrm{iso,DATA}} = 0.97 \pm 0.01(stat.)$ in data and $\varepsilon_{\mathrm{iso,MC}} = 0.98 \pm 0.01(stat.)$ for MC.

4.4.5 Remaining Efficiencies

Only events with two muons of opposite charge are retained in the following analysis. This efficiency is determined to $\varepsilon_{\mathrm{q,DATA}} = 0.99 \pm 0.01(stat.)$ [38] by selecting the number of events that are rejected by a like-sign charge cut for two muons in the invariant mass range around the Z peak. Cosmic muons are rejected with the standard muon-ID group cut on the scintillator times. This efficiency is determined to be $\varepsilon_{\mathrm{q,DATA}} = 0.995 \pm 0.005(stat.)$ [38] by selecting acolinear tracks with high scintillator times Δt.

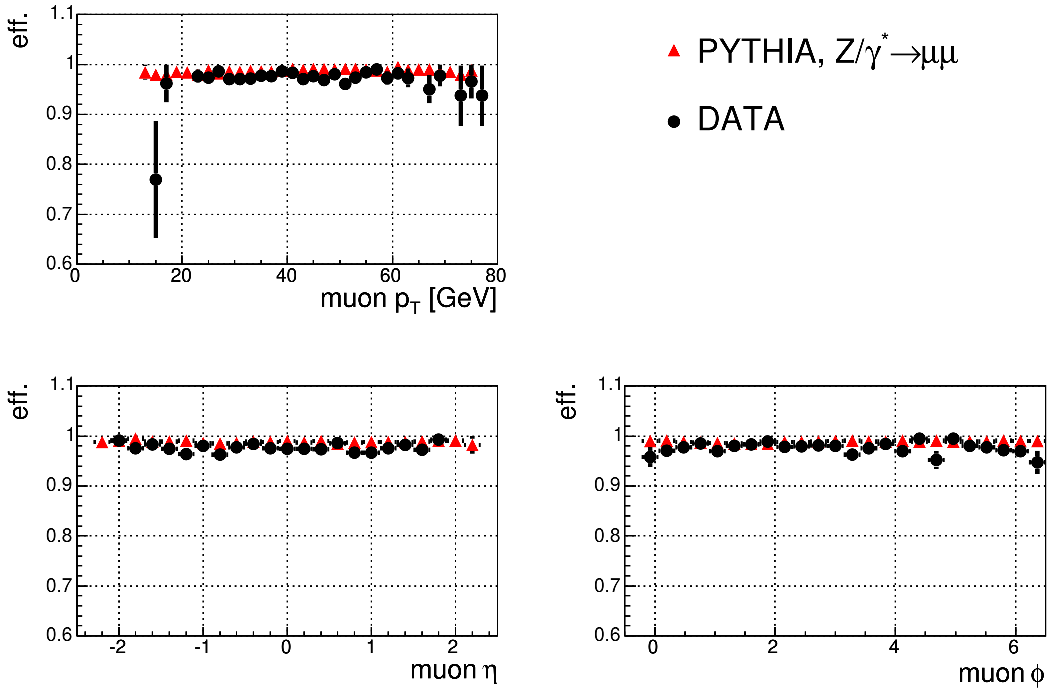

Figure 4.9: *The muon isolation efficiency determined in data (black dots) and Monte Carlo (red triangles)*

4.4.6 Monte Carlo Normalisation and Efficiency

As seen in the previous sections the efficiencies for data and MC differ in various aspects. Two methods have been used to obtain a proper normalisation of the MC with respect to the data.

The well measured process $Z/\gamma^* \to \mu^+\mu^-$ is used in a mass range of $60 - 120\,\text{GeV}$ to determine a scaling factor for all Monte Carlo samples. The leading order Monte Carlo program PYTHIA predicts a cross-section value of $\sigma \cdot BR \approx 180$ pb for this process. In Run I the DØ experiment has measured a value of $\sigma_{ee} = (218 \pm 11 \pm 12)$ pb [39] for $Z \to e^+e^-$ decays. Taking into account the higher centre-of-mass energy $\sqrt{s}$ leads to a scaling factor of $f_s = 1.19$ [40] for the measured cross-section. Fitting the $Z/\gamma^* \to \mu^+\mu^-$ Monte Carlo with a cross-section of ~ 260 pb in the mass range between $60 - 120\,\text{GeV}$ to the data leads to a scaling factor for all Monte Carlo normalisation $f_{\text{MC}} = 0.61 \pm 0.07$. This factor has to be applied to the MC normalisation to compensate the data and MC reconstruction differences. The error of the scaling factor f_{MC} is a combination of the errors of the σ_{ee} measurement, the determination of f_s and the muon momentum smearing. This scaling factor is applied to all Monte Carlo samples subsequently.

A second method uses the different efficiencies determined in the previous sections. The reconstruction efficiency for process $Z/\gamma^* \rightarrow \mu^+\mu^-$ is given by:

$$\varepsilon_Z = \varepsilon_{\text{acc}} \cdot \varepsilon_{\text{trig}} \cdot \varepsilon_{\text{iso}}^2 \cdot \varepsilon_{\text{track}}^2 \cdot \varepsilon_{\text{loose}}^2 \cdot \varepsilon_{\text{cosm}} \cdot \varepsilon_{\text{q}} \tag{4.3}$$

where $\varepsilon_{\text{acc}} = 0.42 \pm 0.01$ [38] denotes the geometrical acceptance and all other values are defined as in the previous sections. This leads to an overall efficiency $\varepsilon_{Z,DATA} = 0.214 \pm 0.012$ in data. Assuming a trigger efficiency of 0.92 ± 0.01 for a $Z/\gamma^* \rightarrow \mu^+\mu^-$ MC an efficiency of $\varepsilon_{Z,MC} = 0.264 \pm 0.016$ is found. The scaling factor for the MC normalisation follows to be $f_{\text{MC}} = 0.60 \pm 0.04$ which is in good agreement with the value obtained with the first method.

4.4.7 Quality of the Missing Transverse Energy $\not\!\!E_{\text{T}}$

Figure 4.10 shows the distribution of missing transverse energy $\not\!\!E_{\text{T}}$ for events with two isolated loose muons each matched to a central track and with a transverse momentum $p_{\text{T}}^{\mu 1} > 20\,\text{GeV}$ and $p_{\text{T}}^{\mu 2} > 10\,\text{GeV}$. There is good agreement between data and MC. It is particularly important to assure the quality of the muon tracks which is done by a cut on the minimum number of SMT hits and distance of closest approach to the vertex. A bad muon momentum resolution distorts the $\not\!\!E_{\text{T}}$ correction as mentioned in the previous sections.

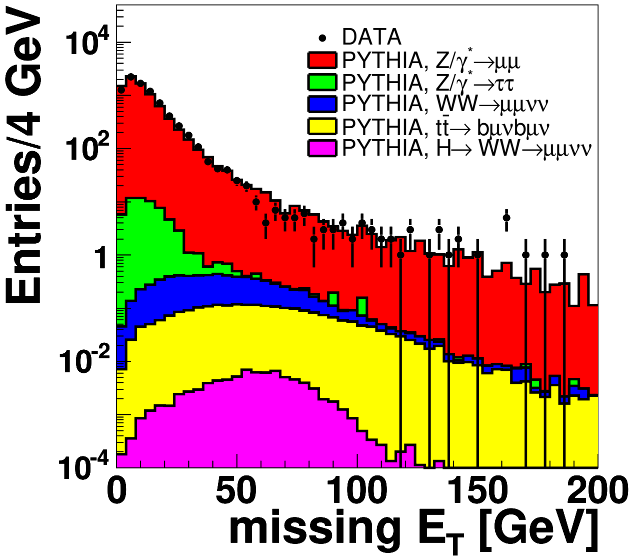

Figure 4.10: *Distribution of the missing transverse energy* $\not\!\!E_{\text{T}}$

5 Limits on $H \to WW^{(*)}$ Production

This Chapter describes the search for the Higgs boson in $H \to WW^{(*)}$ decays. Here, the decay channel of the Ws into two muons and two neutrinos is investigated in detail. At the end of this Chapter a combination with the di-electron and electron-muon decay channel of the Ws is presented.

5.1 $H \to WW^{(*)} \to \mu^+\nu_\mu\mu^-\bar{\nu}_\mu$ Selection

Main Selection Cuts

In Chapter 4 different aspects of muon reconstruction and data quality have been discussed. The event topology of $H \to WW^{(*)} \to \mu^+\nu_\mu\mu^-\bar{\nu}_\mu$ decays is characterised by two isolated muons with high transverse momentum p_T and significant missing transverse momentum $\not{E}_\mathrm{T}$ from the undetected neutrinos. There are several processes that have a similar event topology: $Z/\gamma^* \to \mu^+\mu^-$, $Z/\gamma^* \to \tau^+\tau^-$, $WW \to \mu^+\nu_\mu\mu^-\bar{\nu}_\mu$, $t\bar{t} \to b\mu\nu b\mu\nu$ and some $b\bar{b}$ and W+jets production. To discriminate between signal and background contributions various cuts are applied. The reduction of backgrounds from $Z/\gamma^* \to \mu^+\mu^-$ and $b\bar{b}$ and W+jets production is limited by experimental constraints like the muon momentum or missing transverse momentum resolution. In Chapter 5.2 it will be shown that the latter two backgrounds show negligible contributions. There are also "irreducible" backgrounds like $WW \to \mu^+\nu_\mu\mu^-\bar{\nu}_\mu$ production which distinguishable in a combination of kinematic variables from $H \to WW^{(*)} \to \mu^+\nu_\mu\mu^-\bar{\nu}_\mu$ production. For a Higgs mass of $m_\mathrm{H} = 160\,\mathrm{GeV}$, Figure 5.1 shows distributions of a few kinematic quantities that will help to reduce the contribution of different background processes. The transverse momenta of the decay products are expected to be mainly equally distributed, i.e. the sum of the two muon transverse momenta is about half of the Higgs boson mass if it is produced at rest and the undetected neutrinos (c.f. the missing transverse energy $\not{E}_\mathrm{T}$) carry the remaining part. The range of the invariant mass calculated from the two muons will be limited between the di-muon resonances of the Υ and the Z boson. The main background from $Z/\gamma^* \to \mu^+\mu^-$ production shows a large azimuthal opening angle of the two muons. Muons from this background tends to be rather back to back compared the muons from

$H \to WW^{(*)} \to \mu^+\nu_\mu\mu^-\bar{\nu}_\mu$ production. Figure 5.1 (a) shows the distribution of the leading muon transverse momentum p_T, (b) shows the invariant di-muon mass $m_{\mu\mu}$, (c) shows the missing transverse energy $\not{E}_T$, (d) shows the azimuthal opening angle $\Delta\phi_{\mu\mu}$ between the two muons, and (e) shows the distribution of the transverse momentum p_T of the leading jet. The different distributions of the Higgs signal Monte Carlo simulation (MC) are compared to MC from different background processes with the most discriminate power in this variable. For better visibility the normalisation for all distributions is arbitrarily chosen.

Selected events must have been triggered by the four "unprescaled" di-muon triggers described in Section 4.2.1. Furthermore events should have two opposite charged muons fulfilling the requirements of quality and isolation as described in Section 4.1.1: the muons are of loose quality with a matching central track, isolated by $\sum_{\text{tracks}}^{R<0.5} p_T < 4.0\,\text{GeV}$, have at least three hits $N_{\text{SMT}} \geq 3$ in the silicon tracker and are coming from the nominal vertex region with a distance of closest approach with respect to the vertex of $x_{\text{DCA}} < 0.15\,\text{cm}$. In addition the transverse momentum p_T for the leading muon must be $p_T^{\mu 1} > 20\,\text{GeV}$ and for the trailing muon $p_T^{\mu 2} > 10\,\text{GeV}$. To enhance the ratio of signal over background, a successive list of cuts is applied (see Table 5.1). During the development of this analysis a large amount of cuts on kinematic variables, angular correlations and event shapes has been tried. In the following cuts are presented that give the best signal efficiency and background suppression.

The major background source after the preselection is the $Z/\gamma^* \to \mu^+\mu^-$ production. To reduce this background, two cuts on the invariant mass $m_{\mu\mu}$ are applied: $m_{\mu\mu} > 20\,\text{GeV}$ and $|m_{\mu\mu} - m_Z| > 15\,\text{GeV}$. The first cut suppresses events with two muons from Υ decays, the second cut suppresses events from Z production (see Figure 5.2). The cut value of 15 GeV is approximately two times the measured width of the Z-resonance. For higher masses of the Higgs boson this cut will be responsible for a slight loss of signal efficency. For low Higgs masses the cut $m_{\mu\mu} > 20\,\text{GeV}$ is responsible for most of the signal efficiency loss. This cut cannot be lowered since events from Υ and $b\bar{b}$ decays significantly contribute to the region $m_{\mu\mu} < 20\,\text{GeV}$.

Cut name	Cut range
Di-Muon mass	$m_{\mu\mu} > 20\,\text{GeV}$ and $\lvert m_{\mu\mu} - m_Z\rvert > 15\,\text{GeV}$
Missing transverse energy $\not{E}_T$	$\not{E}_T > 30\,\text{GeV}$
Mismeasured $\not{E}_T$:	$\not{E}_T > 0.75 \cdot p_T^{\mu 1} + 10\,\text{GeV}$
Muon opening angle:	$\Delta\phi_{\mu\mu} < 2.0$
Jet p_T ($\lvert\eta^{\text{Jet}}\rvert < 2.5$)	$p_T^{\text{Jet1}} < 60\,\text{GeV}$, $p_T^{\text{Jet2}} < 30\,\text{GeV}$

Table 5.1: *Summary of signal selection cuts for $H \to WW^{(*)} \to \mu^+\nu_\mu\mu^-\bar{\nu}_\mu$ production.*

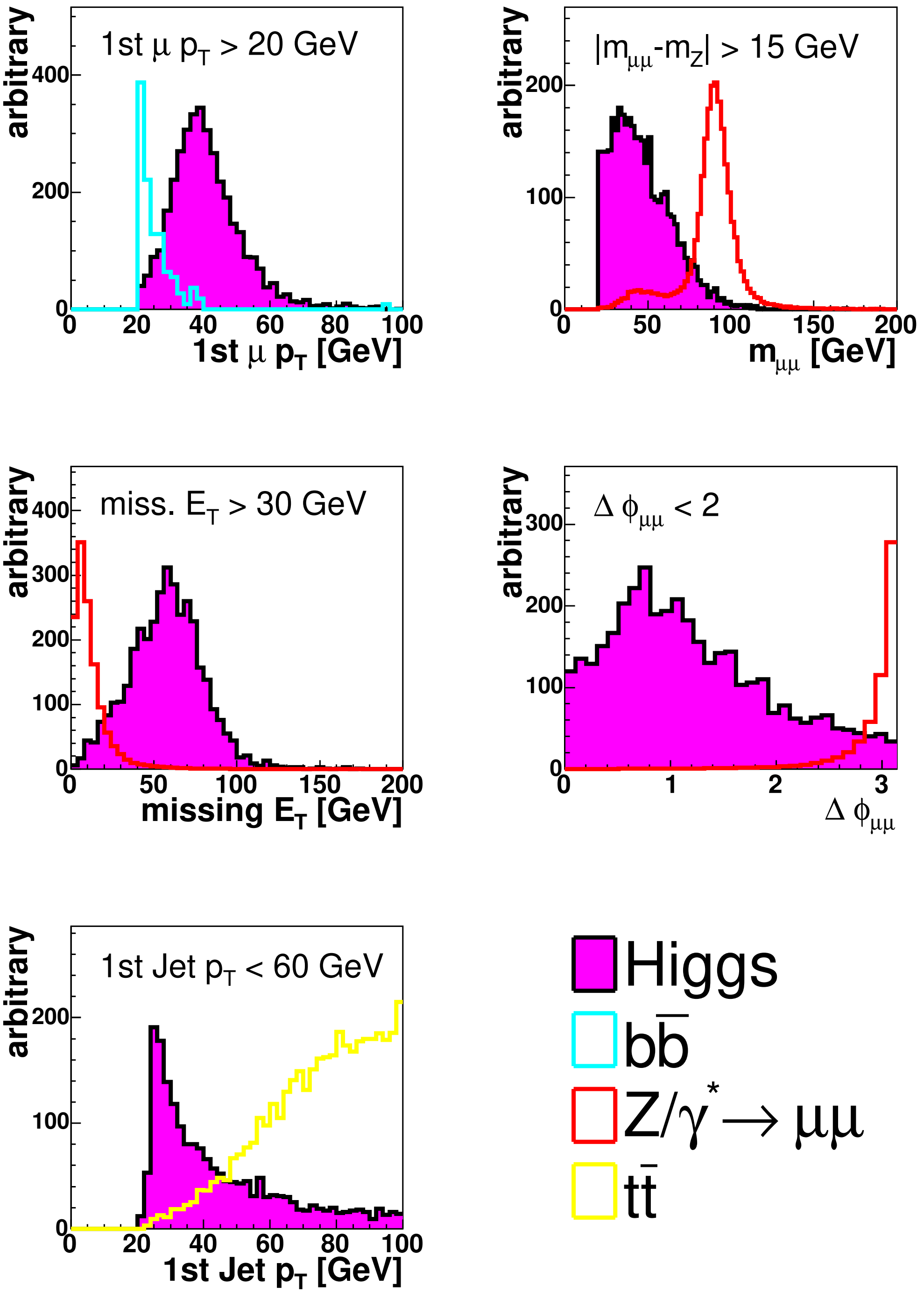

Figure 5.1: *Distributions of the* $H \to WW^{(*)} \to \mu^+\nu_\mu\mu^-\bar{\nu}_\mu$ *signal Monte Carlo for a Higgs mass* $m_\mathrm{H} = 160\,\mathrm{GeV}$ *and different background processes: the muon transverse momentum* p_T *(a), the invariant di-muon mass* $m_{\mu\mu}$ *(b), the missing transverse energy* $\not{E}_\mathrm{T}$*in the event (c), the opening angle* $\Delta\phi_{\mu\mu}$ *between the two muons in the azimuthal plane, and the the distribution of the transverse momentum* p_T *of the leading jet (e). The different cuts are used in the following analysis in Chapter 5. The distributions have arbitrary normalisation.*

$H \to WW^{(*)} \to \mu^+\nu_\mu\mu^-\bar{\nu}_\mu$ decays have a significant fraction of missing transverse energy $\not{E}_\mathrm{T}$ in the events from undetected neutrinos. Therefore a value of $\not{E}_\mathrm{T} > 30\,\mathrm{GeV}$ is required (see Figure 5.3). This cut effectively removes events from $Z/\gamma^* \to \mu^+\mu^-$ and $Z/\gamma^* \to \tau^+\tau^-$ production. Mis-measured muons wrongly indicate a larger missing transverse momentum $\not{E}_\mathrm{T}$. To further reduce these backgrounds with mis-measured muon transverse momentum, a cut in the two dimensional plane between the muon with the highest transverse momentum and the missing transverse energy $\not{E}_\mathrm{T}$ is applied: $\not{E}_\mathrm{T} > 0.75 \cdot p_\mathrm{T}^{\mu 1} + 10\,\mathrm{GeV}$ (see Figure 5.4).

Spin Correlation of the WW-system

The Standard Model Higgs boson has spin zero, whereas the $W^\pm$ bosons have spin 1. In order to conserve angular momentum, the spins of the $W^\pm$ bosons from $H \to WW^{(*)}$decays must be anti-correlated. In the Higgs rest-frame (which is for the considered mass range of the Higgs boson practically the lab frame) the decay axis of the WW-system is denoted as the z-axis. Along this axis, the W-spins are quantised by $S_3(W) = \pm 1, 0$ and are the transverse (T) and longitudinal (L) polarisation direction. Only the decays $H \to W_\mathrm{T}^+ W_\mathrm{T}^-$ and $H \to W_\mathrm{L}^+ W_\mathrm{L}^-$ are allowed, whereas $H \to W_\mathrm{T}^\pm W_\mathrm{L}^\mp$ is forbidden.

The $W^\pm$ polarisations are not directly observable, but can be observed through the final state leptons. The decay rate of $W_\mathrm{T}^+ \to \mu^+\nu_\mu$ is proportional to $(1 + \cos\vartheta)^2$, where ϑ is the angle of the muon momentum vector $\vec{p}_\mu$ with respect to the W_T^+ spin direction. Thus the right-handed positively charged muon is preferentially emitted into the W_T^+ spin direction. In contrast, the left-handed negatively charged muon is emitted in the opposite W_T^- spin direction following a $(1 - \cos\vartheta)^2$ dependence. Since the W boson spins are anti-correlated the momentum vectors of both muons point into the same direction.

The angular dependence of the muons from $W_\mathrm{L}^\pm$ decays follows $\sin^2\vartheta$, where ϑ is the angle of the muon momentum vector $\vec{p}_\mu$ with respect to the z-axis. The muons are most likely emitted perpendicular to the z-axis. If the W boson decays were uncorrelated there would be no particular correlation between the two muon momentum directions. However, they are correlated and their decay rate is proportional to $(\mu^- \cdot \nu_\mu)(\mu^+ \cdot \bar{\nu}_\mu)$, where the particle symbols correspond to the four-momenta of the particles [41]. This product is zero for anti-parallel muon and anti-muon three-momenta and has its maximum for parallel momenta, just as in the $W_\mathrm{T}^+ W_\mathrm{T}^-$ case. Overall a small opening angle of the muon and anti-muon momenta is expected.

Since the spins from the two decaying Ws originating from the Higgs decay are correlated, the opening angle between the two muons tends to be smaller as compared to events from background sources. The distribution of the opening angle $\Delta\phi_{\mu\mu}$ in the transverse plane is a good discriminant between events from Higgs decays and background contribution (see Figure 5.5). A cut on $\Delta\phi_{\mu\mu}<2.0$ significantly suppresses background contributions from almost all channels.

Further Selection Cuts

Multi-jet events, mostly originating from $t\bar{t}$ production, are rejected by applying a cut on the jet transverse momentum. Jets with the highest and second highest value of p_T^{Jet} should fulfil: $p_T^{\mathrm{Jet1}} < 60\,\mathrm{GeV}$ and $p_T^{\mathrm{Jet2}} < 30\,\mathrm{GeV}$. All jets are required to be in the validity range of the jet energy scale correction of $|\eta^{\mathrm{Jet}}| < 2.5$ and should have a transverse momentum of $p_T^{\mathrm{Jet1}} > 20\,\mathrm{GeV}$. (see Figure 5.6 and Figure 5.7).

Figure 5.8 demonstrates the importance of a well measured muon track momentum from which $\Delta\phi_{\mu\mu}$ is directly calculated and a well understood missing transverse energy $\not{E}_T$. Tails from mis-measurements in both variables badly influence the signal to background ratio. This is best seen in the $Z/\gamma^* \to \mu^+\mu^-$ distribution (right plot in the top row) which is the dominant background throughout this analysis also because of its high production cross-section.

Table 5.2 shows the signal efficiency for the process $H \to WW^{(*)} \to \mu^+\nu_\mu\mu^-\bar{\nu}_\mu$ for different Higgs masses derived from Monte Carlo with full detector simulation. Most of the efficiency is already lost in selecting two isolated loose muons with a transverse momentum $p_T > 10\,\mathrm{GeV}$ and $p_T > 20\,\mathrm{GeV}$ within the detector acceptance region. The following cut on the missing transverse energy $\not{E}_T$ reduces the signal efficiency by about 0.1 but has an high impact on the number of selected events from $Z/\gamma^* \to \mu^+\mu^-$ production (c.f. Table 5.6). All successive cuts reduce the efficiency by about 0.02 each.

Cut / m_H	100 GeV	120 GeV	140 GeV
μ-ID/ p_T	0.150 ± 0.004	0.253 ± 0.005	0.318 ± 0.006
$\not{E}_T$ & $\not{E}_T$ vs. $p_T^{\mu 1}$	0.064 ± 0.004	0.153 ± 0.005	0.208 ± 0.006
$m_{\mu\mu}$	0.064 ± 0.003	0.153 ± 0.005	0.202 ± 0.005
$\Delta\phi_{\mu\mu}$	0.053 ± 0.003	0.131 ± 0.004	0.177 ± 0.005
Jet p_T	0.045 ± 0.002	0.110 ± 0.003	0.150 ± 0.004

Cut / m_H	160 GeV	180 GeV	200 GeV
μ-ID/ p_T	0.370 ± 0.007	0.375 ± 0.007	0.410 ± 0.007
$\not{E}_T$ & $\not{E}_T$ vs. $p_T^{\mu 1}$	0.281 ± 0.006	0.274 ± 0.005	0.274 ± 0.005
$m_{\mu\mu}$	0.274 ± 0.006	0.238 ± 0.005	0.212 ± 0.005
$\Delta\phi_{\mu\mu}$	0.257 ± 0.005	0.221 ± 0.005	0.190 ± 0.004
Jet p_T	0.216 ± 0.004	0.179 ± 0.004	0.151 ± 0.004

Table 5.2: *Signal efficiencies for the process $H \to WW^{(*)} \to \mu^+\nu_\mu\mu^-\bar{\nu}_\mu$ for different Higgs masses m_H derived from Monte Carlo. The quoted errors are statistical errors only.*

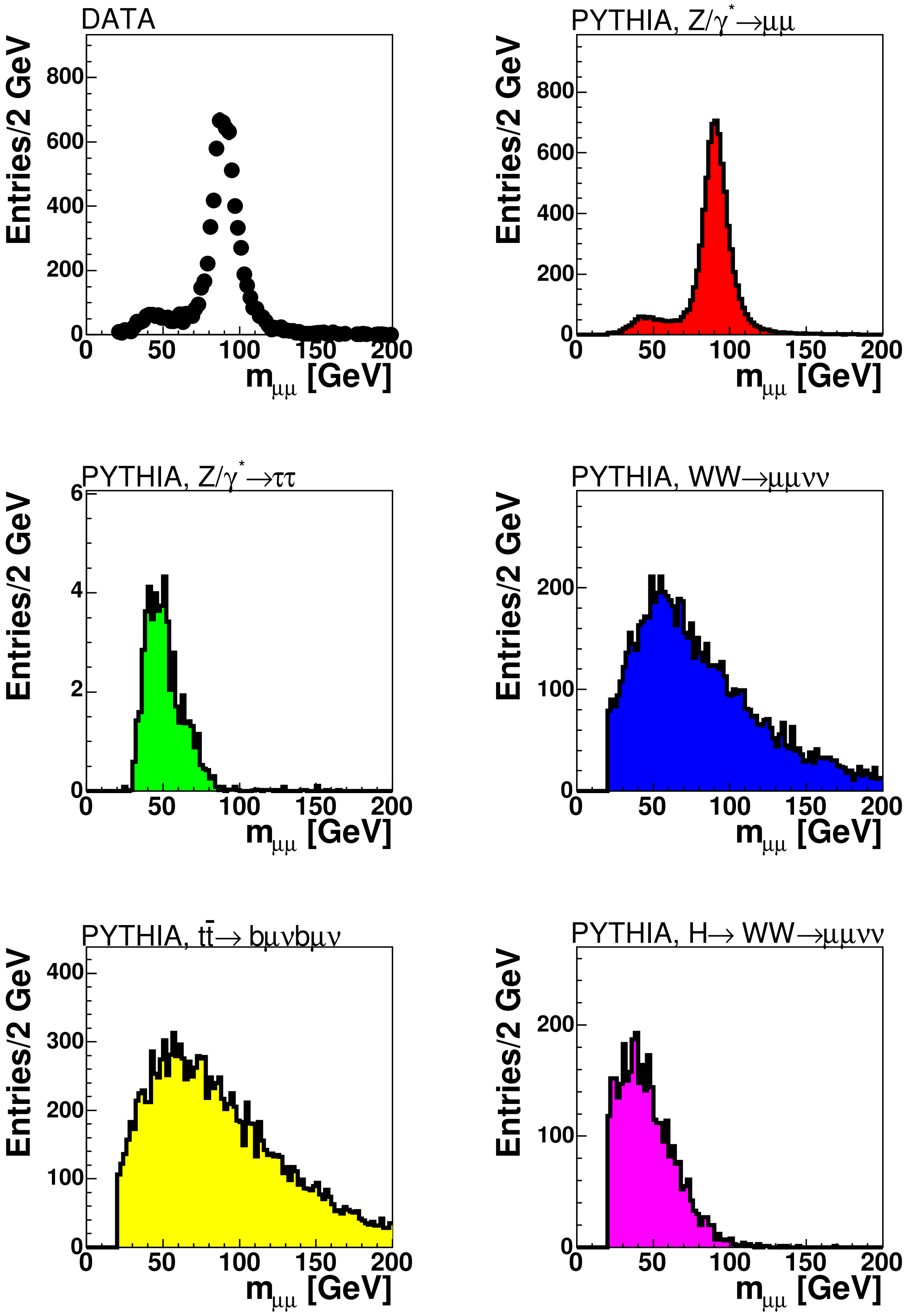

Figure 5.2: *Distribution of the invariant mass $m_{\mu\mu}$ for for the different processes. The distributions are shown after the initial preselection cuts on the muon quality and transverse momenta. For better visibility the plots have arbitrary normalisation.*

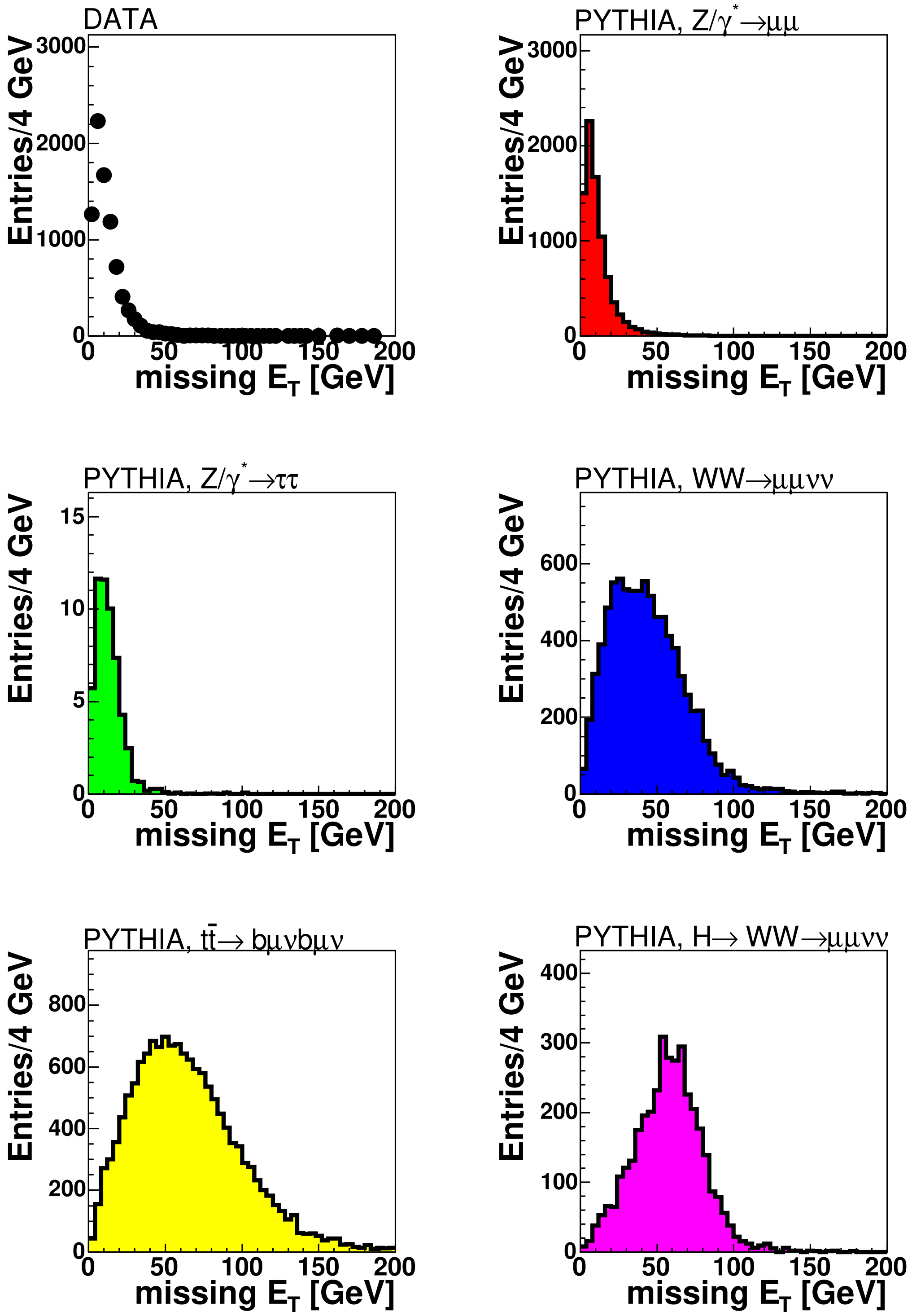

Figure 5.3: *Distribution of the missing transverse energy $\not{E}_{\mathrm{T}}$ for the different processes. The distributions are shown after the initial preselection cuts on the muon quality and transverse momenta. For better visibility the plots have arbitrary normalisation.*

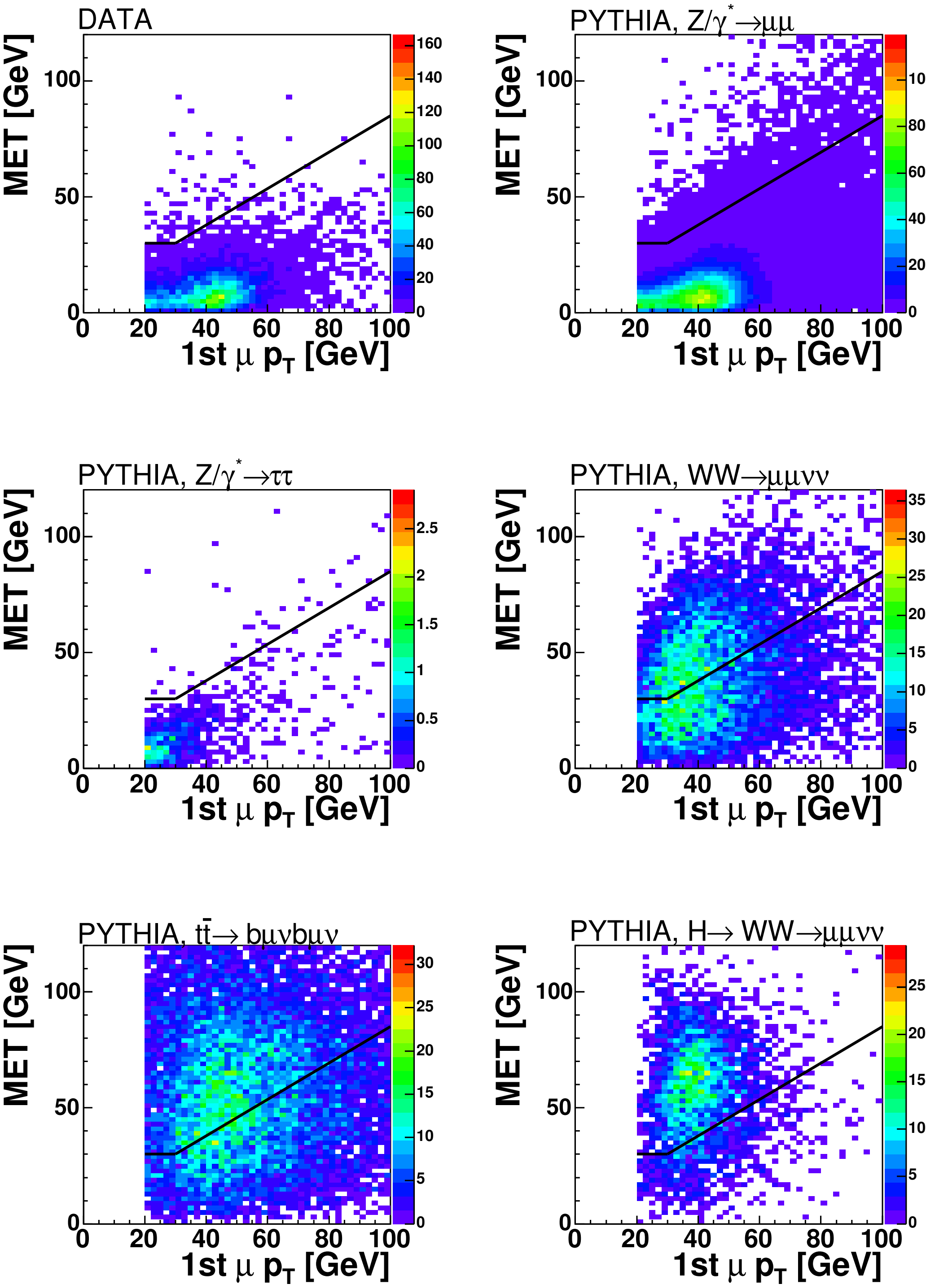

Figure 5.4: *Distribution of the highest muon transverse momentum* $p_{\mathrm{T}}^{\mu 1}$ *and the missing transverse energy* $\not{E}_{\mathrm{T}}$. *Events above the black line are retained. The distributions are shown after the initial preselection cuts on the muon quality and transverse momenta. For better visibility the plots have arbitrary normalisation.*

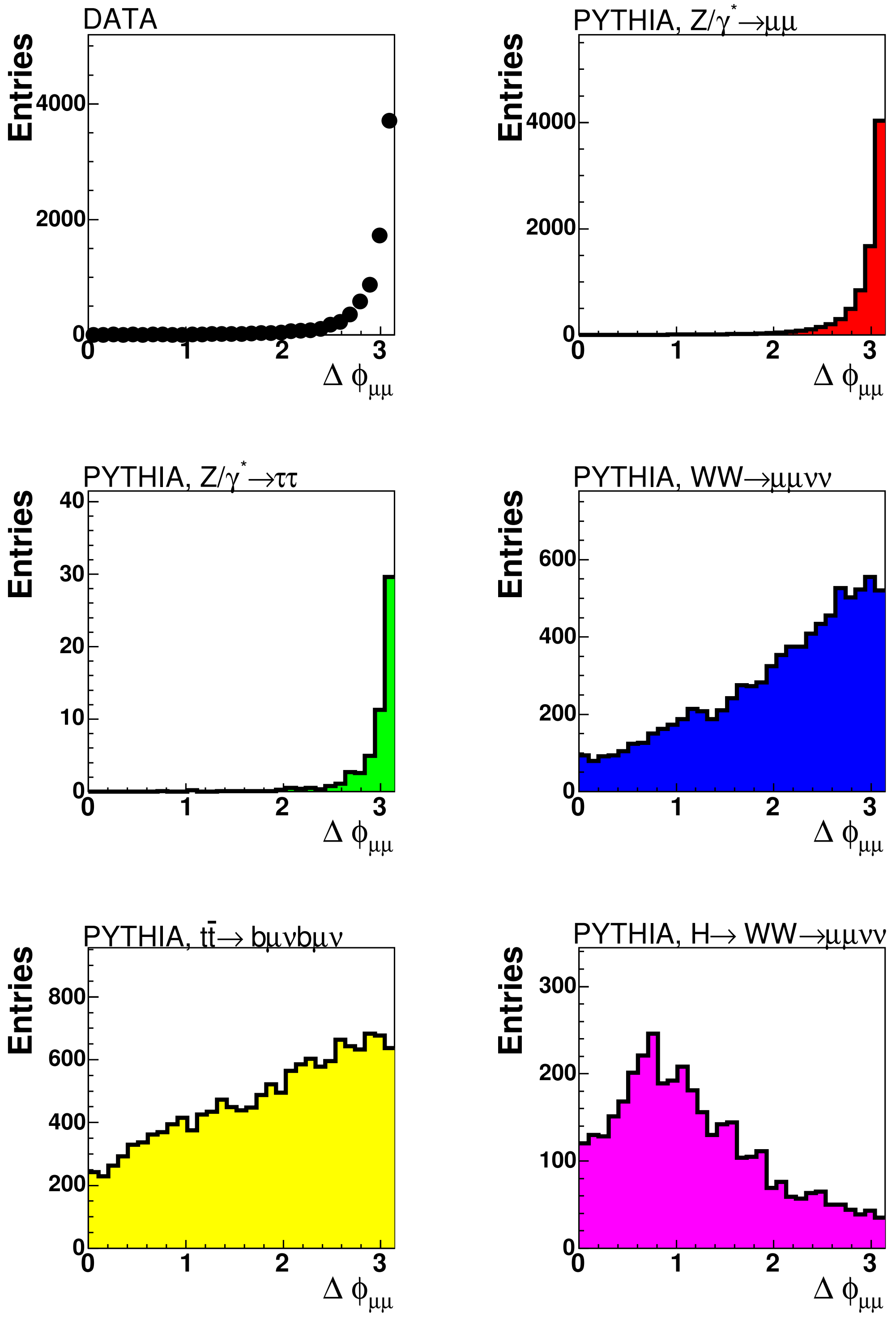

Figure 5.5: *Distribution of the azimuthal opening angle* $\Delta\phi_{\mu\mu}$ *between the two muons for the different channels. The distributions are shown after the initial preselection cuts on the muon quality and transverse momenta. For better visibility the plots have arbitrary normalisation.*

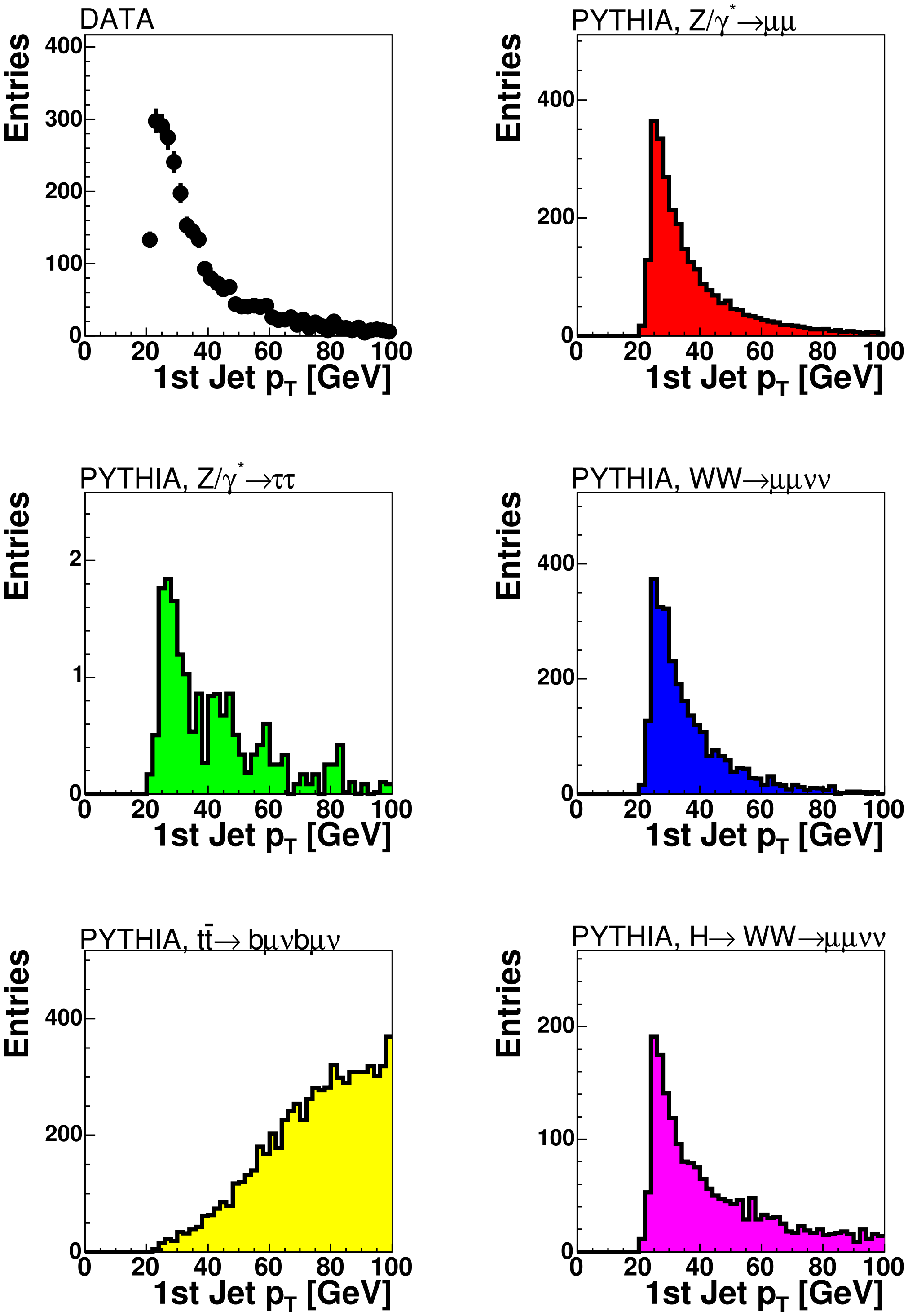

Figure 5.6: *Distribution of the leading jet transverse momentum* p_T^{Jet} *for the different channels. The distributions are shown after the initial preselection cuts on the muon quality and transverse momenta. For better visibility the plots have arbitrary normalisation.*

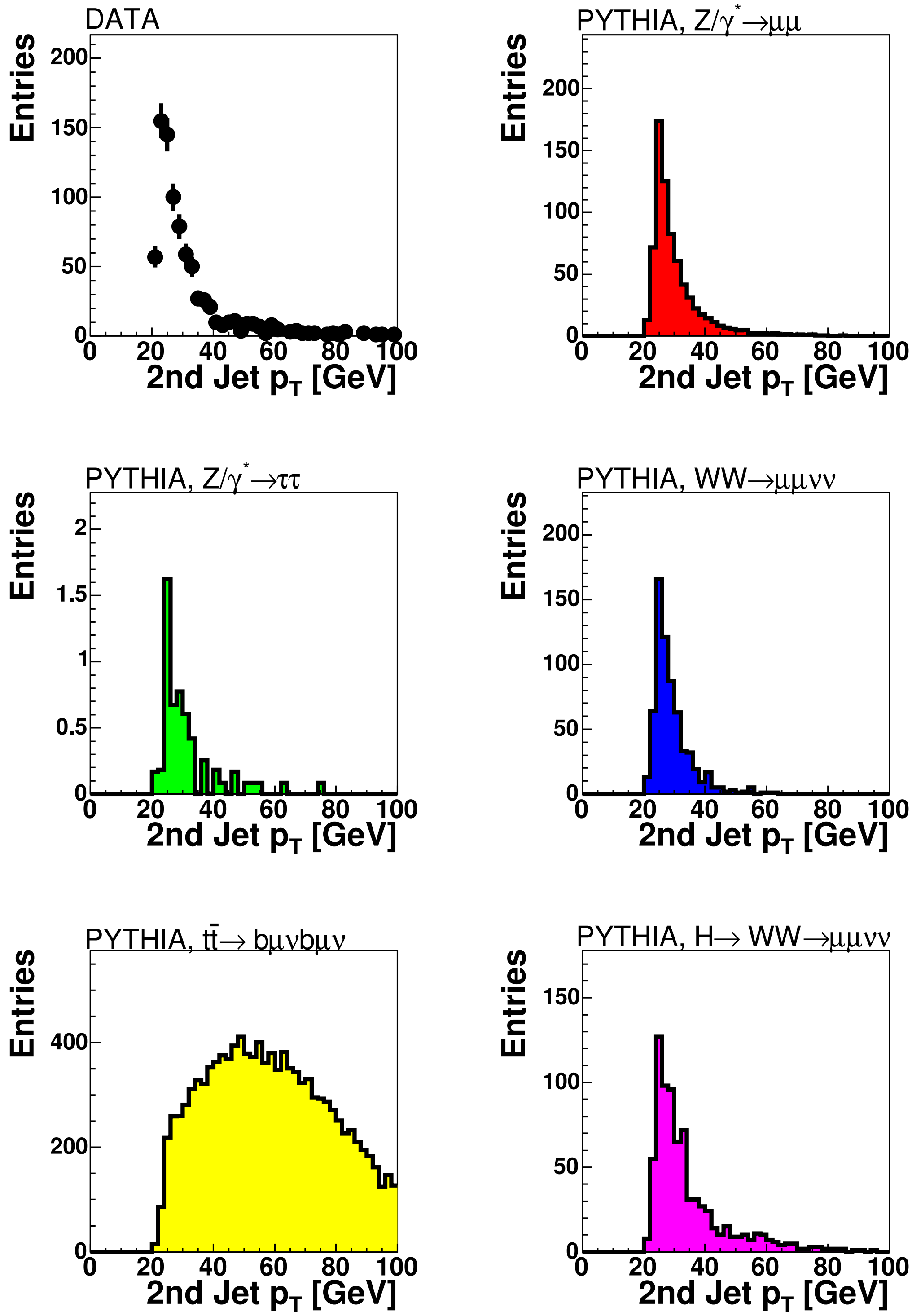

Figure 5.7: *Distribution of trailing jet transverse momentum* p_T^{Jet} *for the different channels. The distributions are shown after the initial preselection cuts on the muon quality and transverse momenta. For better visibility the plots have arbitrary normalisation.*

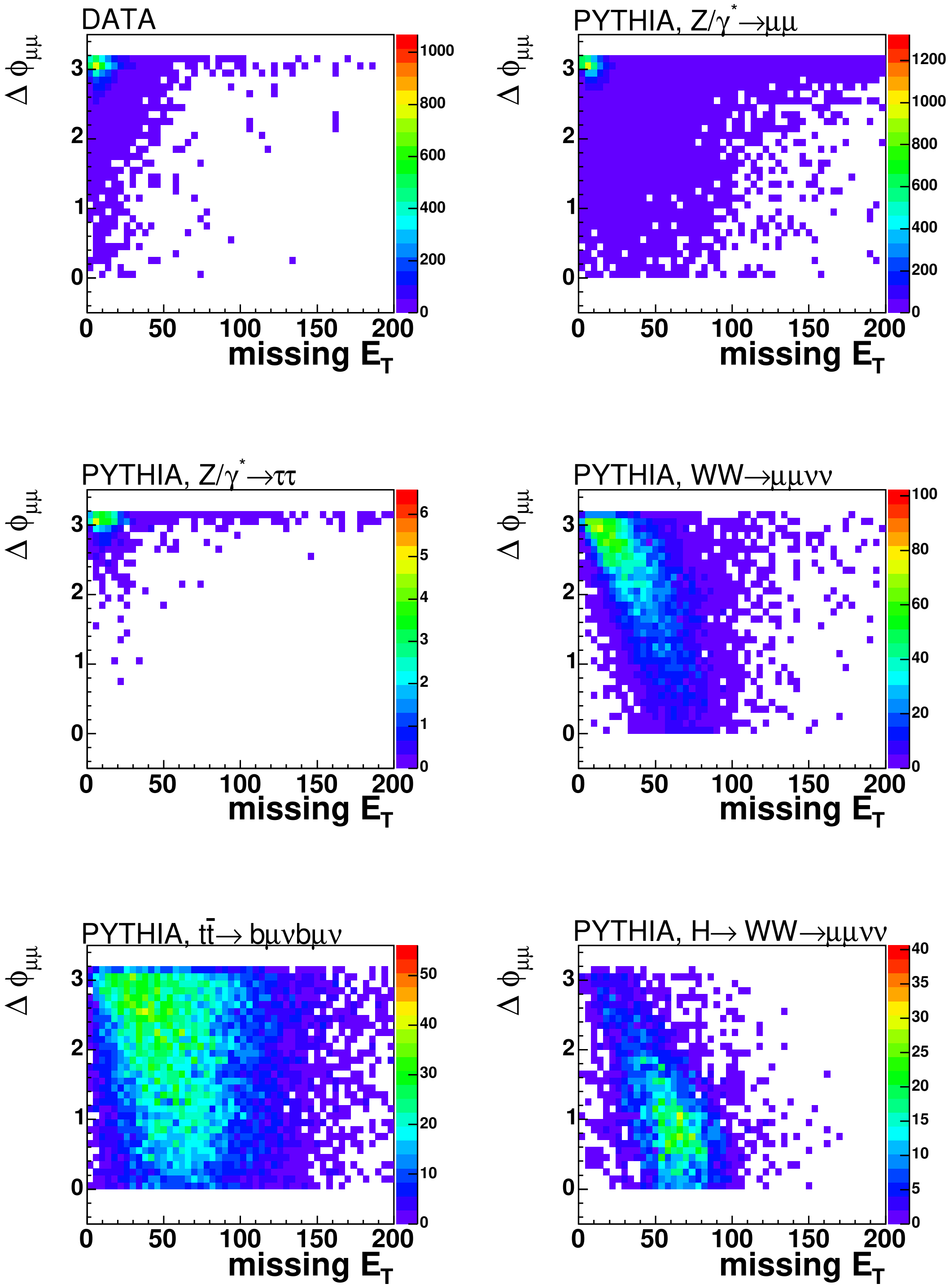

Figure 5.8: *Distribution of missing transverse energy $\not{E}_T$ versus the azimuthal opening angle $\Delta\phi_{\mu\mu}$ of the two muons for the different channels. The distributions are shown after the initial preselection cuts on the muon quality and transverse momenta. For better visibility the plots have arbitrary normalisation.*

5.2 $b\bar{b}$ and W+jets Background

The contribution from $b\bar{b}$ and W+jets background is determined by a combination of data and Monte Carlo simulation. A sample of $b\bar{b}$ events was generated using PYTHIA. EvtGen [42] and `d0_mess` [43] were used for proper decay description and statistical enhancement. EvtGen is an event generator designed for the simulation of the physics of B decays. It is especially useful in complex sequential decays such as semi-leptonic decays and CP violating decays. EvtGen is also used in both the CLEO and BaBar collaborations, which have an extensive b quark research programme. D0_mess is one programme in the DØ MC generation chain. It is used to select certain rare decay processes directly on generator level from a large of sample of generated events. This saves a large amount of computing time and resources since only potentially interesting events have to be passed through the whole detector simulation and reconstruction chain (see Section 2.5). Both programs were also used for a sample of W+$b\bar{b}$ events generated using the Monte Carlo generator ONETOP [44] and PYTHIA.

The contribution from $b\bar{b}$ events is estimated in data from like-sign di-muon events with an inverted isolation criterion. One muon has to fail the isolation cuts, i.e. track isolation: $\sum_{\mathrm{tracks}}^{\mathrm{R}<0.5} p_T > 4.0\,\mathrm{GeV}$. By inverting the muon isolation criterion in the like-sign case an enriched sample of $b\bar{b}$ and W+jets events with almost no $Z/\gamma^* \to \mu^+\mu^-$ contribution is selected. The cross-section given by the Monte Carlo simulation is not used since the uncertainty is too large for a proper normalisation of the $b\bar{b}$ contribution. An overall normalisation derived from data is used instead. Figure 5.9 shows the distributions of the di-muon invariant mass, the muon transverse momentum p_T, the di-muon opening angle $\Delta\phi_{\mu\mu}$ and the missing transverse energy in the like-sign di-muon sample. This background is characterised by low muon p_T, large opening angle and a modest missing transverse energy. The ratio between like-sign and non like-sign $b\bar{b}$ events is obtained from MC to be ≈ 0.344 for muons with transverse momentum $p_T > 15\,\mathrm{GeV}$. The number of $b\bar{b}$ events is given by the number of non like-sign events in MC ($N_{\mathrm{all}}^{\mathrm{MC,ULS}}$) times the isolation efficiency $\varepsilon_{\mathrm{iso,b\bar{b}}}$ squared and normalised to the data by the ratio of inverted isolated like-sign events $N_{\mathrm{inviso}}^{\mathrm{LS}}$ in data and MC:

$$N_{\mathrm{b\bar{b}}} = \varepsilon_{\mathrm{iso,b\bar{b}}}^2 \cdot \frac{N_{\mathrm{inviso}}^{\mathrm{DATA,LS}}}{N_{\mathrm{inviso}}^{\mathrm{MC,LS}}} \cdot N_{\mathrm{all}}^{\mathrm{MC,ULS}}. \tag{5.1}$$

The isolation efficiency is determined by the number of isolated muons divided by the number of all muons in the MC sample:

$$\varepsilon_{\mathrm{iso,b\bar{b}}} = \frac{N_{\mathrm{iso,b\bar{b}}}^{\mu}}{N_{\mathrm{all}}^{\mu}} = 0.068 \pm 0.001(stat.) \pm 0.006(sys.). \tag{5.2}$$

The cut on the muon transverse momentum was varied in a range of $\Delta p_T = 3\,\mathrm{GeV}$ since muons with smaller p_T tend to be less isolated. This leads to an systematic error on $\varepsilon_{\mathrm{iso,b\bar{b}}}$

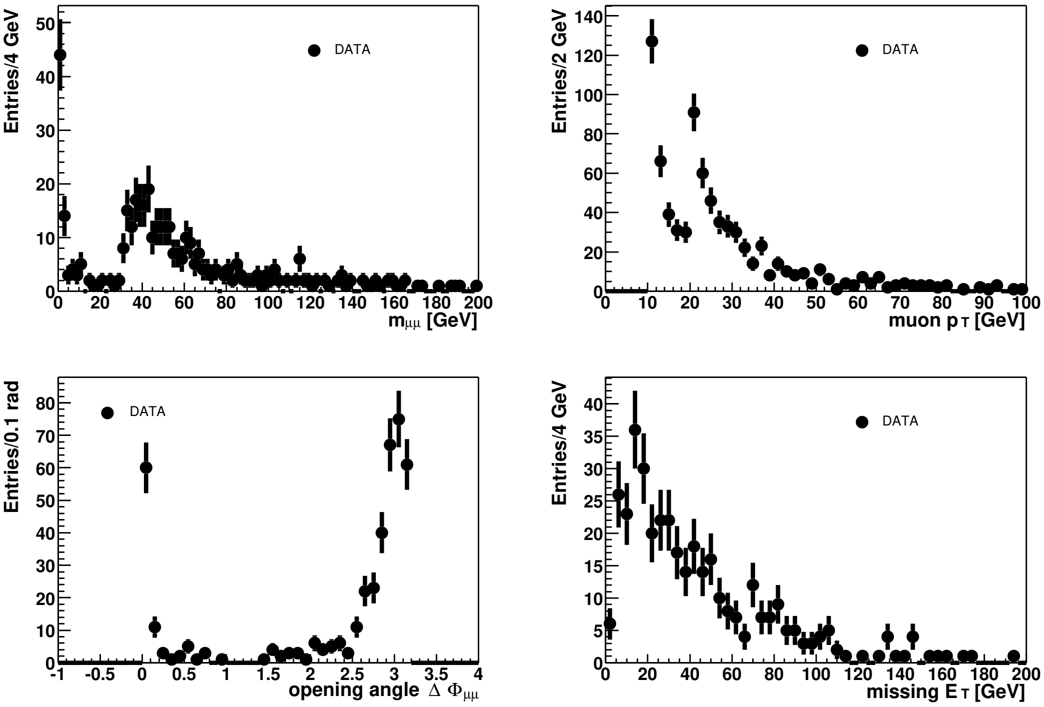

Figure 5.9: *Distributions of the di-muon invariant mass, the muon transverse momentum, di-muon opening angle* $\Delta\phi_{\mu\mu}$ *and the missing transverse energy from* $b\bar{b}$ *and W+jets background enriched sample.*

of about 10%. Table 5.3 shows the contribution of $b\bar{b}$ events after different successive cuts. Already after the preselection the number of $b\bar{b}$ events is very small.

The number of events from W+$b\bar{b}$ production is obtained directly from MC. Table 5.4 shows the number of events after applying successive cuts. The normalisation of the sample is done with a cross-section $\sigma \approx 4.55\,\text{pb}$ calculated with COMPHEP [45]. This cross-section predicted by ONETOP is $\sigma \approx 4.6\,\text{pb}$. The precise value of these cross-section depends on the kinematic cuts made at the generation stage. Due to the large theoretical uncertainties a systematic error of 100% is assigned to this cross-section. After all cuts the contribution from W+$b\bar{b}$ production is approximately the same as from $b\bar{b}$ production.

Table 5.5 shows a systematic check of the W+jet production using APLGEN [46] instead of ONETOP as Monte Carlo generator. Different processes for one- and two-jets production with charm and bottom quarks and inclusive jet production have been simulated. After all cuts only W+$c\bar{c}$ and W+$b\bar{b}$ production show measurable contribution and are in good agreement with the numbers obtained with ONETOP.

cut	$N^{\mathrm{DATA,LS}}_{\mathrm{inviso}}$	$N^{\mathrm{MC,LS}}_{\mathrm{inviso}}$	$N^{\mathrm{MC,ULS}}_{\mathrm{all}}$	$N_{\mathrm{b\bar{b}}}$
μ-ID/ p_{T}	380	3074	9357	5.4 ± 0.6
$\not\!\!E_{\mathrm{T}}$ & $\not\!\!E_{\mathrm{T}}$ vs. $p_{\mathrm{T}}^{\mu 1}$	84	74	209	1.1 ± 0.2
$m_{\mu\mu}$	74	67	193	1.0 ± 0.2
$\Delta\phi_{\mu\mu}$	11	45	141	0.16 ± 0.06
Jet p_{T}	3	4	5	0.02 ± 0.02

Table 5.3: *$b\bar{b}$ contribution estimated from like-sign di-muon events in data.*

cut	$N_{\mathrm{W+b\bar{b}}}$
μ-ID/ p_{T}	0.035 ± 0.035
$\not\!\!E_{\mathrm{T}}$ & $\not\!\!E_{\mathrm{T}}$ vs. $p_{\mathrm{T}}^{\mu 1}$	0.02 ± 0.02
$m_{\mu\mu}$	0.01 ± 0.01
$\Delta\phi_{\mu\mu}$	0.01 ± 0.01
Jet p_{T}	0.01 ± 0.01

Table 5.4: *Number of events from W+$b\bar{b}$ production obtained from MC.*

cut	Wj	Wjj	Wc	Wcj	Wcc	Wbb
No. of events	48350	189500	19600	19600	41150	198500
σ [pb]	1970	222.1	63.2	39.75	5.82	1.543
μ-ID/ p_{T}	4.9 ± 2.5	0	1.5 ± 0.7	0.5 ± 0.3	0.07 ± 0.04	0.064 ± 0.007
$\not\!\!E_{\mathrm{T}}$ & $\not\!\!E_{\mathrm{T}}$ vs. $p_{\mathrm{T}}^{\mu 1}$	0	0	0	0	0.03 ± 0.02	0.023 ± 0.005
$m_{\mu\mu}$	0	0	0	0	0.03 ± 0.02	0.022 ± 0.005
$\Delta\phi_{\mu\mu}$	0	0	0	0	0.02 ± 0.02	0.018 ± 0.004
Jet p_{T}	0	0	0	0	0.02 ± 0.02	0.011 ± 0.003

Table 5.5: *Number of events from W+jets production obtained from ALPGEN+PYTHIA MC. The "j" denote inclusive jet production of light flavours (u,d,s quarks) and gluons, whereas "b" or "c" denotes jets from b or c-quarks (or their antiquarks).*

5.3 Events with Di-muons and Missing Transverse Energy

Table 5.6 shows the comparison between data and expected background events and the expected number of $H \to WW^{(*)} \to \mu^+\nu_\mu\mu^-\bar{\nu}_\mu$ after the successive application of all cuts. The first column denotes the events after the preselection cuts. Most of the efficiencies discussed in Chapter 4 have been determined with a subsample of these events. There is reasonable agreement between data and Monte Carlo after all successive cuts. The muon momentum resolution from low quality tracks and tracks with high transverse momentum distorts the resolution of the missing transverse energy $\not\!\!E_{\mathrm{T}}$. This is balanced by the first cut requiring the $\not\!\!E_{\mathrm{T}}$ to be dependent on the leading muon transverse momentum.

After applying all cuts 5 events remain in the data whereas 5.3 ± 0.6 events are expected from background Monte Carlo, mainly $Z/\gamma^* \to \mu^+\mu^-$ and $WW \to \mu^+\nu_\mu\mu^-\bar{\nu}_\mu$ production. 0.085 ± 0.001 events are expected from Standard Model $H \to WW^{(*)} \to \mu^+\nu_\mu\mu^-\bar{\nu}_\mu$ decays with a Higgs mass of $m_{\mathrm{H}} = 160\,\mathrm{GeV}$.

	μ-ID/p_{T}	$\not\!\!E_{\mathrm{T}}$ & $\not\!\!E_{\mathrm{T}}$ vs. $p_{\mathrm{T}}^{\mu 1}$	$m_{\mu\mu}$
DATA	8509	98	53
$Z/\gamma^* \to \mu^+\mu^-$	8426 ± 27	97.8 ± 2.8	38.8 ± 1.7
$b\bar{b}$/W+jets	5.4 ± 0.6	1.1 ± 0.2	1.0 ± 0.2
$Z/\gamma^* \to \tau^+\tau^-$	57.7 ± 2.2	0.5 ± 0.2	0.5 ± 0.2
$WW \to \mu^+\nu_\mu\mu^-\bar{\nu}_\mu$	4.64 ± 0.05	1.98 ± 0.03	1.65 ± 0.03
$t\bar{t} \to b\mu\nu b\mu\nu$	3.15 ± 0.03	1.72 ± 0.02	1.34 ± 0.02
MC SUM	8497 ± 27	103.1 ± 2.8	43.3 ± 1.7

	$\Delta\phi_{\mu\mu}$	Jet p_{T}
DATA	10	5
$Z/\gamma^* \to \mu^+\mu^-$	12.8 ± 1.0	3.9 ± 0.6
$b\bar{b}$/W+jets	0.2 ± 0.1	0.02 ± 0.02
$Z/\gamma^* \to \tau^+\tau^-$	0.1 ± 0.1	0 ± 0
$WW \to \mu^+\nu_\mu\mu^-\bar{\nu}_\mu$	1.33 ± 0.03	1.28 ± 0.03
$t\bar{t} \to b\mu\nu b\mu\nu$	0.88 ± 0.01	0.03 ± 0.003
MC SUM	15.3 ± 1.4	5.3 ± 0.6

Table 5.6: *Cut flow table. The quoted errors are statistical only.*

Since the spins from the two decaying Ws originating from the Higgs decay are correlated, the opening angle between the two muons tends to be smaller as compared to events from background sources. The distribution of the opening angle $\Delta\phi_{\mu\mu}$ in the transverse plane is a reasonable discriminant between events from Higgs decays and background contribution. Figure 5.10 shows the opening angle $\Delta\phi_{\mu\mu}$between the two muon tracks for successive cuts.

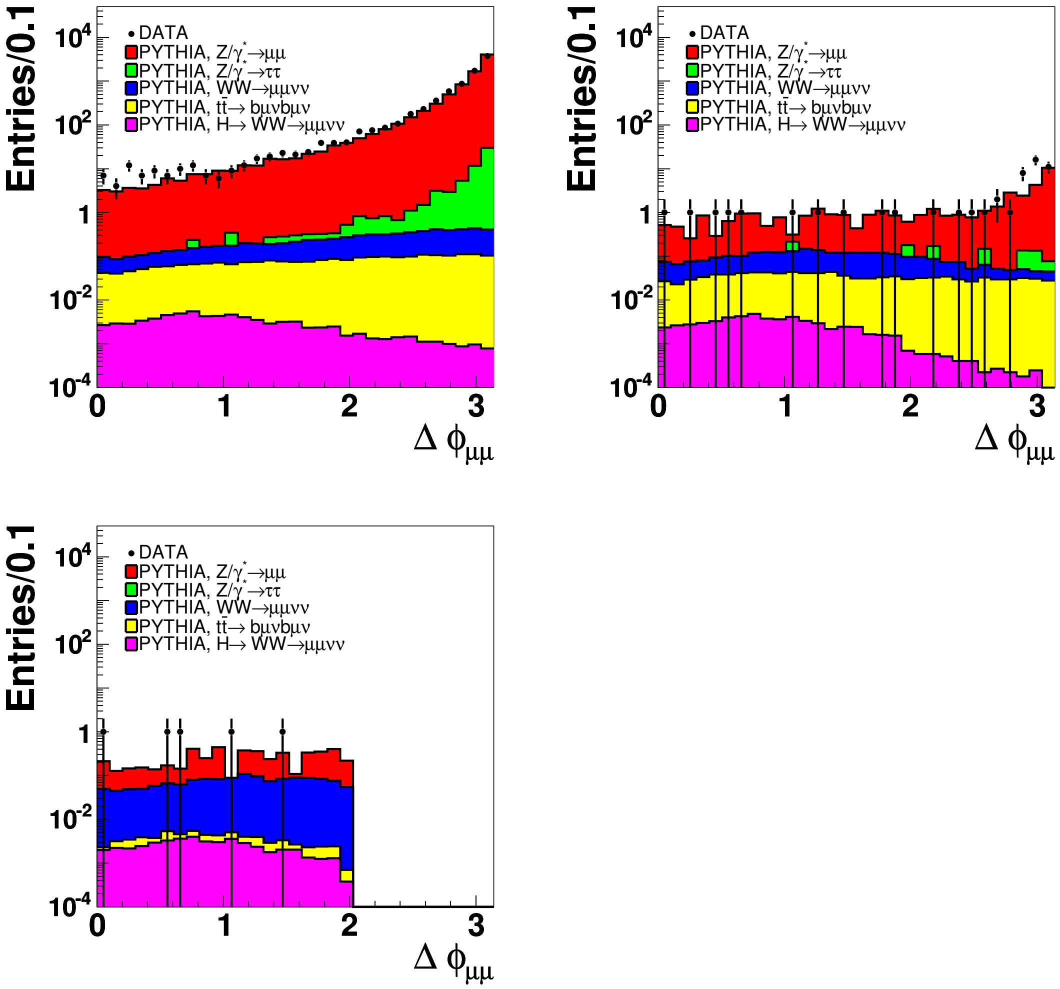

Figure 5.10: *Azimuthal opening angle* $\Delta\phi_{\mu\mu}$ *between the two muon tracks after the different cuts: initial preselection (top), after invariant mass cut (middle), after all cuts. (bottom).*

5.4 Systematic Uncertainties

Systematic uncertainties on the number of selected events have been investigated: the uncertainty on the jet energy scale correction, the muon momentum resolution, the cross-section variation of the main background processes and the luminosity uncertainty. The uncertainty on the luminosity of ±6.5% [26] is part of the limit calculation procedure in the next Section and will be treated separately.

The standard procedure to estimate the error of jet energy scale correction (JES) is the variation of the correction in a $\pm 1\sigma$ error range. Since in this analysis most events have relatively few jets (see Figure 6.2) and most of the jets have small transverse momenta p_{T}, this would lead to an overestimation of the systematic error. In addition only the error on the fraction $JES_{\mathrm{DATA}}/JES_{\mathrm{MC}}$ is needed, which is smaller than the separate errors. The correction was varied instead as follows: the missing transverse energy $\not{E}_{\mathrm{T}}$ was recalculated by adding (subtracting) 25% of every jet transverse momentum. This is a conservative estimation of the errors given in Figure 4.3 since most of the selected jets have a transverse momentum $p_{\mathrm{T}} < 50\,\mathrm{GeV}$. This systematic variation changes the sum of the background events by $+11.2\%$ and -1.9% respectively, while the number of data events stays unchanged. The signal efficiency only slightly changes by -1.7% and $+0.9\%$, respectively.

The muon transverse momentum smearing was changed in MC. In Chapter 4 the influence of the muon transverse momentum resolution on the width of the Z resonance and the quality of the missing transverse energy $\not{E}_{\mathrm{T}}$ distribution was discussed in detail. The smearing factor of $f = 0.00205$ was changed by ±50%. This value is a conservative assumption on the change of the muon transverse momentum resolution, since the width of the Z peak visibly changes under these variations by approximately $0.5\,\mathrm{GeV}$. These variations changes the number of background events by $+6.1\%$ and $+8.1\%$, respectively. The signal efficiency again only slightly changes by $+1.0\%$ and -1.2%, respectively. Though this systematic variation is done in a large range, the effect on the number of background events or signal efficiency is rather small.

The cross-sections of the main background processes have been varied simultaneously within their theoretical uncertainty: the cross-section of Z/γ^{*} production was changed by ±5.6%, the $WW \to \mu^{+}\nu_{\mu}\mu^{-}\bar{\nu}_{\mu}$ production cross-section was varied by $+6.7\%$ and -7.7% and the cross-section of $t\bar{t}$ production was changed by $+5.9\%$ and -14.7%. These variations yield a change on the sum of all background processes of $+3.7\%$ and -4% respectively.

5.5 Limits on the Cross-Section $H \to WW^{(*)}$ in the Di-muon Channel

The limit calculation was done following the method described in [47]. This method calculates the cross-section limits at 95% C.L. with the integrated luminosity, number of background events, signal acceptance and number of events in data with corresponding errors as inputs. The integrated luminosity for the data sample with the four di-muon triggers is $(146.9 \pm 9.5)\,\mathrm{pb}^{-1}$. The uncertainty on the luminosity is 6.5%. The number of background events and events in data is taken from Table 5.6. The signal efficiency for six different Higgs boson masses is listed in Table 5.2. The uncertainty on the background was determined from the statistical and systematic error added in quadrature.

For this single decay channel the upper limits on the cross-section are calculated by determining a Bayesian likelihood function L as a function of the signal cross-section which directly depends on the Higgs boson mass m_{H}. The likelihood function L is interpreted as a probability density of observing N events for a signal cross-section σ under a combined signal+background hypothesis. The upper limit on the cross-section σ_{95} at 95% C.L. is given by:

$$0.95 = \int_0^{\sigma_{95}} L d\sigma \cdot \left(\int_0^{\infty} L d\sigma \right)^{-1} . \tag{5.3}$$

For a detailed discussion of the Bayesian limit calculation see [47] and appendix B in [27].

Table 5.7 summarises the upper limits on the cross-section times branching ratio $\sigma \times BR(H \to WW)$ for $H \to WW^{(*)} \to \mu^+\nu_\mu\mu^-\bar{\nu}_\mu$ decays for six different Higgs masses m_{H} with $BR(W \to \mu\nu) = 0.1057 \pm 0.0022$ [18]. Figure 5.11 shows the calculated cross-section limits on $\sigma \times BR(H \to WW)$ from the analysis of the di-muon channel assuming the above value of the branching ratio $BR(W \to \mu\nu)$ for the different Higgs masses together with expectations from Standard Model Higgs boson production and alternative models. The LEP limit on the Standard Model Higgs boson production is taken from [1], the 4th generation model is presented in [17], and the topcolor model is presented in [8]. It can be seen that no mass region of a Standard Model Higgs boson or alternative model can be excluded with this single decay channel and the current integrated luminosity. With the expected full data set in the year 2009 and the approximately 50 time larger amount of integrated luminosity a 4th generation and topcolor model can be excluded or discovered. It is expected that the presented analysis easily scales with the yet to be taken data until the end of Tevatron data taking. An exclusion or discovery of a Standard Model Higgs boson in certain mass region needs a combination with other decay channels, which is presented in the next section.

$m_{\mathrm{H}}\,[\mathrm{GeV}]$	100	120	140	160	180	200
upper limit on $\sigma \times BR\,[\mathrm{pb}]$	82.7	33.7	24.7	17.1	20.7	24.5

Table 5.7: *Upper limits at 95% CL on the cross-section times branching ratio* $\sigma \times BR(H \to WW)$ *for different Higgs masses* m_{H}.

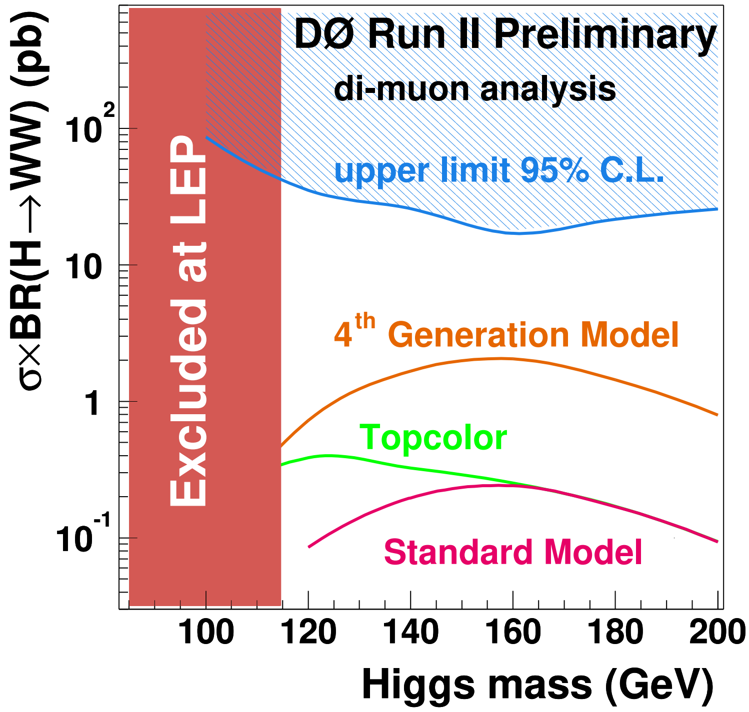

Figure 5.11: *cross-section limit curve* $\sigma \times BR(H \to WW)$ *for the process* $H \to WW^{(*)} \to \mu^+\nu_\mu\mu^-\bar{\nu}_\mu$ *together with expectations from Standard Model Higgs boson production and alternative models. The LEP limit on the Standard Model Higgs boson production is taken from [1], the 4th generation model is presented in [17], and the topcolor model is presented in [8].*

5.6 Combination of Limits on the Cross-Section $H \to WW^{(*)}$

As described in the previous section, the limit on the $H \to WW^{(*)}$ production can be improved by combining the limits from the di-muon channel with other decay channels of the Ws. This is done with the di-electron and electron-muon decay channels of the two W bosons [48]. Decay channels with tau leptons are not considered, since tau decays are much more difficult to detect and discriminate from background processes than the first two generation leptons.

If the two or more independent data sets for a combination have the same production cross-section, a combined limit can be calculated by multiplying the two likelihood functions to a combined likelihood $L = L_1 \cdot L_2$, before applying equation 5.3. A combination of all three channels has been performed by multiplying the individual likelihood functions of all three channels resulting into a combined likelihood function. The different experimentally measured values of the branching ratios for the electron and muon decays of the Ws and the double rate of the electron-muon decay channel have been taken into account. The calculation is done separately for all six different masses. The cross-channel correlation given by the luminosity uncertainty and common object ID's in the different channels is determined to be small.

Table 5.8 sums up the individual upper limits on the cross section times branching ratio for the three different decay channels and their combination for six different Higgs boson masses m_{H}. The integrated luminosities for the three different channels are $\mathcal{L} \approx 177\,\mathrm{pb}^{-1}$ for the ee channel, $\mathcal{L} \approx 158\,\mathrm{pb}^{-1}$ for the $e\mu$ channel, and $\mathcal{L} \approx 147\,\mathrm{pb}^{-1}$ for the $\mu\mu$ channel. The differences are due to different quality criteria that are required for the different channels. For the di-muon channel all parts of the DØ sub-detectors should have good quality assignments, whereas for the di-electron channel the muon detector is less relevant. The different values of the upper limits for the three different channels especially for the two lowest mass points are a consequence of the different background contributions. The ee and $\mu\mu$ channels have about the same sensitivity. The differences between both channels are due to the different integrated luminosity in both channels. The $e\mu$ channel has more sensitivity compared to the other two channels because of the double branching ratio and the absence of di-lepton resonances like the Z boson and Υ.

The combination of all channels yields approximately three times better limits than for the single di-muon channel presented in the previous sections. The combination of the three channels is without any efficiency losses equivalent to a four times larger integrated luminosity in a single channel. The difference between the theoretical gain of a factor of four and the actual gain of about a factor of three is due to the different integrated luminosities and selection efficiencies in the three channels. With the full Run II dataset certain mass regions of the Standard Model Higgs boson can be excluded at 95 % C.L. in the combination of all three channels. Figure 5.12 shows the calculated cross-section limits for $\sigma \times BR(H \to WW^{(*)})$ for the different Higgs boson masses compared with predictions from the Standard Model and alternative models. No alternative models or a Standard Model Higgs boson mass region can be excluded yet.

m_{h} [GeV]	100	120	140	160	180	200
ee: limit $\sigma \times BR(H \to WW)$ [pb]	102.2	29.7	21.8	14.8	15.2	19.2
$e\mu$: limit $\sigma \times BR(H \to WW)$ [pb]	90.0	21.0	13.1	9.6	9.2	9.6
$\mu\mu$: limit $\sigma \times BR(H \to WW)$ [pb]	86.4	35.2	25.8	17.9	21.6	25.7
all: limit $\sigma \times BR(H \to WW)$ [pb]	40.1	12.0	8.2	5.7	5.8	6.6

Table 5.8: *Upper limits on the cross-section times branching ratio for* $\sigma \times BR(H \to WW)$ *from the ee, eμ, μμ final state and the combination of all three channels for different Higgs boson masses* m_{H}.

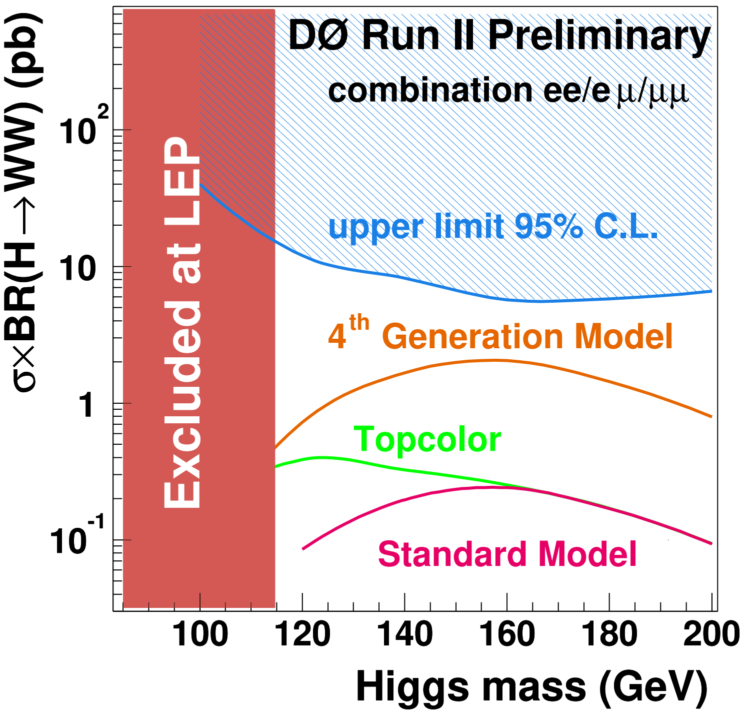

Figure 5.12: Excluded cross-section times branching ratio $\sigma \times BR(H \to WW^{(*)})$ at 95% C.L. together with expectations from Standard Model Higgs boson production and alternative models. The LEP limit on the Standard Model Higgs boson production is taken from [1], the 4th generation model is presented in [17], and the topcolor model is discussed in [8].

6 Measurement of the *WW* Cross-Section

In Chapter 5 limits on the $H \to WW^{(*)}$ production have been presented in detail in the di-muon channel and in combination with the di-electron and electron-muon channel. It was shown that the dominant irreducible backgrounds after all cuts are $Z/\gamma^* \to \mu^+\mu^-$ and $WW \to \mu^+\nu_\mu\mu^-\bar{\nu}_\mu$ production. It is very important to measure these background with good accuracy to improve the limits on $H \to WW^{(*)}$ production. In the following Chapter limits on the WW cross-section in the di-muon channel and a first measurement of the WW cross-section at DØ in the combination of all three channel are presented.

6.1 Event Selection and Limit in the Di-muon Channel

The event selection for WW cross-section measurement in the di-muon channel is similar to the selection criteria discussed in Section 5.1. The kinematic properties of WW production are comparable with them from $H \to WW^{(*)}$ production, though there are slight differences like e.g. in the azimuthal opening angle $\Delta\phi_{\mu\mu}$. To further enhance the signal to background ratio especially with respect to the remaining $Z/\gamma^* \to \mu^+\mu^-$ background a few cuts are slightly changed. The few differences are discussed in the following. The muons are restricted to the pseudo-rapidity range of $|\eta| < 1.8$. Since WW production is more central than the main background from $Z/\gamma^* \to \mu^+\mu^-$ decays, no significant signal inefficiency is expected. Figure 6.1 shows the distributions of η versus ϕ for the different MC contributions and data. Furthermore this cut assures a homogeneous tracking efficiency since tracks in the regions $|\eta| > 1.8$ tend to have less track quality which distorts the $\not{E}_T$ distribution (see Section 4.4.2). The cut on the invariant mass $m_{\mu\mu}$ is tightened on the region below the Z resonance with the requirement $20\,\mathrm{GeV/c^2} < m_{\mu\mu} < 75\,\mathrm{GeV/c^2}$. This cut reduces background from mismeasured $Z/\gamma^* \to \mu^+\mu^-$ events from the Z-peak. The cut on the opening angle between the two muons is relaxed from $\Delta\phi_{\mu\mu} < 2.0$ to $\Delta\phi_{\mu\mu} < 2.4$. To reject the dominant contribution from $Z/\gamma^* \to \mu^+\mu^-$ decays, a tighter cut on the missing transverse energy is applied. Requiring $\not{E}_T > 40$ GeV removes most of the $Z/\gamma^* \to \mu^+\mu^-$ decays without decreasing the signal efficiency significantly. The

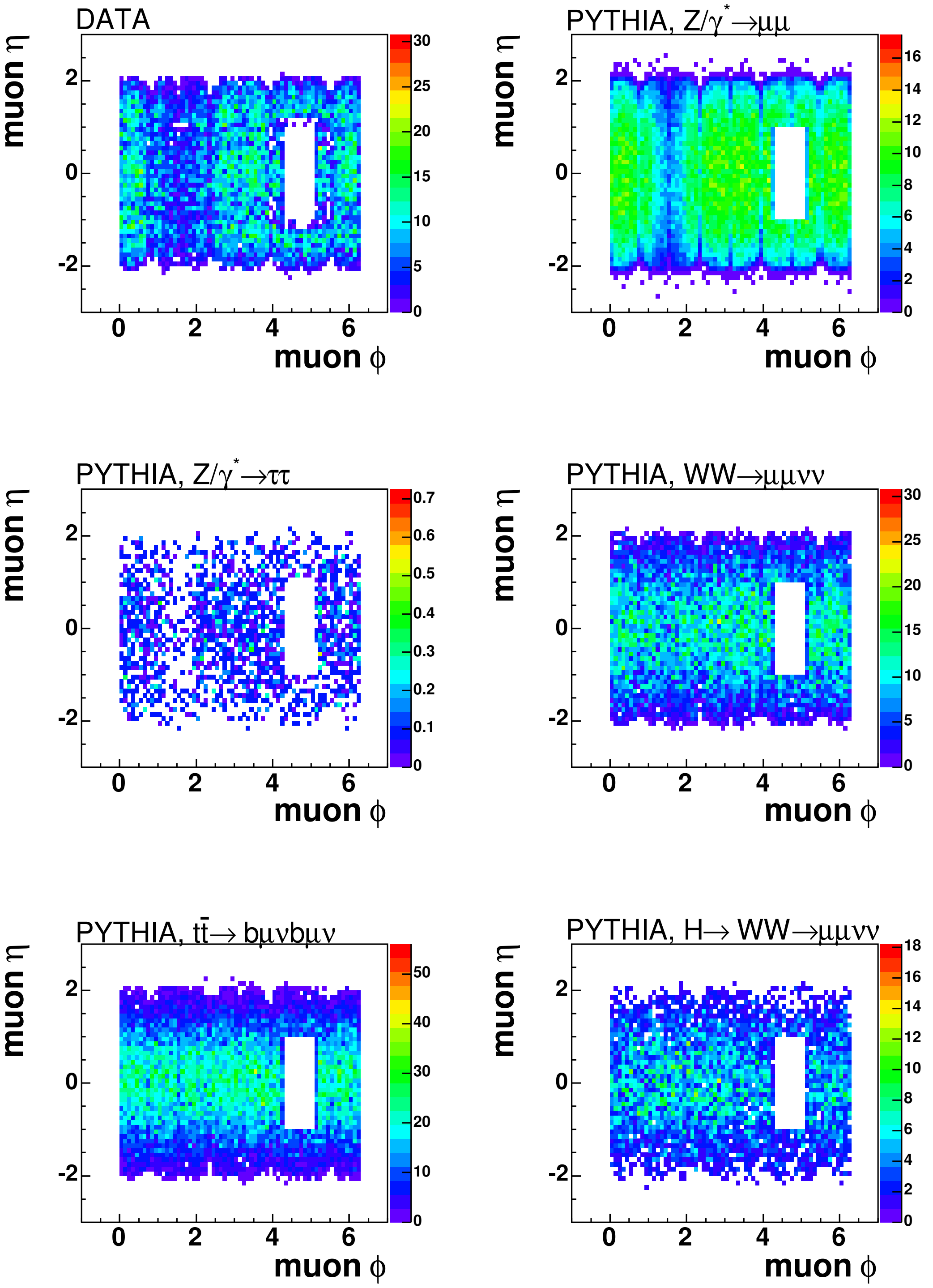

Figure 6.1: *Distribution of the muon* η *versus* φ. *The hole in the data acceptance for* $4.25 < \phi < 5.25$ *and* $\eta < 1$ *is due to the missing muon scintillation detector coverage in the bottom part of the detector and therefor the missing level 1 trigger acceptance in the region. For consistency reasons this region was excluded in MC. It can be seen that WW production happens more central than e.g.* $Z/\gamma^* \to \mu^+\mu^-$ *production. For better visibility the plots have arbitrary normalisation.*

remaining $t\bar{t}$ and multi-jet events are rejected by a cut on the leading jet p_{T} requiring $p_{\mathrm{T}}^{\mathrm{Jet1}} < 60\,\mathrm{GeV/c}$. The cut on the trailing jet p_{T} is dropped since WW production is expected to have less jets in the events. Figure 6.2 and 6.3 shows the jet multiplicity of the different MC contributions and data. It can be seen that WW has mainly zero or only jet jet in the events. The disagreement between data and MC for high jet multiplicities is expected since PYTHIA is a leading order Monte Carlo generator. This disagreement is negligible for this analysis though, since only events with low jet multiplicity are selected.

Table 6.1 summarises all cuts for the measurement of the WW production. The kinematic and quality cuts are identical to the cuts discussed in Section 5.1. After this final selection, three events remain in the data.

Cut name	Cut range
Acceptance	$\eta_{\mu} < 1.8$
Di-Muon mass	$20\,\mathrm{GeV} < m_{\mu\mu} < 75\,\mathrm{GeV}$
Missing transverse energy $\not{E}_{\mathrm{T}}$	$\not{E}_{\mathrm{T}} > 40\,\mathrm{GeV}$
Mismeasured $\not{E}_{\mathrm{T}}$:	$\not{E}_{\mathrm{T}} > 0.75 \cdot p_{\mathrm{T}}^{\mu 1} + 10\,\mathrm{GeV}$
Muon opening angle:	$\Delta\phi_{\mu\mu} < 2.4$
Jet p_{T} ($\lvert\eta^{\mathrm{Jet}}\rvert < 2.5$)	$p_{\mathrm{T}}^{\mathrm{Jet1}} < 60\,\mathrm{GeV}$

Table 6.1: *Summary of signal selection cuts for* $WW \to \mu^{+}\nu_{\mu}\mu^{-}\bar{\nu}_{\mu}$ *production.*

For the $\mu^{+}\mu^{-}$ channel, the efficiency for $WW \to \mu^{+}\nu_{\mu}\mu^{-}\bar{\nu}_{\mu}$ production at the beginning of the selection is (33.1±0.2)%. Applying all the different selection criteria reduces the efficiency to (7.4±0.2)%. The expected number of WW events is 1.62±0.04 assuming the cross-section of 13 pb (c.f. Section 2.3) and an integrated luminosity of $147\,\mathrm{pb}^{-1}$. The expectations from all the backgrounds is 1.28±0.30 events to which $Z/\gamma^{*} \to \mu^{+}\mu^{-}$ decays contribute more than 90%. In Table 6.2 the expected numbers for all backgrounds, the WW signal are compared with the data for all different selection criteria.

With the given numbers the significance of a cross-section measurement is very low in the di-muon channel alone. A limit at 95% C.L. can be calculated for the di-muon channel with the same methods described in Section 5.5. Neglecting systematic uncertainties the limit calculation yields a limit of $\sigma_{WW} < 43.1\,\mathrm{pb}$ at 95% C.L.

6.2 Measurement of the Cross-Section

From the previous Section it can be seen that a measurement of the WWcross-section excluding a zero cross-section is not possible in the di-muon channel alone. The cross-section is estimated separately for all three final states of the di-muon, di-electron and

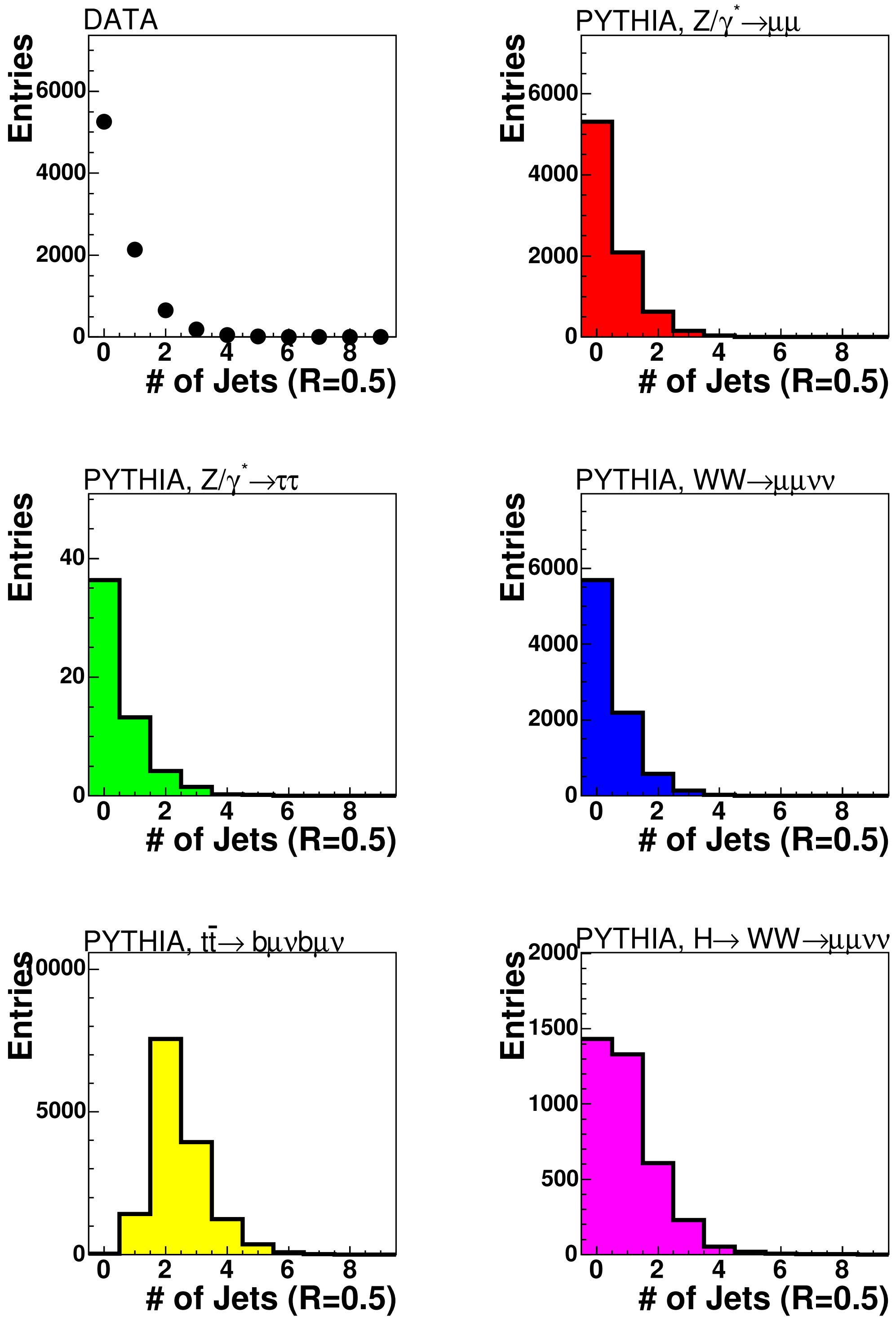

Figure 6.2: *Distribution of the jet multiplicity of the different MC contributions and data. It can be seen that WW production has mainly zero or one jet in the event. For better visibility the plots have arbitrary normalisation.*

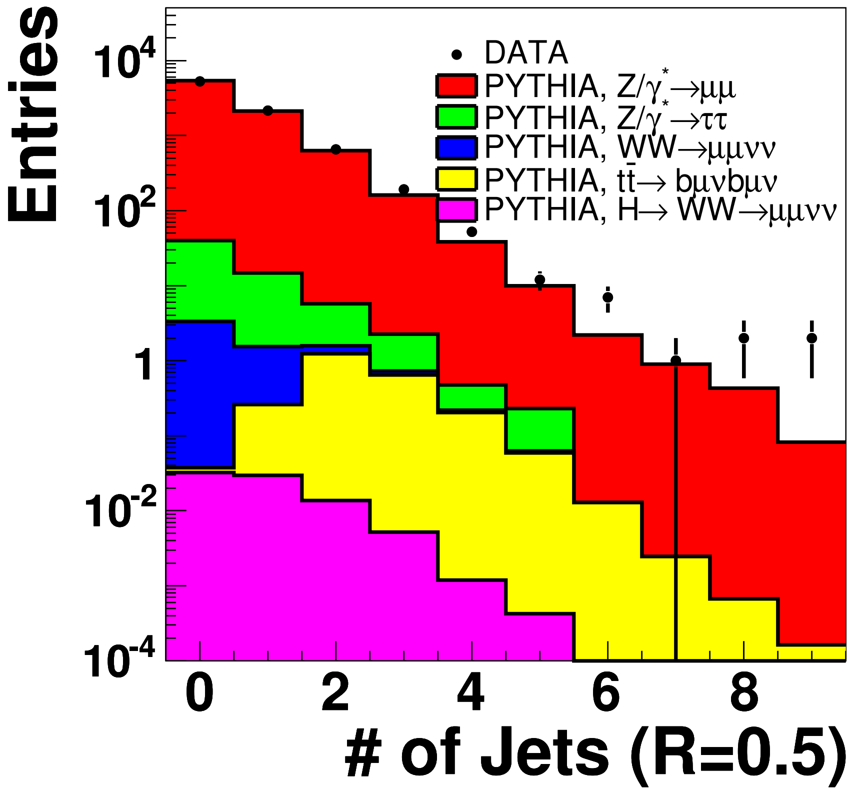

Figure 6.3: *Distribution of the jet multiplicity in data and MC.*

electron-muon channel before combining it. To calculate the cross-section, the likelihood method described in [49] is used. The small number of events are taken into account by using Poisson statistics. The cross-section σ is given by the equation

$$\sigma = \frac{N_{\mathrm{obs}} - N_{\mathrm{bg}}}{\mathcal{L} \cdot BR \cdot \varepsilon}, \tag{6.1}$$

where N_{obs} is the number of observed events, N_{bg} the expected background contribution, $\mathcal{L}$ is the integrated luminosity, BR the branching ratio and ε the efficiency for the signal. The likelihood for the observation of $\tilde{N}$ events with N_{obs} events in the data is given by:

$$L(\sigma, N_{\mathrm{obs}}, N_{\mathrm{bg}}, \mathcal{L}, BR, \varepsilon) = \frac{\tilde{N}^{N_{\mathrm{obs}}}}{N_{\mathrm{obs}}!} e^{-\tilde{N}} \,. \tag{6.2}$$

$\tilde{N}$ is the number of signal and background events:

$$\tilde{N} = \sigma \cdot BR \cdot \mathcal{L} \cdot \varepsilon + N_{\mathrm{bg}} \tag{6.3}$$

	μ-ID/p_{T}	η	$m_{\mu\mu}$
DATA	8509	7496	1149
$WW \to \mu^+\nu_\mu\mu^-\bar{\nu}_\mu$	7.24±0.08	6.79±0.08	3.46±0.05
$Z/\gamma^* \to \mu^+\mu^-$	8426±27	7460±25	1065±10
$b\bar{b}$/W+jet	5.4±0.6	5.0±0.5	4.9±0.5
$Z/\gamma^* \to \tau^+\tau^-$	57.7±2.2	53.2±2.1	50.8±2.1
$t\bar{t}$	3.15±0.03	3.06±0.03	1.36±0.02
MC Sum	8500±27±553	7528±26±489	1125±10±73

	$\Delta\phi$/Jet	$\not{E}_{\mathrm{T}}$ vs. $p_{\mathrm{T}}^{\mu 1}$	$\not{E}_{\mathrm{T}}$
DATA	129	6	3
$WW \to \mu^+\nu_\mu\mu^-\bar{\nu}_\mu$	2.57±0.04	1.88±0.04	1.62±0.04
$Z/\gamma^* \to \mu^+\mu^-$	108.5±3.4	3.9±0.6	1.2±0.3
$b\bar{b}$/W+jet	0.2 ±0.1	0.02±0.02	0.01±0.01
$Z/\gamma^* \to \tau^+\tau^-$	0.9±0.3	0.0±0.0	0.0±0.0
$t\bar{t}$	0.11±0.01	0.07±0.003	0.07±0.003
MC Sum	112±3.3±7.3	5.9±0.6±0.4	2.9±0.3±0.2

Table 6.2: *Expected number of background events and events observed after successive selections for an integrated luminosity of* $\mathcal{L} = 147\,\mathrm{pb}^{-1}$ *in the* $\mu^+\mu^-$ *channel. A cross-section of 13 pb is assumed for the WW events. The statistical error is listed for all backgrounds. The error due to the uncertainty of the integrated luminosity is only given for the sum of all backgrounds. The different cuts are summarised in Table 6.1.*

The cross-section σ can be estimated by minimising $-2\log L(\sigma, N_{obs}, N_{bg}, \mathcal{L}, BR, \varepsilon)$. For a combination of the channels the likelihood functions can simply be multiplied:

$$L_{\mathrm{comb}}(\sigma, N_{\mathrm{obs}}, N_{\mathrm{bg}}, \mathcal{L}, BR, \varepsilon) = \prod_{\mathrm{i}=1}^{N_{\mathrm{channel}}} \frac{\tilde{N}_{\mathrm{i}}^{N_{\mathrm{obs_i}}}}{N_{\mathrm{obs_i}}!} e^{-\tilde{N}_{\mathrm{i}}} \,. \tag{6.4}$$

The likelihood functions of the individual measurements are shown in Figure 6.4. The statistical error is derived from the intersection of the likelihood function with the y-value of the minimum of the likelihood function increased by one which is the one-σ-error interval under the assumption of Gaussian errors.

For the di–electron final state, the measurement yields a cross-section of [50]:

$$\sigma(\mathrm{p\bar{p}} \to \mathrm{WW}) = 13.73^{+15.67}_{-11.16}(\mathrm{stat.}) \pm 0.89(\mathrm{lumi.})\ \mathrm{pb}. \tag{6.5}$$

The measurement in the $\mathrm{e}^{\pm}\mu^{\mp}$ final state yields a cross-sections of [50]:

$$\sigma(\mathrm{p\bar{p}} \to \mathrm{WW}) = 11.78^{+7.20}_{-5.35}(\mathrm{stat.}) \pm 0.77(\mathrm{lumi.})\mathrm{pb}\,. \tag{6.6}$$

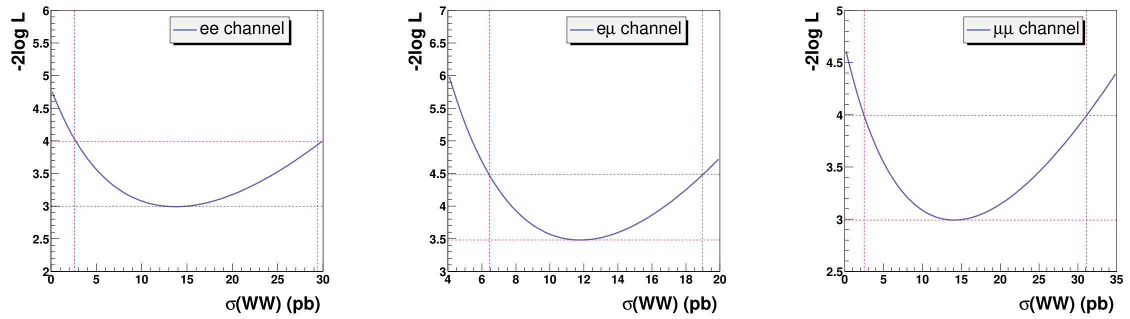

Figure 6.4: *Likelihood distributions for the* e^+e^- *(left),* $e^\pm\mu^\mp$ *(middle) and* $\mu^+\mu^-$ *channel (right).*

For the $\mu^+\mu^-$ final state, the measurement yields a cross-sections of

$$\sigma(\mathrm{p\bar{p}} \to \mathrm{WW}) = 14.07^{+17.01}_{-11.58}(\mathrm{stat.}) \pm 0.91(\mathrm{lumi.})\mathrm{pb}\,. \tag{6.7}$$

The likelihood functions of the individual measurements are shown in Figure 6.4.

The combined result of the cross-section measurement is

$$\sigma(\mathrm{p\bar{p}} \to \mathrm{WW}) = 12.44^{+5.90}_{-4.76}(\mathrm{stat.}) \pm 0.81(\mathrm{lumi.})\mathrm{pb}\,. \tag{6.8}$$

Figure 6.5 presents the likelihood distribution for the combined measurement. This preliminary result is in good agreement with the NLO-calculations of $\sigma(\mathrm{p\bar{p}} \to \mathrm{WW}) = 13.5\,\mathrm{pb}$ [16].

6.3 Systematic Uncertainties

Following the study on the systematic uncertainties on the search of $H \to WW^{(*)}$ production in Chapter 5.4 the following systematic uncertainties have been investigated on their effect on the WW cross-section in the di-muon channel:

- The change of the jet energy scale correction was tested by adding (subtracting) $\pm 25\%$ of every jet transverse momentum to the missing transverse energy $\not{E}_\mathrm{T}$. The cross-section changes by -21.5% and $+20.1\%$.
- The cross-sections of $Z/\gamma^* \to \mu^+\mu^-$ and $t\bar{t}$ production were lowered and raised simultaneously within their theoretical error of $\pm 3.6\%$ for $Z/\gamma^* \to \mu^+\mu^-$ and $+5.9\%$ or -14.7% for $t\bar{t}$ production. The cross-section changes by -2.7% and $+4.7\%$.

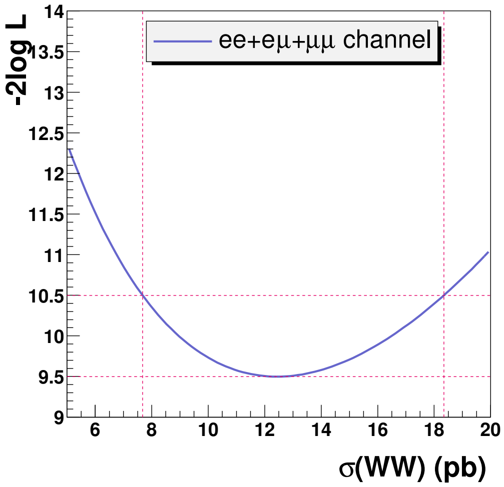

Figure 6.5: *Combined likelihood distribution from the* e^+e^-, $e^\pm\mu^\mp$ *and* $\mu^+\mu^-$ *channel.*

- The muon momentum smearing was varied by ±50% of the smearing parameter f. The cross-section changes by -17.0% and $+25.0\%$. This is a rather large effect since the background from $Z/\gamma^* \to \mu^+\mu^-$ production depends on a good description of the muon momentum resolution. This effect can be significantly lowered by reducing background from $Z/\gamma^* \to \mu^+\mu^-$ production.

All these variations add up to a systematic uncertainty on the WW cross-section in the di-muon channel of $+4.6\,\text{pb}$ and $-3.9\,\text{pb}$, respectively. The systematic uncertainties in the electron-electron and electron-muon channel are in the same range, but have not been finalised yet [50]. At the moment this measurement is statistically limited. Some systematic errors can also be lowered in future by a better background description in the MC, by a better accuracy of the jet energy scale correction and a better modelling of the μ momentum resolution.

7 Precise Muon Tracking

In the previous chapters it was shown that track finding with high precision and efficiency is an essential tool for the discovery of the Higgs boson and many other important measurements. This will also be a key issue of the physics programme at the next generation collider. The Large Hadron Collider (LHC) at CERN in Geneva, Switzerland, with a scheduled start in spring 2007, will collide protons at a centre of mass energy of $\sqrt{s} = 14\,\text{TeV}$. Due to the higher centre of mass energy and higher design luminosity, the discovery potential of the Higgs boson will be much higher at the LHC compared to the Tevatron collider. Two general purpose experiments, ATLAS and CMS, are currently built.

At hadron colliders leptons play an important role in the discovery of new physics. This was explicitly shown in the previous chapters for the search of the Higgs boson. Lepton identification and precise measurement of their momenta is also a key element for the detector design of the next generation experiments ATLAS and CMS at the LHC. The measurement accuracy of the momentum in a magnetic field scales with $\Delta p_{\mathrm{T}}/p_T^2 \approx$ const. at high energies. Therefore the effort for the magnetic measurement of momenta has to increase with the centre of mass energy of colliders. For electrons the magnetic measurement of momenta can be complemented by a calorimetric measurement of their total energy. For high momentum muons, however, precise tracking is the only feasible way to determine their momenta.

The investigation of $H \to WW^{(*)}$ is a typical example that an effort to have precise muon measurement as well as a precise electron measurement is rewarded by a factor of four in statistics. The tremendous effort which has to be invested for that is reflected in the name of both general purpose LHC experiments: ATLAS - “A Toroidal LHC ApparatuS” and CMS - “The Compact Muon Solenoid”.

The Cosmic Ray Measurement Facility at LMU Munich is part of the effort of the ATLAS experiment for a precise muon measurement. In the course of this thesis an alignment system has been developed and commissioned for this facility.

7.1 The ATLAS Muon Spectrometer

Figure 7.1 shows the outline of the ATLAS experiment with its different detector components. A detailed discussion of the different components and its performance can be found in [51]. Here only the muon spectrometer will be focused on. It is located at the outer most part of the ATLAS detector which has a diameter of 22 m and length of 44 m. The muon spectrometer is located inside an air-core coil with a toroidal magnetic field of average strength of 0.4 T. The spectrometer comprises three different detector types and is build into three layers. This construction design assures a muon track momentum measurement with high precision from the muon spectrometer only. Each muon track should be measured in at least three layers of the muon chambers and with the knowledge of the magnetic field map the muon momentum can be reconstructed from the sagitta of the track. The precision chambers (MDT chambers, monitored drift tube) are used for the bending coordinate measurement, which is parallel to the beam line in the central pseudo-rapidity range $|\eta| < 1$ and radial in the forward pseudo-rapidity range $|\eta| > 1$. The

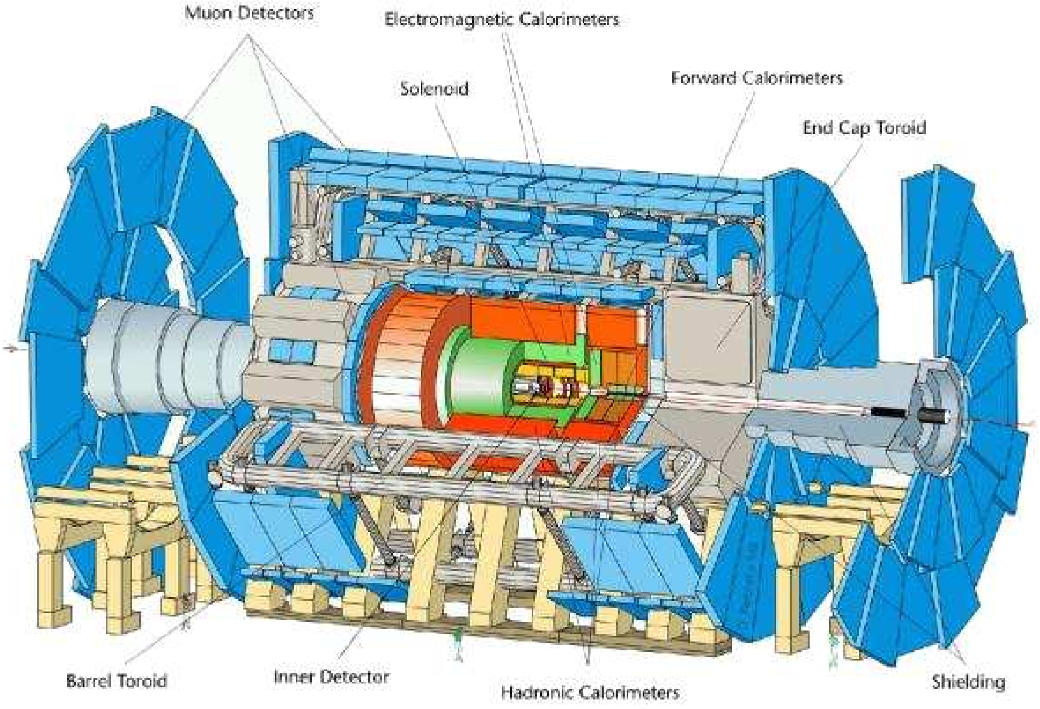

Figure 7.1: *Outline of the ATLAS detector [51].*

z-coordinate along the magnetic field needs only to be known to a precision of $5-10$ mm since it is not as important for the momentum measurement, but is required for a safe track reconstruction. This measurement is done by the trigger chambers.

The performance of the ATLAS muon spectrometer is driven by its physics programme and the resolutions needed e.g. to detect signals of new physics beyond the Standard Model. Several benchmark processes, in particular Standard Model and non-Standard Model Higgs boson decays have been studied and require a momentum and mass resolution at the level of 1% for the reconstruction of narrow two- and four-muon final states on top of high background levels. The process $H \rightarrow ZZ^{(*)} \rightarrow 4\mu$ is an important discovery channel for a Standard Model Higgs boson over a wide mass range m_{H} due to its clean signature with low backgrounds. For masses in the range $120\,\mathrm{GeV} < m_{\mathrm{H}} < 180\,\mathrm{GeV}$ a high mass resolution of about 1% is needed. To achieve this mass resolution a muon momentum resolution of $\Delta p_{\mathrm{T}}/p_{\mathrm{T}} < 2\%$ is required. It is desired that this momentum resolution is constant over the full pseudo-rapidity range. Figure 7.2 (left) shows that the muon spectrometer design corresponds to momentum resolution of $2\% - 3.5\%$ for muons in a momentum range $10\,\mathrm{GeV} < p_{\mathrm{T}} < 100\,\mathrm{GeV}$. In a combination with the tracks from the inner detector the momentum resolution improves quite significantly and meets the required resolutions (Figure 7.2 (right)). In this momentum range the muon spectrometer only measurement is limited due to multiple scattering in the chamber material

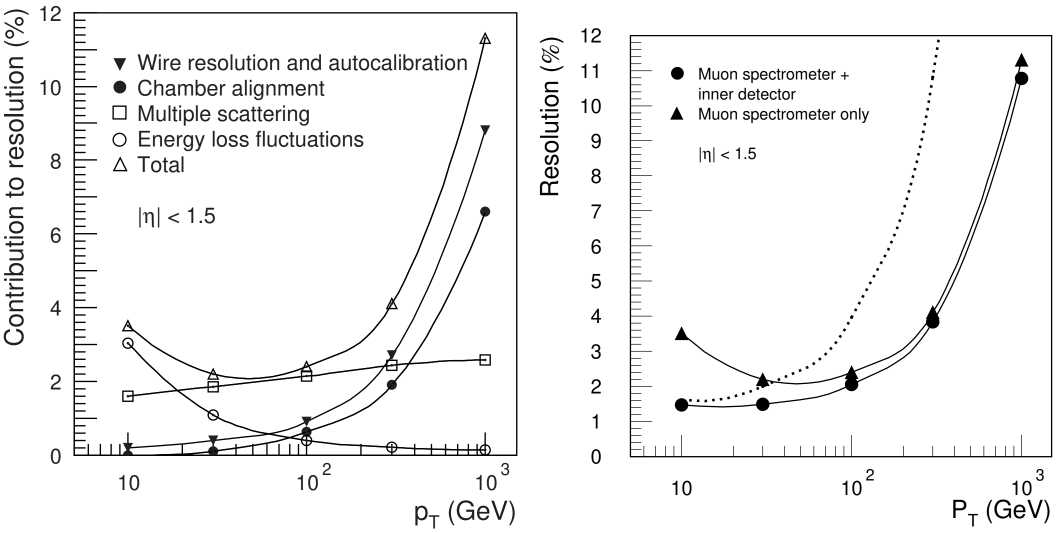

Figure 7.2: *Left: $\Delta p\mathrm{T}/p_{\mathrm{T}}$ as a function of transverse momentum p_{T} for muons reconstructed in the central region ($\eta < 1.5$). Right: the p_{T}-dependence of the muon momentum resolution averaged over the azimuthal angle and in the range $|\eta| < 1.5$. The dashed curve is the resolution for the inner tracker only, with known transverse beam position [52].*

and magnet structure, as well due to energy loss fluctuations in the calorimeter. For B-physics in contrast the muon transverse momenta are typically small and here the muon spectrometer is mainly used for muon triggering. A high pseudo-rapidity coverage and trigger efficiency is desired from the muon spectrometer. The muon track momentum is determined with the inner tracker.

For high muon momenta the chamber alignment plays an important role in the muon momentum resolution. This is an important lesson that can already be learnt from results of the DØ experiment. The observation of the Z boson resonance is not possible with the DØ muon system only. The intrinsic resolution and alignment between the muon chambers is not sufficient for a proper momentum resolution in the momentum range shown in Figure 4.6. A reasonable momentum resolution is only achieved by matching the muon chamber hits to their corresponding tracks in the central silicon and fibre tracker. Also here the internal sub-detector alignment and the alignment between the different detector has a major impact on the momentum resolution. As seen in Figure 4.5 Monte Carlo simulation with ideal detector geometry and alignment assumptions predicts a Z boson width of approximately 6 GeV. Older versions of the reconstruction software predicted a Z boson width in data of about 14.5 GeV compared to 7.5 GeV with the current version. This large difference between the two different reconstruction versions is due to wrong alignment assumptions between an ideal detector model implemented in the old reconstruction software and a better modelling of the "as built" detector geometry in the current software version. From Monte Carlo, however, still some improvements are expected and ongoing studies point to smaller smaller effects due to misalignment or dead detector material.

The ATLAS muon spectrometer has two types of trigger chambers: RPC (resistive plate chambers) in the barrel and TGC (thin gap chambers) in the end-cap region. The gas filled RPC chambers consist of bakelite plates separated by 2 mm and attached to a high voltage field. They provide a position resolution of about 1 cm and a timing resolution of about 1 ns. The TCG chambers operate like multi-wire proportional drift chambers and have a similar resolution like RPC chambers.

MDT chambers are drift tube chambers that consist of two four-layer drift tubes in the inner part of the ATLAS muon spectrometer. In the two outer layers the chambers are built in two triple-layers of drift tubes. Depending on the location of the chambers in the ATLAS detector, the drift tubes are of one to six metres length. The tubes have a diameter of 30 mm. Tube walls are made of aluminium with 400μm thickness. The tungsten-rhenium anode wire has a diameter of 50μm. The drift tubes are filled with a gas mixture of $\mathrm{Ar}-\mathrm{C0_2}$ with in a ratio of $93:7\%$ and a gas pressure of 3 bar. They are operated at a voltage of 3080 V and have a linear gas gain of $2\cdot 10^4$. The drift radius of the secondary electrons induced by ionising muons can be measured with a precision of 80μm. Knowing the anode wire position up to 30μm, a track point can be measured with a precision of 33μm for a three-layer chamber or 28μm for a four-layer chamber. Muons with a transverse momentum of $p_{\mathrm{T}} < 1000\,\mathrm{GeV}$ can be measured with a momentum resolution of $\Delta p_{\mathrm{T}}/p_{\mathrm{T}} \leq 10^{-4} \cdot p_{\mathrm{T}}/\mathrm{GeV}$.

In addition to the precise chamber and tube geometry the good track position measurement is provided by an alignment system within and between the muon drift chambers. This system monitors the chamber deformations caused by thermal or mechanical tensions. The core of this system is the so called Rasnik-System (Red alignment system NIKHEF) [52]. Figure 7.3 shows the mode of operation of the Rasnik-System. The basic idea is the projection of a mask with modified chess board pattern onto a CCD sensor. The mask is lit by a infrared high intensity LEDs with a wave length of 875 nm. The mask is a high accuracy ($< 0.5\mu$m) thin-film/glass slide as used in semiconductor industry and has a size of $20\,\mathrm{mm} \cdot 20\,\mathrm{mm}$ with a grid of 120μm. The projection is done by a quartz crystal convex lens with a focal length between 300 mm and 1000 mm and a diameter of 40 mm. The CCD sensor is a commercial monochrome CMOS image sensor with a pixel array size of $387 \cdot 287$ and a pixel size of $12\mu\mathrm{m} \cdot 12\mu\mathrm{m}$. The projected image is fed into a multiplexer and then digitised by a monochrome frame-grabber card operated in a PC. Movements in all three dimensions and rotations are calculated by a analysis software and can be measured in steps of about 1 sec if necessary. Movements transverse to the optical axis can be measured with an accuracy up to 2μm. Movements along the optical axis are measured from the image size with about one order of magnitude less precision. Figure 7.4 shows the resolution of (1.9 ± 0.1) mm obtained from a constant movement of the mask in 62.5μm steps transverse to the optical axis.

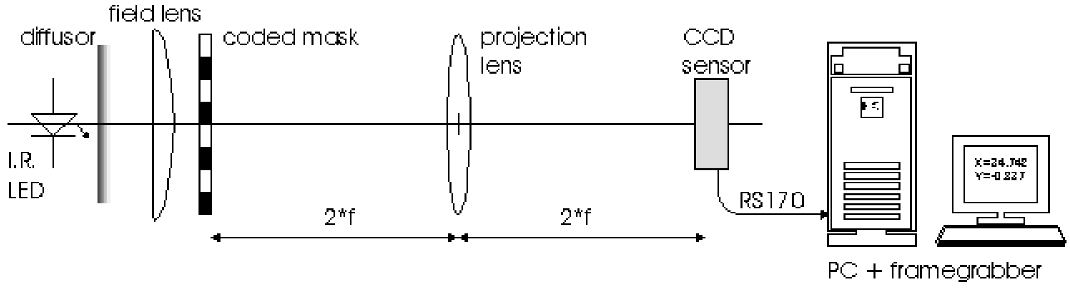

Figure 7.3: *Working principle of the Rasnik system.*

Figure 7.5 shows the outline of a ATLAS MDT chamber together with the light beams of the Rasnik alignment system. The light beams parallel to the long beam measure the transverse movements with high precision whereas the diagonal beams measure the longitudinal motions. With the combination of all four beams chamber distortions in all directions can be measured.

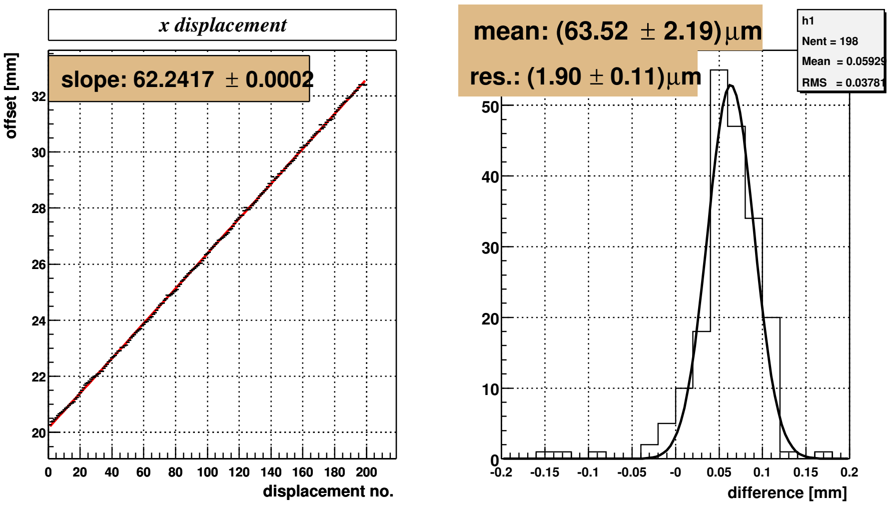

Figure 7.4: *Resolution of the Rasnik system transverse to the optical axis. The mask was moved in small steps (left) of* $62.5\,\mathrm{mum}$*. The resolution calculated from this variation is* $(1.9 \pm 0.1)\,\mathrm{mm}$.

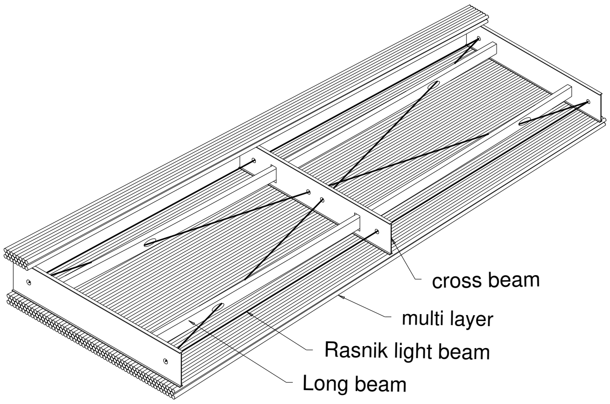

Figure 7.5: *Outline of a ATLAS MDT chamber with Rasnik alignment system.*

7.2 The Cosmic Ray Measurement Facility

7.2.1 General Setup

The cosmic ray measurement facility at LMU Munich allows efficiency tests and calibration studies of 88 drift tube chambers built for the ATLAS muon spectrometer at CERN [53]. Every chamber is tested for operativeness, noise and their single tube drift-time spectra. Extensive electronic and mechanical tests are performed. The positions of the single tube wires are determined and measured with respect to an external reference platform.

Muons from cosmic rays are steadily produced in the upper atmosphere by highly energetic protons hitting onto atom nuclei. In these collisions pions are produced that weakly decay into muons and neutrinos. The mean energy of muons at ground level is $\approx 4\,\mathrm{GeV}$. The energy integrated intensity of vertically incidenting muons above $1\,\mathrm{GeV}$ at sea level is $\approx 70\,\mathrm{m}^{-2}\mathrm{s}^{-1}\mathrm{sr}^{-1}$ [18].

Figure 7.6 shows the a sketch of the cosmic ray measurement facility. Three chambers are mounted on top of each other with a spatial distance of 80 mm between each of them. The top and the bottom chamber are the so called “reference” chambers. The wire positions of these two chambers have been determined at the CERN X-ray tomograph with a precision of about 4μm. In between these two chambers a “test” chamber is placed and measured with respect to the two other chambers. During the planned operation time of several hours to days the relative position of the three muon chambers with respect to each other must be known. These positions may vary in the order of a few μm because of mechanic tensions or thermal movements. To determine the precision coordinate of the single drift tube with a precision of about 10μm, the relative movement of the chambers should be know better than 5μm.

7.2.2 The Alignment System

Two different systems are used to monitor the positions. Movements of the test chamber are monitored by a capacitive system with respect to the upper reference chamber [54]. Capacitive sensors mounted on four corners on the lower side of the upper reference chamber measure movements with respect to the middle test chamber. For this thesis a second system to measure the movements of the two outer reference chambers relative to each other has been designed and implemented. Optical alignment systems based on the Rasnik technology described in the previous sections are installed at every corner of the reference chambers.

The main task of the reference chamber monitoring system is the control of coordinates transverse to the tube wire, namely the y- and z-component (Fig. 7.6). The reference

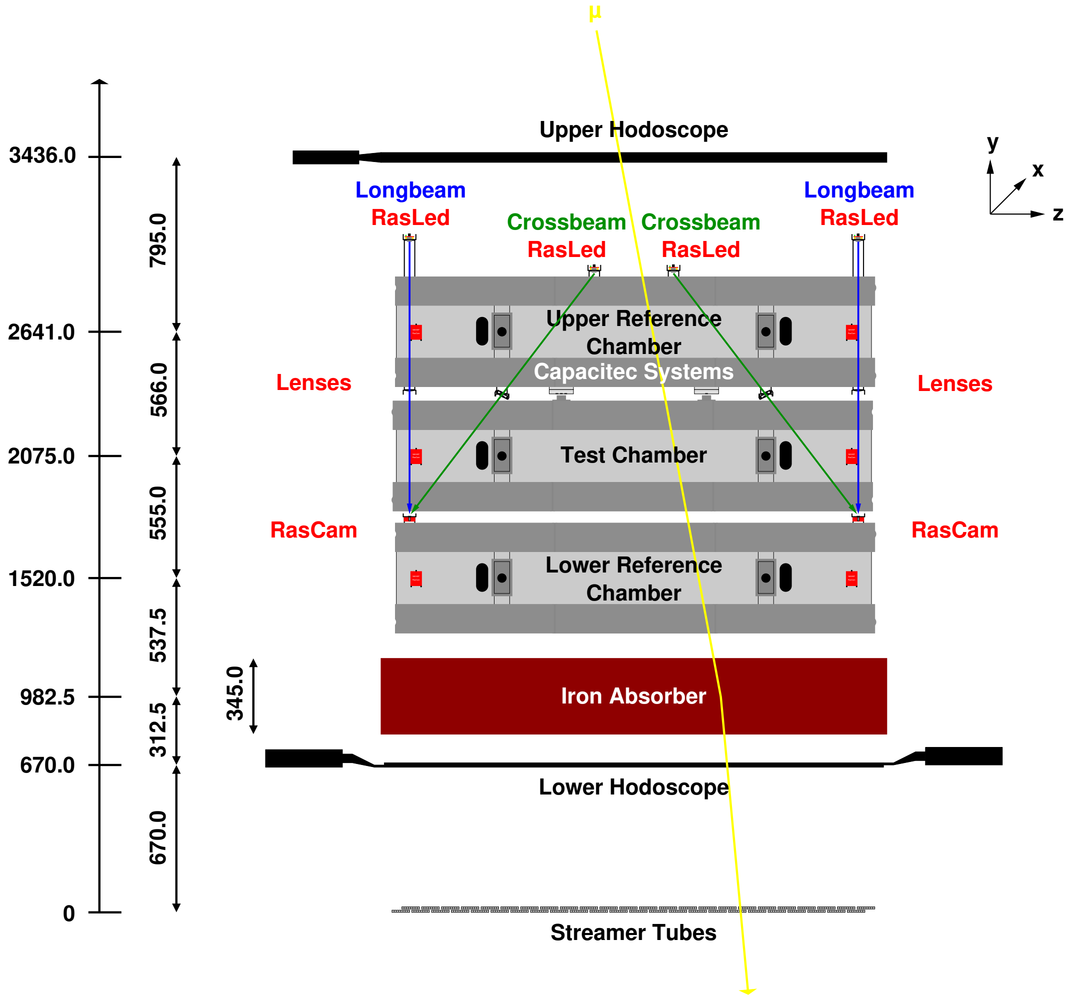

Figure 7.6: *Front view of the sensor mounting scheme on the MDT chambers in the cosmic ray measurement facility. The blue and green arrow lines sketch the infrared light rays from the mask through the lens to the sensor. Both sides of the measurement facility hold the shown alignment system.*

chamber monitoring system consists of four Rasnik systems on every corner of the chambers. These systems are capable of measuring the x- and z-coordinate with high precision. Two components, the mask and lens, are mounted on the top chamber and one component, the CCD, is mounted on the bottom chamber. In order to monitor the y-component with a similar accuracy, four additional Rasnik systems are mounted in diagonal setups. The stereo angle measurement is about three times less precise. More detailed mechanical drawings of the outline of the Rasnik system are given in Appendix A.

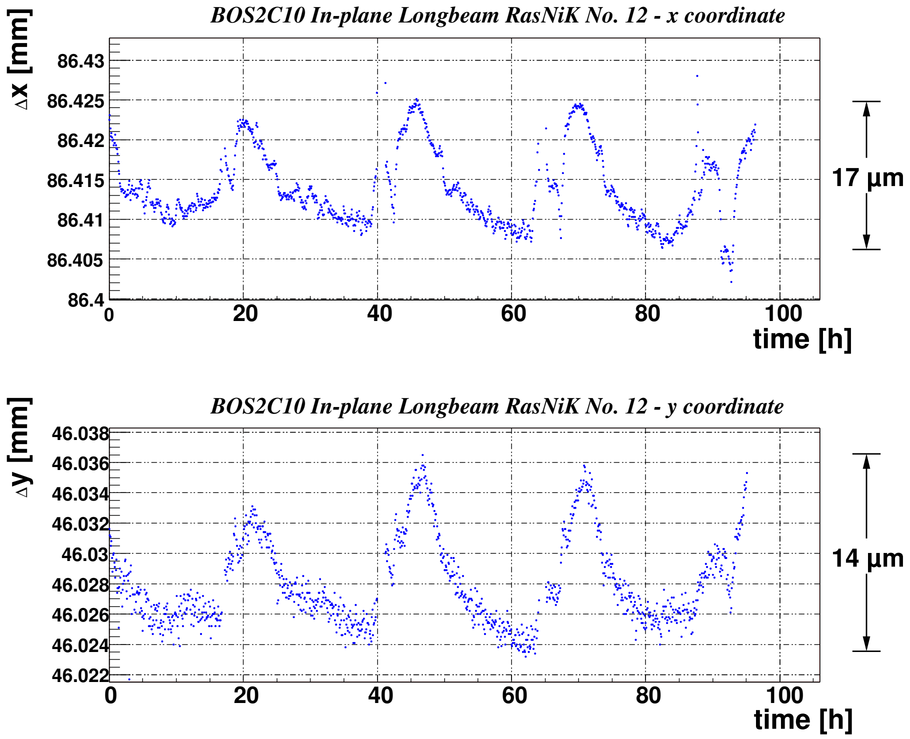

Figure 7.7: *The Figure shows the movements in x (top) and y direction (bottom) measured with the chamber in-plane Rasnik system due to day and night temperature changes. The range is good agreement with the temperature variations.*

The measurement facility is operated in an air-conditioned hall with a temperature stabilised at $(20.0 \pm 2.0)^\circ$C. Aluminium as main component of the chambers has a linear extension coefficient of about 23μm for one meter of material at a temperature change of 1°K. Figure 7.7 shows the variation of the chamber geometry due to the hall temperature changes during several day and night cycles. The variations of the chamber geometry within 17μm and 14μm, respectively, are consistent with the short term temperature variations of ± 0.5K within the hall.

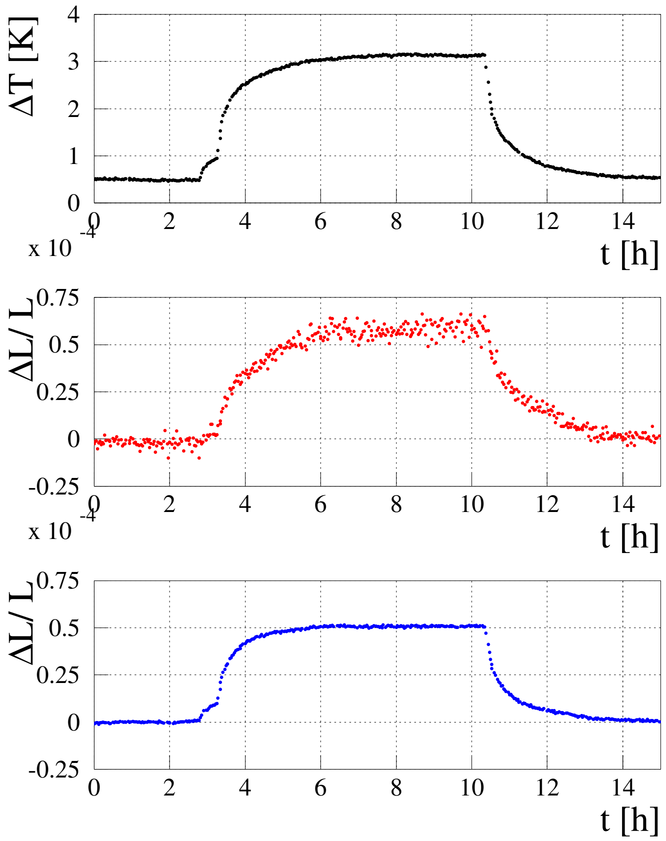

Figure 7.8: *The Figure shows the controlled temperature change in time (top), the movements measured with the reference chamber Rasnik system (middle), and the movements measured with the internal Rasnik system (bottom).*

7.2.3 Performance of the Alignment System

The performance of the reference chamber Rasnik system has been tested by a controlled temperature change of test stand setup. One cross-plate of the upper reference chamber was heated by $\Delta T \approx 2.7\,\mathrm{K}$ for about 10 h [55]. The temperature reached its maximum and the original temperature after the heating in approximately 2 h The aluminium cross beam of the muon chamber was constantly heated over its full length. A theoretical expansion of $\Delta L/L \approx 60\mu\mathrm{m}$ of pure aluminium is expected from this temperature change. The top histogram in Figure 7.8 shows the temperature change with time. The lower plot shows the chamber geometry change in z direction calculated from a trapezoidal fit to the chamber geometry measured with the in-plane Rasnik system. A direct correlation between the temperature change and the chamber deformation is visible. The middle plot of Figure 7.8 shows the chamber deformation measured with the reference chamber Rasnik system. There is a slight delay visible between the temperature change and chamber deformation change. This is due to the fact that the reference chamber Rasnik system is mounted onto the drift tubes without stiff connection to chamber cross beam which was heated up.

Figure 7.9 shows the differential plot of the relative chamber expansion with respect to the temperature change measured with the chamber in-plane Rasnik system. The hatched line corresponds to the theoretical prediction of a linear expansion of the cross beam due to heating. The dots corresponds to the measured expansion from a fit to the chamber geometry. There is good agreement between the measurement and the prediction for small temperature changes. There is also only a small hysteresis visible, since the in-plane Rasnik system is directly mounted on the heated cross beam. The deviations of the measurement from the linear predictions at high ΔT can be explained by mechanical constraints of the chamber construction and uncertainties in the measurement and fitting technique.

Figure 7.10 shows a similar differential plot expansion with respect to the temperature change but now measured with the reference chamber Rasnik system. A prominent hysteresis is visible over the full range of the temperature change. As mentioned earlier the reference chamber Rasnik system is not in direct contact with the heated cross beam which causes the strong expected hysteresis. There is good agreement between data and theoretical prediction over the full range for the temperature change with the given hysteresis. It is important to include trapezoidal distortions of the chamber geometry into the fitting procedure. The chamber readout electronic is mounted only on one cross-plate side. Therefore this chamber side is a few K warmer than the other side without mounted readout electronics.

The reference chamber Rasnik system shows the expected performance and is able to monitor chamber movements in the required range of a few micrometres. The measured movements due to temperature changes or mechanical tensions provide corrections to the determination of wire positions in the muon drift chambers. The operation of the entire facility is expected to provide valuable input to the design of the online calibration procedures which will be needed during LHC operation to achieve the required muon momentum resolution.

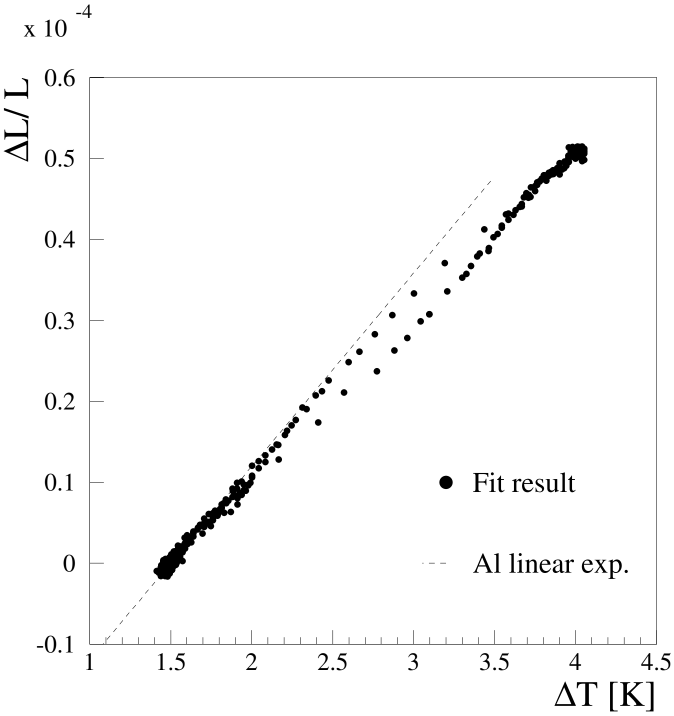

Figure 7.9: *The Figure the movements of the z-coordinate of the internal Rasnik system of the upper reference chamber due to a controlled temperature change. The hashed line shows the theoretical prediction given by the aluminium expansion coefficient.*

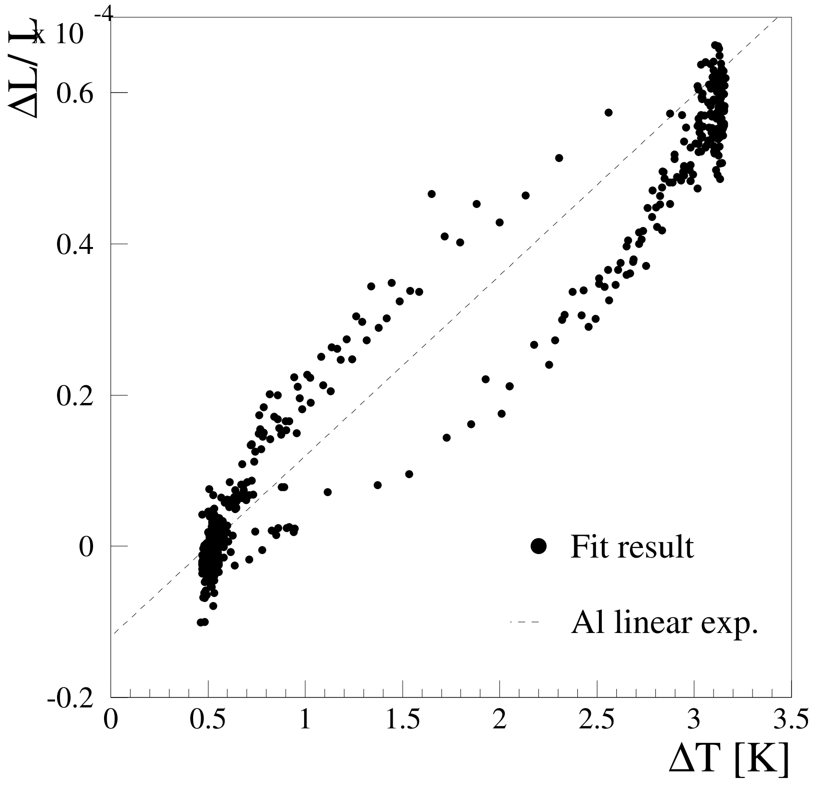

Figure 7.10: *The Figure shows the movements of the z-coordinate of the reference chamber Rasnik system due to a controlled temperature change. The hashed line shows the theoretical prediction given by the aluminium expansion coefficient.*

8 Conclusions

The generation of fermion and weak gauge boson mass is one of the experimental unsolved problems of the Standard Model of particle physics. The standard solution is "Higgs mechanism" with the introduction of elementary scalar fields ϕ that spontaneously break the gauge symmetry, leaving an, as yet unobserved, massive scalar boson, the Higgs boson. In $p\bar{p}$ collision at the Tevatron collider with a centre of mass energy of $\sqrt{s} = 1.96\,\mathrm{TeV}$ the main production mechanism of the Higgs boson is the gluon-gluon fusion with a production cross-section of approximately $2-0.1\,\mathrm{pb}$. In this thesis results were presented from the search of the Higgs boson in its decay channel to two W bosons. This decay channel is most sensitive for a Standard Model Higgs boson mass $m_\mathrm{H} > 140\,\mathrm{GeV}$.

Data taken with the DØ experiment between April 2002 and September 2003 with an integrated luminosity of $\mathcal{L} \approx 147\,\mathrm{pb}^{-1}$ has been analysed. The emphasis was placed on the di-muon decay channel $H \to WW^{(*)} \to \mu^+\nu_\mu\mu^-\bar{\nu}_\mu$ of the two W bosons. Different efficiencies of trigger and reconstruction were determined. A well motivated cut-based analysis was developed to reduce main backgrounds from $Z/\gamma^* \to \mu^+\mu^-$, $Z/\gamma^* \to \tau^+\tau^-$, $WW \to \mu^+\nu_\mu\mu^-\bar{\nu}_\mu$, $t\bar{t}$, $b\bar{b}$ and W+jets production. The observed data was compared to Monte Carlo predictions of the various backgrounds. The $b\bar{b}$ contribution was determined from data and Monte Carlo. After all cuts 5 events remain in data with a Standard Model background expectation of 5.3 ± 0.6 events. The dominant remaining backgrounds are $Z/\gamma^* \to \mu^+\mu^-$ and $WW \to \mu^+\nu_\mu\mu^-\bar{\nu}_\mu$ production. Since no excess of the data is observed, upper limits on the cross-section of $H \to WW^{(*)}$ have been calculated at 95% C.L. for six Higgs boson masses in the range of $100\,\mathrm{GeV} < m_\mathrm{H} < 200\,\mathrm{GeV}$. The calculated cross-section limits range from $82.7\,\mathrm{pb}$ for $m_\mathrm{H} = 100\,\mathrm{GeV}$ to $17.1\,\mathrm{pb}$ for $m_\mathrm{H} = 160\,\mathrm{GeV}$ with the most sensitivity. A combination of limits with the di-electron and electron-muon channels yield about two to three times better limits on $H \to WW^{(*)}$ with $40.1\,\mathrm{pb}$ for $m_\mathrm{H} = 100\,\mathrm{GeV}$ to $5.7\,\mathrm{pb}$ for $m_\mathrm{H} = 160\,\mathrm{GeV}$. No mass regions of a Standard Model Higgs boson or alternative model can yet be excluded. The presented analysis is easily scalable to the expected 50 times larger integrated luminosity of the full Tevatron Run II dataset in 2009. With the final data set certain mass regions of the Standard Model Higgs boson can be excluded at 95% C.L.

One of the dominant remaining backgrounds in the search for the Higgs boson in the decay channel $H \rightarrow WW^{(*)} \rightarrow l^{+}\nu l^{-}\bar{\nu}$ is the WW production. This background needs to be well understood before placing final limits on the $H \rightarrow WW^{(*)}$ production and has only been partially measured in $\mathrm{p\overline{p}}$ collision. A limit of $\sigma_{\mathrm{WW}} < 43.1\,\mathrm{pb}$ has been determined at 95% C.L. in the di-muon channel with similar cuts presented in the $H \rightarrow WW^{(*)} \rightarrow \mu^{+}\nu_{\mu}\mu^{-}\bar{\nu}_{\mu}$ analysis case. A first measurement of the combination of the di-muon, di-electron and electron-muon final state yield a cross-section of $\sigma(\mathrm{p\overline{p}} \rightarrow \mathrm{WW}) = 12.44^{+5.90}_{-4.76}(\mathrm{stat.}) \pm 0.81(\mathrm{lumi.})\mathrm{pb}$.

In the first chapters it was shown that track finding with high precision and efficiency is essential for the discovery of the Higgs boson and many other important measurements. From 2007 onwards the Large Hadron Collider, LHC, will collide protons at a centre of mass energy of $\sqrt{s} = 14\,\mathrm{TeV}$. The ATLAS experiment with its distinct muon system is one of two general-purpose experiments which will take up the challenge. At the LMU Munich Cosmic Measurement Facility 88 chambers of the muon chambers are tested for operativeness, noise and their single tube drift-time spectra. An alignment system with Rasnik infrared sensors was developed and commissioned to monitor chamber movements in this test-stand, which works well within the specifications.

A Outline of the Alignment System

In Chapter 7 an alignment system for the Cosmic Ray Measurement Facility was presented. Figure 7.6 shows an outline of the chamber positions and the positions of the alignment systems. Detailed mechanical drawings of the Rasnik system positions are given in a front view in Figure A.1 and in a side view in Figure A.2. All parts are fixed by a fixture piece that is glued onto the chamber drift tubes surface (top plot in Figure A.3). This piece fits into the spacing between two drift tubes and offers a very stable fixture possibility for all kind of devices that need to be placed directly onto the chamber surface.

As an example for the bars, that hold the different Rasnik components, the CCD bar is explained in more detail. The bottom plot in Figure A.3) shows the step that is screwed on the fixture piece to provide the correct distance in the optical system and to fit the fixture into the free space between the reference and test chamber. The 2 mm thickness of the aluminium sheet was chosen to provide the necessary stiffness of the step. Figure A.4 shows the bar that holds the CCD box. This bar is screwed onto the step from Figure A.3. The U-shape of the bar and the thickness of 1 mm prevent the bar from unintentional deflections in all directions. The positions of all parts in the measurement facility are designed to deal with different test chamber positions in the test setup.

Similar fixtures have been designed for the Capacitive alignment system. These are glued and screwed between the upper reference chamber and the test chamber. All fixtures are made from aluminium to have the same expansion coefficient like the drift chamber material.

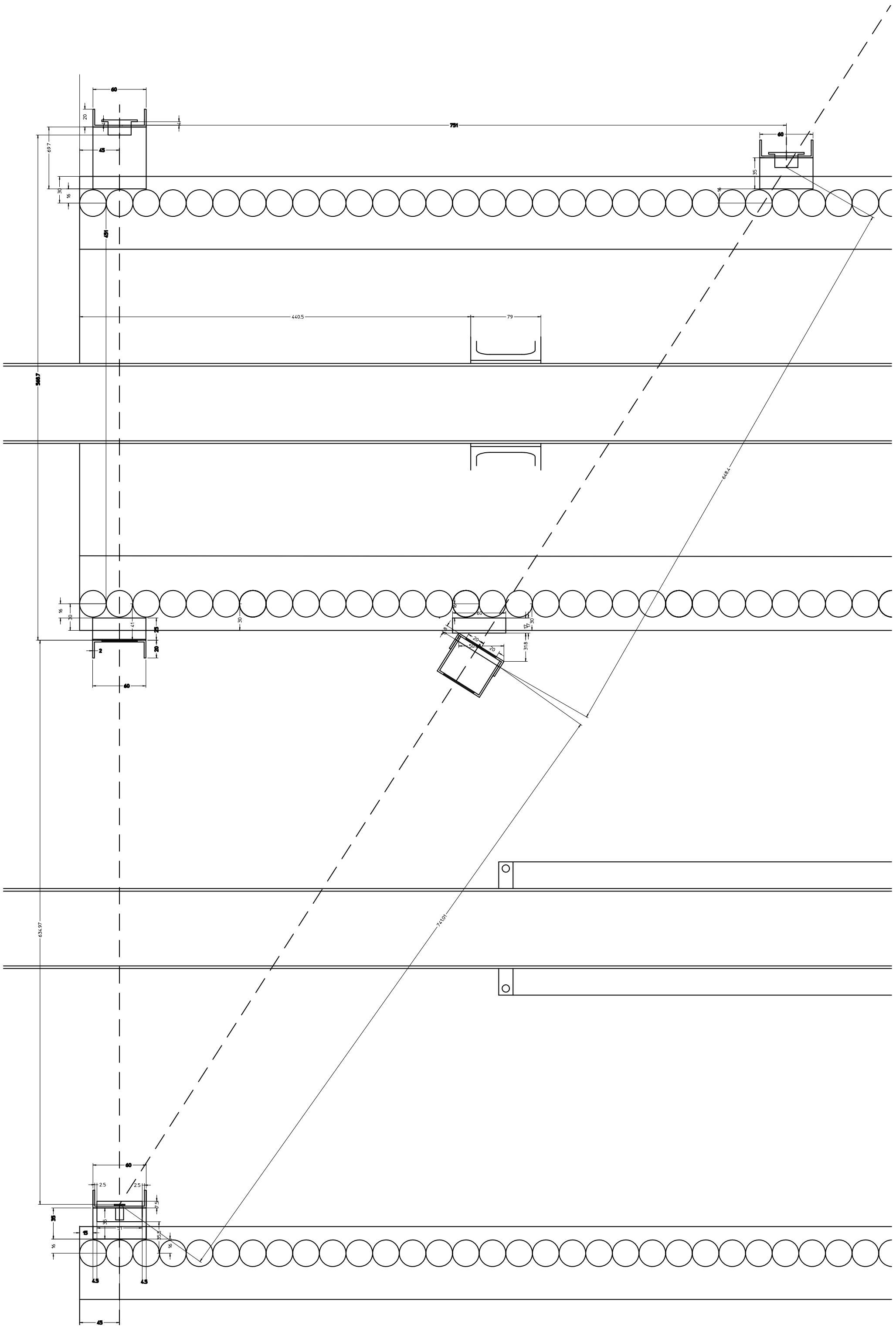

Figure A.1: *Cutout of the front view of the Cosmic Ray Measurement Facility. The circles indicate one drift tube layer. It is shown the top reference chamber and the top part of the lower reference chamber together with the fixtures of the Rasnik system components CCDs, mask and lenses. The dashed lines indicate the light rays of the Rasnik system.*

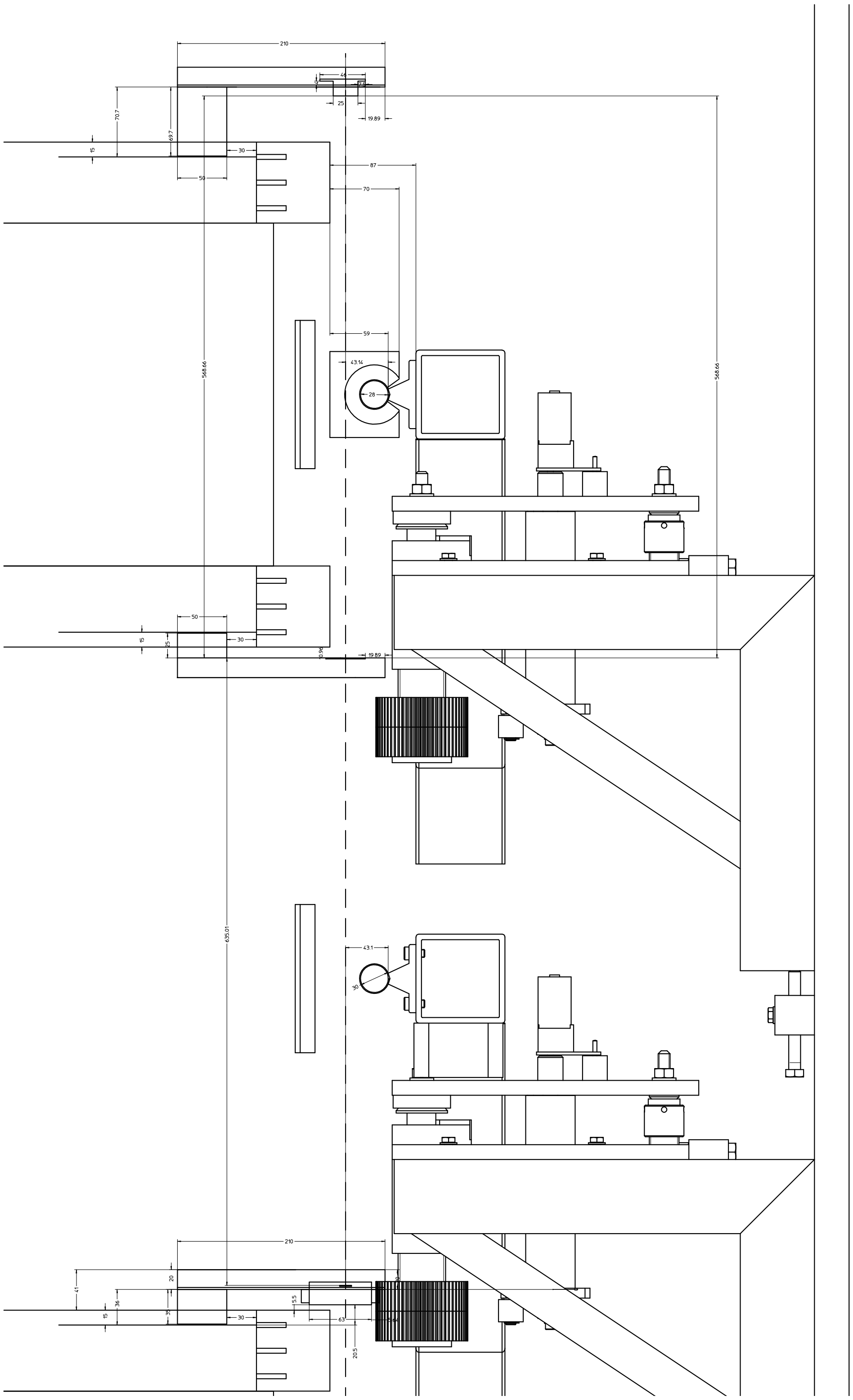

Figure A.2: *Cutout of the side view of the Cosmic Ray Measurement Facility. The left bars indicate one drift tube layer. It is shown the top reference chamber and the top part of the lower reference chamber together with the fixtures of the Rasnik system components CCDs, mask and lenses. The dashed line indicates the light rays of the Rasnik system.*

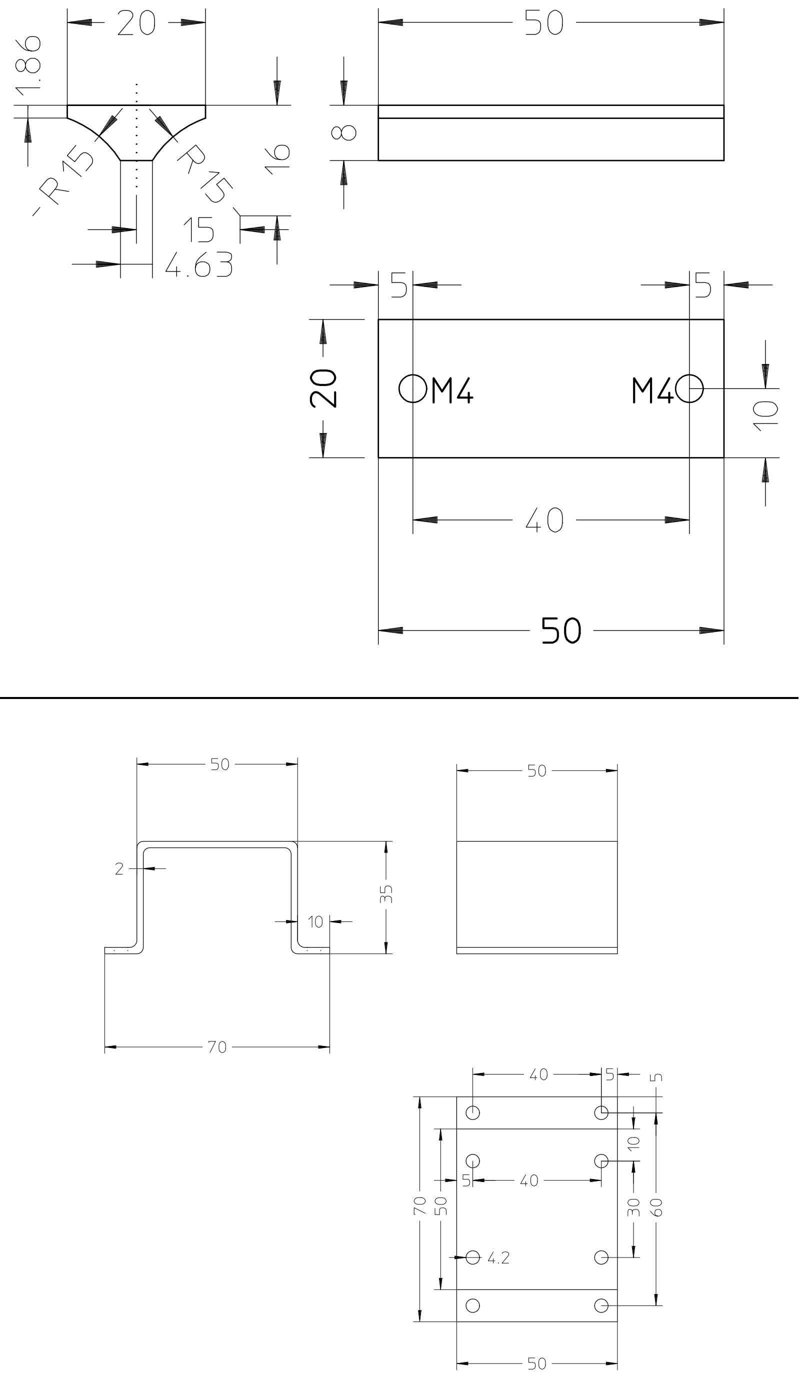

Figure A.3: *Top: mechanical drawing of the fixture piece that is glued onto this drift chambers to hold the CCD, mask or lens bars. Bottom: step for the CCD bar screwed to the top fixture piece to provide the correct distance in the Measurement Facility.*

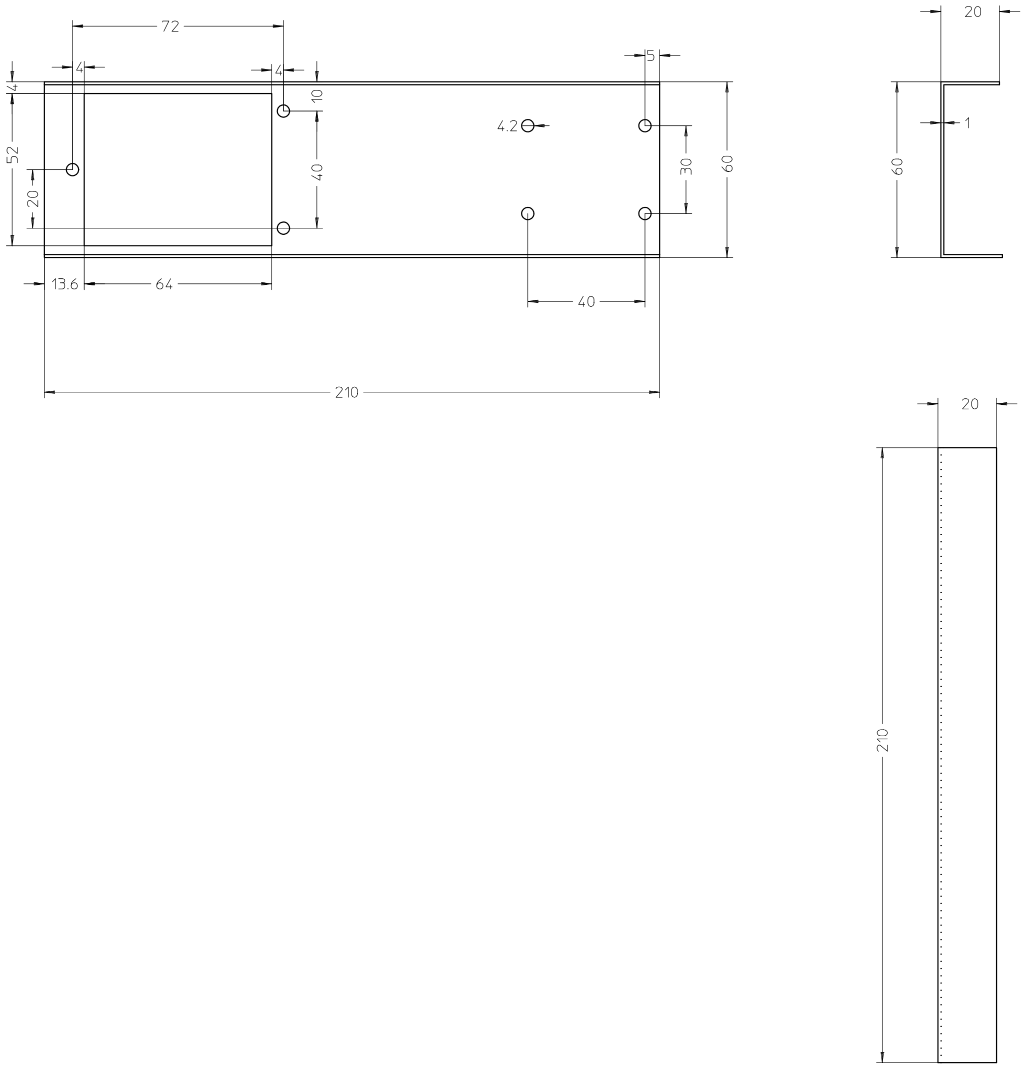

Figure A.4: *Mechanical drawing of the CCD bar that is screwed to the step from Figure A.3 and holds the CCD box.*

Bibliography

[1] The LEP Working Group for Higgs Boson Searches, *Search for the Standard Model Higgs Boson at LEP*, CERN-EP/2003-011.

[2] The LEP and SLD Collaborations, *A Combination of Preliminary Electroweak Measurements and Constraints on the Standard Model*, hep-ex/0312023.

[3] D. J. Griffiths, "Introduction To Elementary Particles," Wiley Text Books, 1987.

[4] M. K. Gaillard, P. D. Grannis and F. J. Sciulli, Rev. Mod. Phys. 71 (1999) S96, hep-ph/9812285.

[5] P. Aliani, V. Antonelli, M. Picariello and E. Torrente-Lujan, Phys. Rev. D 69 (2004) 013005, hep-ph/0212212.

[6] D. N. Spergel *et al.*, Astrophys. J. Suppl. 148 (2003) 175, astro-ph/0302209.

[7] P. W. Higgs, Phys. Lett. 12 (1964) 132, Phys. Lett. 13 (1964) 508, Phys. Rev. 145 (1066) 1156;
F. Englert and R. Brout, Phys. Rev. Lett. 13 (1964) 321;
G. S. Guralnik, C. R. Hagen and T. W. B. Kibble, Phys. Rev. Lett. 13 (1964) 585;
T. W. B. Kibble, Phys. Rev. 155 (1967) 1554.

[8] M. Carena *et al.* [Higgs Working Group Collaboration], "Report of the Tevatron Higgs working group," hep-ph/0010338.

[9] J. F. Gunion, H. E. Haber, G. L. Kane and S. Dawson, "The Higgs Hunter's Guide," Perseus Publishing, Reading, MA, 2000.

[10] R. K. Ellis, W. J. Stirling and B. R. Webber, Cambridge Monogr. Part. Phys. Nucl. Phys. Cosmol. 8 (1996) 1.

[11] M. Spira, Report DESY T-95-05 (October 1995), hep-ph/9510347 `http://people.web.psi.ch/spira/proglist.html`.

[12] A. Djouadi et al., Comp. Phys. Commun. 108 (1998) 56, hep-ph/9704448.

[13] R. Hamberg, W. L. van Neerven and T. Matsuura, Nucl. Phys. B 359 (1991) 343 [Erratum-ibid. B 644 (2002) 403].

[14] K. Hagiwara, J. Woodside and D. Zeppenfeld, Phys. Rev. D 41 (1990) 2113.

[15] H. L. Lai *et al.*, Phys. Rev. D 55 (1997) 1280, hep-ph/9606399.

[16] J. M. Campbell and R. K. Ellis, Phys. Rev. D 60 (1999) 113006, hep-ph/9905386.

[17] E. Arik, M. Arik, S. A. Cetin, T. Conka, A. Mailov and S. Sultansoy, Eur. Phys. J. C 26 (2002) 9, hep-ph/0109037.

[18] K. Hagiwara *et al.* [Particle Data Group Collaboration], Phys. Rev. D 66 (2002) 010001.

[19] L. Brucher and R. Santos, Eur. Phys. J. C 12 (2000) 87, hep-ph/9907434.

[20] T. Sjostrand, P. Eden, C. Friberg, L. Lonnblad, G. Miu, S. Mrenna and E. Norrbin, Comput. Phys. Commun. 135 (2001) 238, hep-ph/0010017.

[21] H. L. Lai *et al.* [CTEQ Collaboration], Eur. Phys. J. C 12 (2000) 375, hep-ph/9903282.

[22] G. Andersson, G. Gustason, G. Ingelman und T. Sjöstrand, Phys. Rep. 97 (1983) 31.

[23] GEANT, CERN Program Library Long Writeup W5013, Version 3.21, (1995).

[24] The DØ Collaboration, S.Abachi et al., *The DØ Upgrade: The Detector and its Physics*, Fermilab Pub-96/357-E (1996).

[25] S. Klimenko *et al.*, FERMILAB-FN-0741(2003).

[26] B. Casey *et al.*, *"The Updated DØ Luminosity Determination"*, DØ Note 4328.

[27] T. Christiansen, *Search for Second-Generation Leptoquarks in* $p\bar{p}$ *Collisions,Ph.D. thesis*, LMU Munich, 2003.

[28] D. Whiteson,*"Global Track Finding at Level 3"*, DØ Note 3808.

[29] Muon-ID certification v3.0
`http://www-d0.fnal.gov/phys_id/muon_id/d0_private/muon_id.html`

[30] Common sample group - What Data to use for Analysis
`http://www-d0.fnal.gov/Run2Physics/cs/index.html`

[31] G. C. Blazey *et al.*, "Run II jet physics," hep-ex/0005012.

[32] Certified Jet Energy Scale v4.2
`http://www-d0.fnal.gov/phys_id/jes/d0_private/certified/certified.html`

[33] DØ Jet and MET ID Properties in p11 and p13
`http://www-d0.fnal.gov/~d0upgrad/d0_private/software/jetid/certification/v2_0/jetid_p13.html`

[34] Luminosity-ID, Accessing Luminosity Information
`http://www-d0.fnal.gov/phys_id/luminosity/data_access/`

[35] Offline Run Quality Database
`http://d0db.fnal.gov/qualitygrabber/qualQueries.html`

[36] The DØ Collaboration, V.M. Abazov *et al.*, Phys. Rev. D 67, 012004 (2003).

[37] M. Agelou *et al.*, *"Measurement of the Inclusive* $W \to \mu\nu$ *Cross-Section in* $p\bar{p}$ *Collisions at* $\sqrt{s} = 1.96\,\mathrm{TeV}$*"*, DØ Note 4128.

[38] E. Nurse *et al.*, *"Measurement of* $\sigma \cdot Br$ *for* $Z \to \mu^+\mu^-$ *in* $p\bar{p}$ *Collisions at* $\sqrt{s} = 1.96\,\mathrm{TeV}$*"*, DØ Note 4114.

[39] The DØ Collaboration, S. Abachi et al., Phys. Rev. Letters 75 1456 (1995).

[40] J. Elmsheuser, *"Background studies for the search of the Higgs boson in the channel* $H \to WW^{(*)} \to \mu^+\nu_\mu\mu^-\bar{\nu}_\mu$ *at DØ in Run II"* , DØ Note 4121.

[41] E. W. N. Glover, J. Ohnemus and S. S. D. Willenbrock, Phys. Rev. D 37 (1988) 3193.

[42] DØ EvtGen Webpage
`http://www-d0.fnal.gov/computing/MonteCarlo/generator_tools/evtgen.html`

[43] DØ d0_mess Webpage
`http://www-d0.fnal.gov/computing/MonteCarlo/generator_tools/d0_mess.html`

[44] D. O. Charlson, Ph.D. Thesis, Michigan State University(1995), hep-ph/9508278.

[45] A. Pukhov et al., CompHEP - a package for evaluation of Feynman diagrams and integration over multi-particle phase space, hep-ph/9908288.

[46] M.L. Mangano, M. Moretti, F. Piccinini, R. Pittau, A. Polosa, *ALPGEN, a generator for hard multiparton processes in hadronic collisions*, JHEP 0307:001,2003, hep-ph/0206293.

[47] I. Bertram *et al.*, *"A recipe for the Construction of Confidence Limits"*, Fermilab-TM-2104.

[48] J. Elmsheuser,M. Hohlfeld, *“Search for the Higgs boson in* $H \to WW^{(*)} \to l^+\nu l^-\bar{\nu}$ *(*$l = e,\mu$*) decays at DØ in Run II”* , DØ Note 4387.

[49] S. Anderson *et. al*,*“Measurement of the* $t\bar{t}$ *cross section at* $\sqrt{s} = 1.96\,\mathrm{TeV}$*”*, DØ Note 4116.

[50] M. Hohlfeld, private communication.

[51] The ATLAS Collaboration,*“ATLAS Detector and Physics Performance, Technical Design Report”*, CERN/LHCC/99-14 and CERN/LHCC/99-15, 1999.

[52] The ATLAS Muon Collaboration, *“ATLAS Muon Spectrometer Technical Design Report”*, CERN/LHCC/97-22, 1997.

[53] N. Hessey, A. Staude, T. Trefzger, *“Cosmic Ray test stand at the LMU Munich”*, ATLAS-MUON-98-266, 1998.

[54] A. Kraus,*“Genaue Bestimmung der Ereigniszeit und Entwicklung eines Alignierungssystems für einen großen Höhenstrahlteststand”*, Diploma thesis, LMU Munich, 2001.

[55] T. Nunnemann, private communication.

Acknowledgements

This work would not have been possible without the work of a lot of people at the DØ experiment, Tevatron collider, Fermilab and Munich computing division. I'd like to thank everybody for their tireless efforts for an excellent fundamental research.

In particular I'd like to thank the Munich particle physics group lead by Dorothee Schaile. She offered me the opportunity to this thesis and the possibility to work as a guest scientist at the DØ experiment on-site at Fermilab. My special thanks goes to Thomas Nunnemann who always had some good advise when things where getting complicated again.

Curriculum Vitae

14. June 1975	Born in Gießen, Germany Parents: Dr. Hans Elmsheuser, Monika Elmsheuser geb. Löw 2 Sisters: Annegret and Kathrin Elmsheuser
August 1981 - December 1983	Grundschule Rodheim v.d.H., Kreis Friedberg
December 1983 - June 1985	Grundschule Schallbach, Kreis Lörrach
August 1985 - June 1994	Hans-Thoma-Gymnasium Lörrach, Degree: Abitur
October 1994 - November 2000	Studies of Physics and Mathematics at Albert-Ludwigs-Universität Freiburg im Breisgau. Degree: Diplom
September 1997 - June 1998	SOCRATES-Scholarship, Studies of Physics and Mathematics at the University of Glasgow, U.K.
November 2000	Diploma thesis: Open beauty production in photon-photon collisions with the OPAL experiment.
January 2001 - present	Graduate studies and Wissenschaftlicher Angestellter at Ludwig-Maximillians-Universität München.
September 2001	Maria Laach Summer School of Particle Physics
January 2002 - September 2002	Guest scientist at Fermilab, Batavia, USA, DØ Level 2 Trigger expert.